STOCHASTIC DYNAMICS IN BUMP ATTRACTOR MODELS OF SPATIAL WORKING MEMORY

A Dissertation Presented to

the Faculty of the Department of Mathematics

University of Houston

In Partial Fulfillment

of the Requirements for the Degree

Doctor of Philosophy

By

Daniel Bernard Poll

May 2017

STOCHASTIC DYNAMICS IN BUMP ATTRACTOR MODELS OF SPATIAL WORKING MEMORY

Daniel Bernard Poll

APPROVED:

Dr. Krešimir Josić, Chairman
Department of Mathematics, University of Houston

Dr. Zachary Kilpatrick, Co-chairman
Department of Appl. Math, University of CO

Dr. Ilya Timofeyev
Department of Mathematics, University of Houston

Dr. William Ott
Department of Mathematics, University of Houston

Dr. Haluk Ogmen
School of ELEC, University of Denver

Dean, College of Natural Sciences and Mathematics

Acknowledgements

First and foremost, I would like to express my sincere gratitude to my advisor and mentor, Dr. Zachary Kilpatrick, for his encouragement, expertise, and patience. His guidance and understanding has truly impacted my writing and research of this thesis. I could not have imagined a better mentor during my graduate studies. I'm grateful to have been his student.

I also wish to extend my thanks to Dr. Krešimir Josić. His input into the research of this work and suggestions for future work was invaluable. In a similar vein, the rest of the lab: Simon, Adrian, James, and others have been vital with their own set of questions and suggestions throughout the last few years. Thanks for all the time and fun we've had working together.

My sincere thanks to the rest of the committee: Dr. William Ott, Dr. Ilya Timofeyev, and Dr. Haluk Ogmen. Whether it was through a class, sharing in research, or a passing conversation down the hall, all of you have contributed to my research and for that I am appreciative. I would also like to thank the National Science Foundation for funding support (NSF-DMS-1311755 and NSF-DMS-1615737).

Last but not least, I extend my thanks and love to my family for their unending support. Their encouragement during my struggles and their joy in my achievements are something I will always cherish.

STOCHASTIC DYNAMICS IN BUMP ATTRACTOR MODELS OF SPATIAL WORKING MEMORY

An Abstract of a Dissertation

Presented to

the Faculty of the Department of Mathematics

University of Houston

In Partial Fulfillment

of the Requirements for the Degree

Doctor of Philosophy

By

Daniel Bernard Poll

May 2017

Abstract

Mammalian spatial navigation systems utilize several different sensory information channels. This information is converted into a neural code that represents the animal's current position in space by engaging place cell, grid cell, and head direction cell networks. We begin by analyzing a classical model of short term memory, wherein stationary pulse solutions (bumps) correspond to a mammal's representation of position in two dimensions. Neural fields are integrodifferential equations whose integral kernel describes the strength and polarity of synaptic interactions between neurons at different locations in the network. Through asymptotic analysis, we can study the effects of weak external inputs into the network. We find bumps tend to drift towards local attractors endowed by external inputs. Furthermore, when weak spatiotemporal noise is introduced, bumps tend to diffuse. This can disrupt the position code over short time windows, causing a degradation in location recollection. To address position errors induced by noise, we introduce a novel addition to the model that incorporates the effects of sensory landmarks. Through the inclusion of an external control signal, representing the effects of sensory landmarks in a given environment, errors can be reduced significantly. Our analysis concludes with extensions to multilayer (coupled) networks. We can again derive a low-dimensional approximation of the network dynamics that describes how heterogeneity, noise, and velocity input impact bump position. In particular, we find excitatory synaptic coupling between layers promotes correct velocitiy integration by reducing the effects of noise, a phenomena known as 'reliability through redundancy'.

Contents

Chapter 1

Introduction

1.1 Biological Motivation

Spatial working memory tasks test the brain's ability to encode information for short periods of time [65, 114]. A subject's performance during such tasks can be paired with brain recordings to help determine how neural activity patterns represent memory during a trial [70]. When a monkey is trained to recall the specific position of a cue, the network location of persistent activity encodes the corresponding cue location. Any displacement of the persistent activity from its initial location is reflected by errors the monkey makes in recalling the cue's position [160]. In a related way, persistent activity in the entorhinal cortex [73] and hippocampus [32] can store an animal's physical location in its environment, constituting an internal "global positioning system" [1]. In general, working memory involves the retention of information for time periods lasting a few seconds [11],

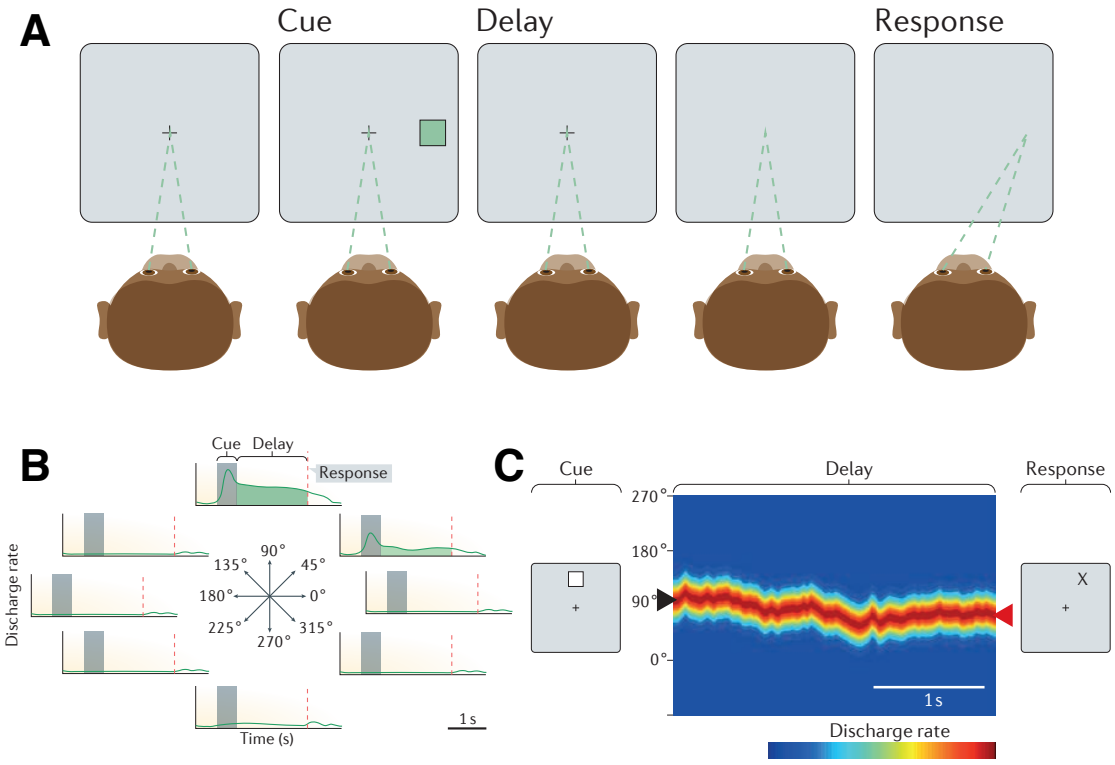

Figure 1.1: Example of a spatial working memory task. (**A**) A monkey is presented a visual cue at a fixed angle. The cue is then removed while the monkey attempts to remember its location. After a few seconds, the monkey is allowed to move its eyes to the direction of the cue. (**B**) Diagram of the activity of a single prefontal neuron during the task. (**C**) Activity of the network in time, wherein localized neural activity tends to diffuse during the delay period. Adapted from [41]

operating on the order of milliseconds. More specifically, spatial working memory involves the short term storage of a spatial variable, such as idiothetic location [33] or a location on a visual display [54]. While most studies of spatial working memory tend to focus on recalling an analog variable in one-dimension [150], networks performing tasks such as spatial navigation have been shown to represent space in two [107] and even three dimensions [165].

In addition to the short term storage of location, several networks of the brain

can integrate velocity signals to update a remembered position [109]. Angular velocity of the head is used by the vestibular system to update memory of heading direction [141]. Furthermore, intracellular recordings from goldfish demonstrate that eye position can be tracked by neural circuits that integrate saccade velocity to update memory of eye orientation [3]. Velocity integration has also been identified in place cell and grid cell networks, which track an animal's idiothetic location [68, 73, 157]. While these networks each possess distinct circuit mechanisms for integrating and storing information, the general dynamics of their stored position variables tends to be similar [107].

However, there are a number of potential sources of error to this velocity integration mechanism. The nervous system itself is prone to a wide variety of noise sources due to channel fluctuations, synaptic failures, or even stochastic network-wide events [57]. This could lead to faulty communication of velocity or head direction signals, or it could corrupt the storage of the position signal [140]. Furthermore, the network that integrates the velocity signal may be comprised of architecture that is heterogeneous, providing an imperfect summation of velocity inputs [26]. Any inaccuracy in the represented position or velocity will be compounded over time, as the neural code continues to trace the animal's true path [93, 146].

Fortunately, path integration is not the sole navigational technique of the mammalian brain; landmarks detected by the sensory system help anchor and correct the integrated velocity signal [39, 56, 138]. Several experiments have demonstrated that mammals' representation of space is sharpened in the presence of

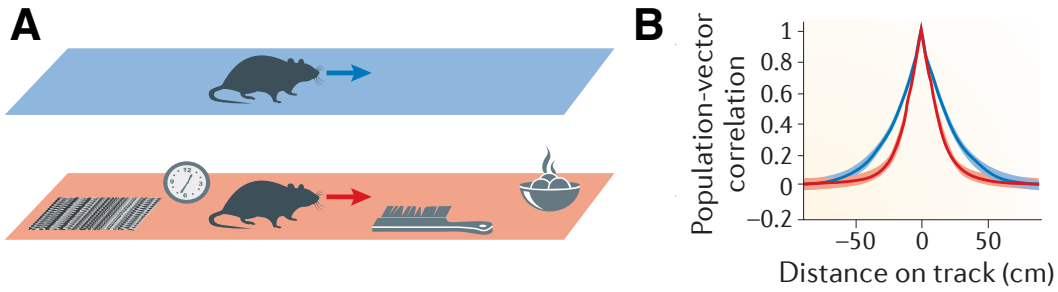

Figure 1.2: (**A**) Schematic of a mammal traversing a one-dimensional track without sensory landmarks (blue) and in the presence of sensory landmarks (red). (**B**) Measurements in population-vector correlations show a trend of narrower place fields in the presence of sensory landmarks (red) compared to the absence of landmarks (blue). Adapted from [68].

sensory cues (Fig. 1.2**B**) [2, 12, 145, 169]. Experiments typically compare place fields of individuals cells - spatial locations where the cell becomes active - in the presence and absence of sensory landmarks (e.g., steel brush or ticking clock; Fig. 1.2**A**). For instance, Battaglia et al. (2006), recorded from hippocampal place cells in rats moving on an annular track [12]. When there were no sensory cues along the track, the measured place field of an individual cell could differ substantially, depending on whether the rat was moving clockwise or counterclockwise around the annulus. This suggests there was some drift in animals' neural representation of their position. However, when several position cues were placed along the track, the clockwise and counterclockwise place fields of individual cells were strongly correlated. This suggests the sensory cues tightened the navigation system's fine representation of the animal's spatial position [130]. Similar effects have been observed in brown bats, whose echolocation signals provide a brief burst of

rich sensory information, sharpening the animal's place fields [145]. Thus, sensory cues appear to provide a correction mechanism for the many sources of error that disrupt position representation and broaden place fields.

Another important feature of spatial working memory, often overlooked in models, is its distributed nature [79]. Most models focus on the dynamics of persistent activity representing position memory in a single-layer network [40, 102, 168]. However, extensive evidence demonstrates working memory for visuospatial and idiothetic position is represented in several distinct modules in the brain that communicate via long-range connectivity [50, 129]. There are many possible advantages conferred by such a modular organization of networks underlying spatial memory. One well tested theory notes different network layers can represent position memory on different spatial scales, leading to higher accuracy within small-scale layers and wider range in large-scale layers [29]. Furthermore, the information contained in spatial working memory is often needed to plan motor commands, so it is helpful to distribute this signal across sensory, memory, and motor-control systems [125]. Another advantage of generating multiple representations of position memory is that it can stabilize the memory through redundancy [132]. For instance, coupling between multiple layers of a working memory network can reduce the effects of noise perturbations, as we have shown in previous work [86].

In addition to being distributed, the networks that generate persistent activity underlying spatial working memory also appear to be heterogeneous. For instance, prefrontal cortical networks possess a high degree of variation in their

synaptic plasticity properties as well as their cortical wiring [120, 153]. Furthermore, there is heterogeneity in the way place cells from different hippocampal regions respond to changes in environmental cues [7, 103]. Along with such between-region variability, there is local variability in the sequenced reactivations of place cells that mimic the activity patterns that typically occur during active exploration [115]. In particular, these reactivations are saltatory, rather than smoothly continuous, so activity focuses at a discrete location in the network before rapidly transitioning to a discontiguous location. Such activity suggests that the underlying network supports a series of discrete attractors, rather than a continuous attractor [26].

1.2 Neural Field Model

Network models of this activity typically involve local excitation and broader inhibition, producing localized activity packets referred to as *bump attractors* [40, 99]. These models have recently been validated using recordings from oculomotor delayed-response tasks in monkeys [160] and from grid cell networks of freely moving rats [166]. This suggests that studying network mechanisms for generating reliable neural activity dynamics can provide insight into how the brain robustly performs spatial working memory tasks. We focus on a particular continuum model of neural activity, known as a *neural field equation*.

The solutions and applications of neural field equations have been studied extensively [19, 20]. In particular, stationary bumps can be regarded as an idealized

model of location encoding [4, 102]. Many studies have examined how modifications into the model impact solutions. These modifications include experimentally verified phenomena such as synaptic heterogeneity [60], short term plasticity [82], and adaptation [46]. Heterogeneity, for example, can cause discrete attractors to form in the network, pinning the bump in place [90]. Plasticity itself is a known mechanism generating heterogeneity by modifying synaptic coupling strengths [119, 122]. While bumps are a particular class of solutions that arise from a neural field equation, many other solutions have been studied such as traveling waves, fronts, and anti-pulse solutions [43, 116].

However, previous work has largely focused on deterministic neural field equations, ignoring the impact of noise on spatiotemporal dynamics. This is a useful assumption in analysis, but also disregards features that may be present in the network. While there are a few exceptions [20, 98], to our knowledge no study has analyzed in detail the impact of noise on neural field models of spatial navigation. We improve these deterministic models by including dynamic input fluctuations (noise) and studying their impact on bump attractor dynamics. For example, one key difference from deterministic models is the absence of purely stationary solutions. Any pinning of the bump, as a result of an input or heterogeneity, is temporary due to synaptic fluctuations. Another important difference is the impact fluctuations have on velocity integration. The inclusion of noise introduces an instability in bump position. We address this in Chapters 3 and 4.

As a starting point, we introduce the neural field model [6, 112, 142, 156]

$$\frac{\partial u(x,t)}{\partial t} = -u(x,t) + \int_{\Omega} w(x,y) f(u(y,t))\, dy, \tag{1.1}$$

where $u(x,t)$ denotes the total synaptic input to the neural field at the position $x \in \Omega$. The integral term describes the synaptic connectivity of the network, so that $w(x,y)$ describes the strength (amplitude) and polarity (sign) of connectivity from neurons at location y to neurons at location x. In Chapter 2, we will use two dimensional modified Bessel functions of the second kind to generate a Mexican hat kernel, such that translation symmetry is preserved, i.e. $w(x,y) \equiv w(x-y)$. This will allow us to write a finite explicit expression for stationary bump solutions through Hankel transforms. In Chapter 3, we will simplify our computations by considering one-dimensional periodic kernels $w(x,y)$, such as cosine or a sum of cosines. However, we will allow for a weak heterogeneity, such that $w(x,y) = (1+\epsilon h(y))w(x-y)$, where $h(.)$ is the function describing the network heterogeneity. Clearly, if $\epsilon \equiv 0$, we recover the homogeneous case. Chapter 4 will utilize similar functions as Chapter 3, but with the assumption that synaptic connectivity in individual layers is heterogeneous, while the connectivity between layers remains homogeneous.

The function f denotes the firing rate of the model, which is a representation of the fraction of total active neurons, $0 \leq f \leq 1$. Experimental data suggests f should roughly be a sigmoidal function [158]

$$f(u) = \frac{1}{1+e^{-\gamma(u-\kappa)}} \tag{1.2}$$

where u is the synaptic input, γ is the gain and κ is the threshold. The effective equations we derive for the stochastic motion of bumps will hold for general firing

rate functions f, but we consider the high gain limit $\gamma \to \infty$ of (1.2) to compute the resulting formulas explicitly. In this case [4, 6]

$$f(u) := H(u-\kappa) = \begin{cases} 1: & u \geq \kappa, \\ 0: & u < \kappa, \end{cases} \tag{1.3}$$

so the firing rate function is a Heaviside function.

The neural field equation (1.1) in the absence of noise has been studied extensively, demonstrating a wide variety of neural patterns [6, 48, 101, 112]. However, our main concern is the impact of noise on stationary bump solutions of (3.1). We focus on a model that incorporates additive noise into a neural field, an extension of recent studies that have explored how noise shapes spatiotemporal dynamics of neural fields in one-dimensional domains [16, 19, 80, 99]. The model takes the form of a Langevin equation on the domain Ω forced by a spatiotemporal noise process

$$du(x,t) = \Big(-u(x,t) + \int_\Omega w(x,y) f(u(y,t))\, dy \Big) dt + \varepsilon dW(x,t). \tag{1.4}$$

The term $dW(x,t)$ is the increment of a spatially varying Wiener process with spatial correlations defined

$$\langle dW(x,t) \rangle = 0, \quad \langle dW(x,t) dW(y,s) \rangle = C(x-y)\delta(t-s)dtds, \tag{1.5}$$

so that ε describes the intensity of the noise, which we assume to be weak ($\varepsilon \ll 1$). The function $C(x-y)$ describes the spatial correlation in each noise increment between two points $x, y \in \Omega$. The spatial correlation function $C(x-y)$ can be related directly to the spatial filter $\mathcal{F}(x-y)$. First, we note that $dW(x,t)$ can be defined

by convolving a spatially white noise process $d\mathcal{Y}(x,t)$, satisfying $\langle d\mathcal{Y}(x,t)\rangle = 0$ and $\langle d\mathcal{Y}(x,t)d\mathcal{Y}(y,s)\rangle = \delta(x-y)\delta(t-s)dtds$, with the filter $\mathcal{F}(x-y)$, so

$$dW(x,t) = \int_\Omega \mathcal{F}(x-y)d\mathcal{Y}(y,t)dy.$$

Thus, we can determine how the variance of $dW(x,t)$ depends on the filter $\mathcal{F}(x-y)$ by computing

$$\begin{aligned}
\langle dW(x,t)dW(y,t)\rangle &= \left\langle \int_\Omega \mathcal{F}(x-x')d\mathcal{Y}(x',t)dx' \int_\Omega \mathcal{F}(y-y')d\mathcal{Y}(y',t)dy' \right\rangle \\
&= \int_\Omega \int_\Omega \mathcal{F}(x-x')\mathcal{F}(y-y')\langle d\mathcal{Y}(x',t)d\mathcal{Y}(y',t)\rangle dy'dx' \\
&= \int_\Omega \int_\Omega \mathcal{F}(x-x')\mathcal{F}(y-y')\delta(x'-y')dy'dx'\delta(t-s)dtds \\
\langle dW(x,t)dW(y,t)\rangle &= \int_\Omega \mathcal{F}(x-x')\mathcal{F}(y-x')dx'\delta(t-s)dtds \\
&= C(x-y)\delta(t-s)dtds, \qquad (1.6)
\end{aligned}$$

so

$$C(x-y) = \int_\Omega \mathcal{F}(x-x')\mathcal{F}(y-x')dx'. \qquad (1.7)$$

The last equality in (1.6) holds due to our definition of $dW(x,t)$. Note that (1.7) implies that $C(x-y)$ should be an even symmetric function, since the arguments of both functions $\mathcal{F}(x)$ can be exchanged. In other words, the points x and y in $C(x-y)$ can also be exchanged.

We also consider an external stimulus $I(x,t)$ acting on our stochastic system (1.4), and our modified model takes the form

$$du(x,t) = \left(-u(x,t) + \int_{\mathbb{R}^2} w(x,y)f(u(x,t))\,dy + I(x,t)\right)dt + \varepsilon dW(x,t). \qquad (1.8)$$

In Chapter 2, we will consider stationary external inputs and analyze the resulting dynamics. In Chapters 3 and 4, we will use a spatially constant weak input $I(x,t) \equiv \varepsilon I(t)$. Based on a simplified version of the model by [127], neural activity bumps are propelled around the network by external velocity inputs that introduce spatial asymmetry into the balance of excitation and inhibition. A similar mechanism was utilized by [30] in a two-dimensional model of grid cell activity. Thus, this framework is a well accepted model of position encoding cells in hippocampus, entorhinal cortex, and the vestibular system [168].

1.3 Content of Dissertation

The content of the dissertation is as follows. In Chapter 2, we examine the impact of noise on the memory of a two-dimensional continuous variable in a bump attractor network. In particular, we explore the stochastic motion of bumps in planar neural fields, reaching beyond current work that tends to explore one-dimensional domains [19, 80]. Our principal finding is that weak noise causes stationary bumps to execute two-dimensional Brownian motion, which can be quantified with an effective diffusion coefficient. Our derivations require the enforcement of a solvability condition for the linearization of a nonlinear Langevin equation on the plane. Since bump position represents a memory of an initial condition, we are interested in what features of the model shape the long term diffusion of the bump. Thus, we also analyze the impact of external inputs on stochastic bump motion, finding they tend to pin the bumps to their peaks. We begin

Section 2.1 by reviewing previous analyses of existence and stability of radially symmetric bumps [112], providing intuition for the impact of noise perturbations on bump position. Subsequently, we derive an effective equation for the dynamics of radially symmetric bumps subject to weak noise, deriving an effective diffusion coefficient for the variance of the bump's position. In Section 2.2, we extend these results by incorporating the effects of an external input on the stochastic dynamics of bumps. Inputs stabilize bumps to translating perturbations, so the position of noise-driven bumps evolves approximately as an Ornstein-Uhlenbeck process in two dimensions.

Proceeding to Chapter 3, we note recent experiments have examined rodent navigation on an annular track [12]. Thus, we introduce a neural field model of spatial navigation in a one-dimensional periodic domain, which combines path integration and sensory cue feedback. Errors in the path integration signal will arise, in our model, due to internal disruptions of an accurately delivered velocity input. Based on a double ring network model of the head-direction system [164], we can reformulate a constant external input, acting as the velocity input, into a single bump attractor model describing the impact of the input on the synaptic connectivity (Appendix A). Sensory cues are assumed to provide a reliable estimate of the animal's true position. This position is then compared with the place cell network's estimate of position. Any discrepancy in the position estimate is then translated into a corrective velocity input, which is added to the baseline velocity input (Fig. 3.1**A**). Even when the cues occur discretely in space, this mechanism works well for reducing the long term error in the position estimate.

Through asymptotic analysis, we can derive a low-dimensional approximation for the dynamics of bump position in the neural field model (Section 3.2). This reduction reveals the relative influence of velocity inputs, sensory feedback, and heterogeneity on the animal's perceived position of its current location.

Ultimately, this allows us to calculate the impact of various control strategies on the error between the animal's perceived position and true position (Section 3.3). Our main finding is that there is an optimal control strength at which the long term error of the network is minimized. Our findings are similar in the case that errors arose due to dynamic noise fluctuations (Subsection 3.3.2), rather than synaptic heterogeneities (Subsection 3.3.1). In this case, the low-dimensional approximation of the neural field is a stochastic differential equation whose variance we can evaluate explicitly.

Finally, Chapter 4 concludes by examing how the architecture of multilayer networks impacts the quality of the encoded spatial memory. Previous work has examined networks whose interlaminar connectivity was weak and/or symmetric, ignoring the effects of spatial heterogeneity in constituent layers [86, 88]. In this work, we will depart from the limit of weak coupling, and derive effective equations for the dynamics of bumps whose positions encode a remembered location. Through the use of linearization and perturbation theory, we can thus determine how both the spatial heterogeneity of individual layers and the coupling between layers impact spatial memory storage. Previous work has also shown that spatial heterogeneity can help to stabilize memories of a stationary

position [91], but such heterogeneities also disrupt the integration of velocity inputs [118]. Thus, it is important to understand the advantages and drawbacks of heterogeneities, and quantify how they trade off with one another.

We focus on a multilayer neural field model of spatial working memory, with arbitrary coupling between layers and spatial heterogeneity within layers. Furthermore, as we are interested in both the retention of memory and the integration of input, we incorporate a velocity-based modulation to the recurrent connectivity which is non-zero when the network receives a velocity signal [168]. The stationary bump solutions of this network are analyzed in Section 4.2. Since the effects of velocity input and heterogeneity are presumed to be weak, the stationary bump solutions only depend upon the connectivity between layers. Analyzing the stability of bumps, we can determine the marginally stable modes of these bump solutions which will be susceptible to noise perturbations. Subsequently, we derive a one-dimensional stochastic equation that describes the response of the bump solutions to noise, velocity input, and spatial heterogeneity. With this approximation in hand, we can determine the effective diffusion and velocity of bumps using asymptotic methods, which compare well with numerical simulations of the full model (Section 4.3). Lastly, we analyze more nuanced architectures in Section 4.4, whose bump solutions possess multiple marginally stable modes. As a result, we find we must derive multi-dimensional stochastic equations to describe their dynamics in response to noise. Our work examines in detail the effects of modular network architecture on the coding of spatial working memory.

Chapter 2

Dynamics of Bumps in a Model of Spatial Working Memory

2.1 Wandering bumps in $\mathbb{R}^2$

We begin by studying bumps in the unbounded domain $\Omega = \mathbb{R}^2$, first in the absence of noise (1.1) and then in the presence of additive noise (1.4). Recent studies have shown traveling waves and bumps in stochastic neural fields wander diffusively about their mean position, but these analyses have focused on one-dimensional domains [19, 90]. Our analysis will allow us to approximate the diffusion coefficient of a bump driven by noise in a two-dimensional domain. Since we are exploring the model (1.4) in $\mathbb{R}^2$, we can utilize Hankel transforms to compute integral terms [61].

2.1.1 Existence and stability of bumps

To begin, we review prior results constructing rotationally symmetric stationary bump solutions in the noise-free system [6, 112, 142],

$$\frac{\partial u(x,t)}{\partial t} = -u(x,t) + \int_\Omega w(x,y) f(u(y,t)) dy. \tag{1.1}$$

Specifically, we employ the assumption that the weight function (2.2) is rotationally symmetric to look for stationary solutions of the form $u(\mathbf{x},t) := U(\mathbf{x}) = U(||\mathbf{x}||)$. Recall $u(\mathbf{x},t)$ is the neural activity at location $\mathbf{x} = (x_1, x_2) \in \mathbb{R}^2$ at time t. In this case, the neural field equation (1.1) simplifies to

$$U(||\mathbf{x}||) = \int_{\mathbb{R}^2} w(\mathbf{x}-\mathbf{y}) f(U(\mathbf{y})) d\mathbf{y}. \tag{2.1}$$

In our analysis, we utilize a sum of $N+1$ modified Bessel functions as our weight function

$$w(\mathbf{x}-\mathbf{y}) = \sum_{j=0}^{N} c_j K_0(\alpha_j ||\mathbf{x}-\mathbf{y}||), \tag{2.2}$$

where K_v is a modified Bessel function of the second kind of order v. The constants c_j and α_j scale the amplitude and spatial decay of the jth term in the Bessel function sum. One advantage of the weight function (2.2) is that integrals arising in (1.1) can be computed analytically with the aid of Hankel transforms [61, 101, 112]. Note that $||.||$ denotes the standard Euclidean 2-norm

$$||\mathbf{x}|| = \sqrt{x_1^2 + x_2^2}$$

so that w of the form (2.2) will be radially symmetric. By changing variables to polar coordinates $\mathbf{x} = (x_1, x_2) \mapsto \mathbf{r} = (r, \theta)$, we can convert (2.1) to a double

integral of the form

$$U(r) = \int_0^{2\pi} \int_0^{\infty} w(|\mathbf{r} - \mathbf{r}'|) f(U(\mathbf{r}')) r' dr' d\theta'. \tag{2.3}$$

Note that if we assume a Heaviside firing rate function (1.3), then (2.3) becomes

$$U(r) = \int_0^{2\pi} \int_0^{a} w(|\mathbf{r} - \mathbf{r}'|) r' dr' d\theta', \tag{2.4}$$

where $U(\mathbf{r}) > \kappa$ when $r < a$ and $U(\mathbf{r}) < \kappa$ when $r > a$, so that $r \equiv a$ defines the boundary of the bump. An advantage of using a Heaviside firing rate function (1.3) is that the stability of the bump can be probed by analyzing the dynamics of the boundary. When we analyze the stochastic motion of the bump, we will also derive effective equations by focusing on perturbations of the bump boundary by spatiotemporal noise. We can evaluate the integral in (2.4) using Hankel transform and Bessel function identities, as in [61, 112]

$$U(r) = \int_0^{\infty} \widehat{w}(\rho) J_0(r\rho) J_1(a\rho) d\rho, \tag{2.5}$$

where $J_\nu(z)$ is a Bessel function of the first kind of order ν and the Hankel transform is defined as

$$\widehat{w}(\rho) = \int_{\mathbb{R}^2} \mathrm{e}^{i\mathbf{h}\cdot\mathbf{r}} w(\mathbf{r}) d\mathbf{r},$$

where $\rho = ||\mathbf{h}||$.

To illustrate our analysis, we consider the weight (2.2) given by a sum of modified Bessel functions [112]. Using the fact that the corresponding Hankel transform of $K_0(sr)$ is $\mathcal{H}(\rho, s) = (\rho^2 + s^2)^{-1}$, we have

$$\widehat{w}(\rho) = \sum_{j=1}^{N} c_j \mathcal{H}(\rho, \alpha_j). \tag{2.6}$$

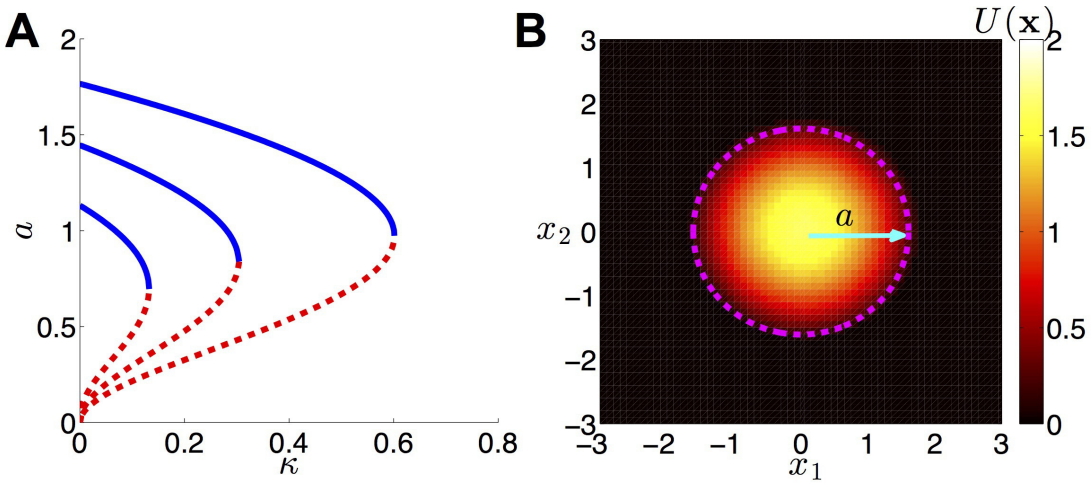

Figure 2.1: Stationary bump solutions $u(\mathbf{x},t) = U(r)$ to the deterministic model (1.1) with weight function (2.2) and Heaviside firing rate (1.3). (**A**) A wider stable (solid) and narrower unstable (dashed) branch of solutions to $U(a) = \kappa$ emerges from a saddle-node bifurcation at a critical value of κ above which no solutions exist. Weight function parameters are (left to right) $[c_1, c_2, c_3, c_4] = [10/9, -10/9, -1/3, 1/3]; [4/3, -4/3, -2/5, 1/3]; [5/3, -5/3, -1/2, 1/2]$. (**B**) An example of a stationary bump $U(\mathbf{x})$ for the parameters $\kappa = 0.2$ and $[c_1, c_2, c_3, c_4] = [5/3, -5/3, -1/2, 1/2]$. We have fixed $[\alpha_1, \alpha_2, \alpha_3, \alpha_4] = [1, 2, 1/4, 1/2]$, as in (2.9).

The bump solution (2.5) can then be evaluated by using the formula (2.6) along with the identity

$$\int_0^\infty \frac{J_0(\rho r)J_1(\rho a)}{\rho^2 + s^2} d\rho \equiv \mathcal{I}(a,r,s) = \begin{cases} \frac{1}{s} I_1(sa)K_0(sr) & : r > a, \\ \frac{1}{s^2 a} - \frac{1}{s} I_0(sr)K_1(sa) & : r < a, \end{cases} \tag{2.7}$$

where I_ν is the modified Bessel function of the first kind of order ν. We can thus generate an explicit solution for the stationary bump $U(r)$, given

$$U(r) = 2\pi a \sum_{k=0}^{N} c_k \mathcal{I}(a,r,\alpha_k).$$

Applying the threshold condition $U(a) = \kappa$, we can generate an implicit equation

relating the bump radius a with the threshold κ and weight parameters

$$U(a) = 2\pi a \sum_{k=0}^{N} \frac{c_k}{\alpha_k} I_1(\alpha_k a) K_0(\alpha_k a) = \kappa. \tag{2.8}$$

In general, explicit solutions for a cannot be computed and (2.8) must be solved numerically using root finding algorithms. Note also that satisfaction of the threshold condition (2.8) is not sufficient for proving the existence of a bump. For instance, the possibility of *ring* solutions must be eliminated by ensuring there are no other threshold crossing points [48, 112]. Furthermore, we must develop a linear stability analysis to identify those bumps that will persist in the presence of perturbations. This will especially be important in our analysis of the stochastic system (1.4), since it will rely on the assumption that the perturbed solution retains a profile similar to the unperturbed system.

We demonstrate the results of this existence analysis by using a Mexican hat type weight distribution such as [23, 112]

$$w(r) = c_1 K_0(r) + c_2 K_0(2r) + c_3 K_0(r/4) + c_4 K_0(r/2), \tag{2.9}$$

where we have fixed the spatial scales $[\alpha_1, \alpha_2, \alpha_3, \alpha_4] = [1, 2, 1/4, 1/2]$ and will take $c_1, c_4 > 0$ and $c_2, c_3 < 0$ to generate a lateral inhibitory kernel. Typically, weight functions like (2.9) lead to a maximum of two bump solutions, as shown in Fig. 2.1.

As mentioned, we must be aware of the possibility of azimuthal instabilities of the stationary bump when developing our linear stability theory [21, 112]. Thus, while it may be convenient to analogize the shifting and expanding/contracting perturbations of 1D bumps [4] with D_1 and circularly symmetric perturbations of

2D bumps [142], one should be sure not to stop here. A full analysis of azimuthal perturbations to the bump (2.3), D_n-symmetric perturbations ($n \in \mathbb{Z}$, $n > 1$), is necessary since bumps can destabilize through such symmetry-breaking instabilities [23, 112]. It is worth noting that this fact was originally identified by Amari in 1978 [5], and other systematic analyses were carried out in the last decade [48, 112].

To determine the stability of stationary solution, we will consider small, smooth perturbations of the stationary bump solution (2.3) of the form $u(\mathbf{x}, t) := U(\mathbf{x}) + \varepsilon\Psi(\mathbf{x}, t)$ where $\varepsilon \ll 1$. We substitute this into equation (1.1) and Taylor expand to linear order to generate the equation

$$\frac{\partial\Psi(\mathbf{x}, t)}{\partial t} = -\Psi(\mathbf{x}, \mathbf{t}) + \int_{\mathbb{R}^2} w(\mathbf{x} - \mathbf{y}) f'(U(\mathbf{y}))\Psi(\mathbf{y}, t) d\mathbf{y}. \tag{2.10}$$

Applying seperation of variables $\Psi(\mathbf{x}, t) = \Psi(\mathbf{x})b(t)$ and rearranging terms results in the solutions $b(t) = e^{\lambda t}$ and

$$(\lambda + 1)\Psi(\mathbf{x}) = \int_{\mathbb{R}^2} w(\mathbf{x} - \mathbf{y}) f'(U(\mathbf{y}))\Psi(\mathbf{y}) d\mathbf{y}. \tag{2.11}$$

We can immediately identify neutrally stable perturbations, those corresponding to $\lambda = 0$, by letting $\Psi(\mathbf{x}) = U_{x_j}(\mathbf{x})$ with $j \in \{1, 2\}$. We apply integration by parts and the definition of a stationary solution U given in (2.1) into (2.11) to yield

$$\begin{aligned}(\lambda + 1)U_{x_j}(\mathbf{x}) &= \int_{\mathbb{R}^2} w(\mathbf{x} - \mathbf{y}) f'(U(\mathbf{y}))U_{y_j}(\mathbf{y})\, d\mathbf{y} = \int_{\mathbb{R}^2} w(\mathbf{x} - \mathbf{y}) \frac{\partial}{\partial y_j}\big(f(U(\mathbf{y}))\big)\, d\mathbf{y} \\ &= \int_{\mathbb{R}^2} \frac{\partial}{\partial y_j}\big(w(\mathbf{x} - \mathbf{y})\big) f(U(\mathbf{y}))\, d\mathbf{y} = \int_{\mathbb{R}^2} \frac{\partial}{\partial x_j}\big(w(\mathbf{x} - \mathbf{y})\big) f(U(\mathbf{y}))\, d\mathbf{y} \\ &= \frac{\partial}{\partial x_j}\left(\int_{\mathbb{R}^2} w(\mathbf{x} - \mathbf{y}) f(U(\mathbf{y}))\, d\mathbf{y} \right) = U_{x_j}(\mathbf{x}). \end{aligned} \tag{2.12}$$

Thus, by the linearity of the integral

$$\Psi_Z(\mathbf{x}) = h_1 U_{x_1}(\mathbf{x}) + h_2 U_{x_2}(\mathbf{x}) \tag{2.13}$$

generates the class of solutions corresponding to the eigenvalue $\lambda_1 = 0$. Note, we will not have such a class of perturbations in the case of stationary external inputs, as the translation symmetry of (1.1) will then be broken.

Prior to analyzing other azimuthal perturbations to the bump (2.3), we briefly discuss how perturbations of the form (2.13) impact the long term bump position. In fact, it is precisely this neutral stability of the bump that leads to purely diffusive motion of the bump in the stochastic model (1.4). Specifically, we focus on the case of a Heaviside firing rate function (1.3), so we can track the position $\boldsymbol{\Delta} = (\Delta_1, \Delta_2) \in \mathbb{R}^2$, i.e. the spatial mean, of the bump by utilizing the level set condition $u(\mathbf{x}, t) = \kappa$, which can be written

$$\begin{aligned}\kappa =& u(a + \varepsilon b(\theta, t), \theta, t) = U(a + \varepsilon b(\theta, t)) + \varepsilon \Psi(a + \varepsilon b(\theta, t), \theta, t) \\ \kappa =& U(a) + \varepsilon U'(a) b(\theta, t) + \varepsilon \Psi(a, \theta, t) + \mathcal{O}(\varepsilon^2),\end{aligned} \tag{2.14}$$

where $b(\theta, t)$ describes the perturbation of the bump boundary $R(\theta, t) = a + \varepsilon b(\theta, t)$ at angular coordinate θ and $\varepsilon \ll 1$. Note we can employ the stationary level set condition $U(a) = \kappa$ to cancel leading order terms in (2.14) to yield [61]

$$b(\theta, t) = \frac{\Psi(a, \theta, t)}{|U'(a)|} + \mathcal{O}(\varepsilon). \tag{2.15}$$

If we specifically denote $\Psi(a, \theta, t)$ to be a neutrally stable perturbation (2.13), then $\Psi(a, \theta, t) = \Psi_Z(a, \theta)$ and $b(\theta, t) = b_1(\theta)$, so that to first order

$$b_1(\theta) = \frac{\Psi_Z(a, \theta)}{|U'(a)|} = \frac{h_1 U'(a) \cos\theta + h_2 U'(a) \sin\theta}{|U'(a)|} = -h_1 \cos\theta - h_2 \sin\theta, \tag{2.16}$$

where we have computed

$$\frac{\partial}{\partial x_1} U(||\mathbf{x}||)\Big|_{r=a} = U'(a)\cos\theta, \qquad \frac{\partial}{\partial x_2} U(||\mathbf{x}||)\Big|_{r=a} = U'(a)\sin\theta. \tag{2.17}$$

Thus, the new bump boundary $R_0(\theta) \approx a + \varepsilon b_1(\theta)$ can be approximated in polar coordinates as

$$R_0(\theta) = a - \varepsilon h_1 \cos\theta - \varepsilon h_2 \sin\theta. \tag{2.18}$$

This approximates the long-term perturbation to the bump boundary $\lim_{t\to\infty} R(\theta, t) \approx R_0(\theta)$ by simply using the leading order term in the expansion $b(\theta, t) = b_1(\theta) + \sum_{j=0, j\neq 1}^{\infty} b_j(\theta) e^{\lambda_j t}$, as $\lim_{t\to\infty} b(\theta, t) = b_1(\theta)$ since all other $\mathrm{Re}\lambda_j < 0$. This follows from the well known result that circularly symmetric bump solutions to (1.1) are neutrally stable to D_1 symmetric perturbations of the bump boundary [61, 112]. Now, define the centroid (center of mass) $\boldsymbol{\Delta} = (\Delta_1, \Delta_2)$ as the first moments of mass along the $x-$ and $y-$directions scaled by the total mass for the lamina Ω_R of uniform density enclosed by the curve (2.18). In Cartesian coordinates, these quantities are given by the double integral formulae $\Delta_1 = \int\int_{\Omega_R} x dx dy / \int\int_{\Omega_R} dx dy$ and $\Delta_2 = \int\int_{\Omega_R} y dx dy / \int\int_{\Omega_R} dx dy$. By utilizing polar coordinates $(x, y) = (r\cos\theta, r\sin\theta)$, and plugging in the formula for the closed curve $R(\theta)$ (2.18), we can compute:

$$\begin{aligned}\Delta_1 &= \frac{\int_0^{2\pi}\int_0^{R(\theta)} r^2\cos\theta dr d\theta}{\int_0^{2\pi}\int_0^{R(\theta)} r dr d\theta} = \frac{\frac{1}{3}\int_0^{2\pi}(a - \varepsilon h_1\cos\theta - \varepsilon h_2\sin\theta)^3\cos\theta d\theta}{\frac{1}{2}\int_0^{2\pi}(a - \varepsilon h_1\cos\theta - \varepsilon h_2\sin\theta)^2 d\theta} \\ &= \frac{\frac{a^2}{3}\int_0^{2\pi}(a - 3\varepsilon h_1\cos\theta - 3\varepsilon h_2\sin\theta)\cos\theta d\theta}{\frac{a}{2}\int_0^{2\pi}(a - 2\varepsilon h_1\cos\theta - 2\varepsilon h_2\sin\theta) d\theta} + \mathcal{O}(\varepsilon^2) \approx -\varepsilon h_1\end{aligned}$$

and

$$\Delta_2 = \frac{\int_0^{2\pi}\int_0^{R(\theta)} r^2 \sin\theta dr d\theta}{\int_0^{2\pi}\int_0^{R(\theta)} r dr d\theta} = \frac{\frac{1}{3}\int_0^{2\pi}(a-\varepsilon h_1\cos\theta-\varepsilon h_2\sin\theta)^3\sin\theta d\theta}{\frac{1}{2}\int_0^{2\pi}(a-\varepsilon h_1\cos\theta-\varepsilon h_2\sin\theta)^2 d\theta}$$
$$= \frac{\frac{a^2}{3}\int_0^{2\pi}(a-3\varepsilon h_1\cos\theta-3\varepsilon h_2\sin\theta)\sin\theta d\theta}{\frac{a}{2}\int_0^{2\pi}(a-2\varepsilon h_1\cos\theta-2\varepsilon h_2\sin\theta)\, d\theta} + \mathcal{O}(\varepsilon^2) \approx -\varepsilon h_2.$$

Thus a perturbation in the bump profile of the form (2.13) will yield a proportional shift in the bump's center of mass $(\Delta_1, \Delta_2) = -\varepsilon(h_1, h_2)$. This foreshadows the impact of noise-induced perturbations to the bump's position, which we explore in Section 2.1.2. Effectively, we will show the primary contribution to the stochastic motion of bumps is the D_1-symmetric portion of the spatiotemporal noise, which is filtered by the bump as a spatial translation of its boundary and center of mass.

Lastly, we briefly review the analysis of azimuthal perturbations to the bump boundary. Note that in the case of a Heaviside firing rate function (1.3), then

$$f'(U(\mathbf{x})) = \delta(U(r)-\kappa) = \frac{\delta(r-a)}{|U'(a)|}, \tag{2.19}$$

where $U'(a)$ is the normal derivative of $U(\mathbf{x})$ along the bump boundary $r = a$, in polar coordinates $\mathbf{r} = (r, \theta)$. Thus, the eigenvalue equation (2.11) becomes

$$(\lambda+1)\Psi(\mathbf{r}) = \frac{a}{|U'(a)|}\int_0^{2\pi} w(|\mathbf{r}-\mathbf{a}'|)\Psi(a,\theta')d\theta', \tag{2.20}$$

where $\mathbf{a}' = (a, \theta')$ in polar coordinates, equivalently $\mathbf{a}' = a(\cos\theta, \sin\theta)$ in Cartesian coordinates. Stability of the bump is thus determined by the spectrum of a compact linear operator acting on continuous, bounded functions $\Psi(r, \theta)$ defined on the disc of radius $r \leq a$. The essential spectrum contains functions $\Psi(\mathbf{r})$ that

vanish on the boundary $\Psi(a,\theta) = 0$ for all θ, so $\lambda = -1$, contributing to no instabilities. We can thus identify the discrete spectrum by setting $\mathbf{r} = \mathbf{a} = (a,\theta)$ in (2.20), so

$$(\lambda+1)\Psi(a,\theta) = \frac{a}{|U'(a)|}\int_0^{2\pi} w\left(2a\sin\left(\frac{\theta-\theta'}{2}\right)\right)\Psi(a,\theta')d\theta',$$

where we have used the identity

$$|\mathbf{a}-\mathbf{a}'| = \sqrt{2a^2-2a^2\cos(\theta-\theta')} = 2a\sin\left(\frac{\theta-\theta'}{2}\right).$$

Any perturbation can be decomposed into the infinite series of Fourier modes $\Psi(a,\theta) = \sum_{n=0}^{\infty} A_n\Psi_n(\theta) + B_n\bar{\Psi}_n(\theta)$, where $\Psi_n(\theta) = \mathrm{e}^{in\theta}$ and $\bar{\Psi}_n(\theta) = \mathrm{e}^{-in\theta}$ [60, 112]. We can thus compute all the eigenvalues of the discrete spectrum by evaluating the expression

$$\lambda_n = -1 + \frac{a}{|U'(a)|}\int_0^{2\pi} w(2a\sin(\theta/2))\mathrm{e}^{-in\theta}d\theta$$

each associated with $\Psi_n(\theta)$ for $n \in \mathbb{Z}_{\geq 0}$. Note, λ_n will always be real, since rescaling $\theta \mapsto 2\theta$:

$$\mathrm{Im}\{\lambda_n\} = -\frac{2a}{|U'(a)|}\int_0^{\pi} w(2a\sin\theta)\sin(2n\theta)d\theta = 0.$$

Therefore, the eigenvalues are real and

$$\lambda_n = \mathrm{Re}\{\lambda_n\} = -1 + \frac{a}{|U'(a)|}\int_0^{2\pi} w(2a\sin(\theta/2))\cos(n\theta)d\theta. \tag{2.21}$$

Note, the bump profile perturbation $\Psi(\mathbf{r},t)$ will be related to the bump boundary perturbation $b(\theta,t)$ via the formula (2.15), as discussed above. The nth order boundary perturbation has D_n symmetry; e.g. $n = 0$ uniformly expands/contracts the bump, $n = 1$ shifts the bump.

By specifying the weight function $w(r)$, we can compute the eigenvalue (2.21) explicitly using Bessel functions to evaluate the integral

$$\begin{aligned}\int_0^{2\pi} w(|\mathbf{a}-\mathbf{a}'|)\cos(n\theta')d\theta' &= \int_0^{2\pi}\left(\int_0^{\infty}\widehat{w}(\rho)J_0(\rho|\mathbf{a}-\mathbf{a}'|)\rho d\rho\right)\cos\theta' d\theta' \\ &= 2\pi\int_0^{\infty}\widehat{w}(\rho)J_n(\rho r)J_n(\rho a)\rho d\rho.\end{aligned}$$

Thus, we can write (2.21) as

$$\lambda_n = -1 + \frac{\int_0^{\infty}\widehat{w}(\rho)J_n(\rho r)J_n(\rho a)\rho d\rho}{\int_0^{\infty}\widehat{w}(\rho)J_1(\rho r)J_1(\rho a)\rho d\rho}.$$

Since we know $\lambda_1 = 0$, the bump will be stable if $\lambda_n < 0$ for all $n \neq 1$. Employing the general weight distribution (2.2), we find

$$\lambda_n = -1 + \frac{\sum_{j=1}^{N} c_j K_n(\alpha_j a) I_n(\alpha_j a)}{\sum_{j=1}^{N} c_j K_1(\alpha_j a) I_1(\alpha_j a)}. \tag{2.22}$$

More specifically, we could focus on the Mexican hat weight distribution (2.9) along with the parameters given in Fig. 2.1**A**. Indeed, checking the formula for the eigenvalues (2.22), we find $\lambda_n < 0$ ($n \neq 1$) for all solutions along the upper branch of wide bump solutions.

2.1.2 Effective equations for stochastic bump motion

We now explore how noise impacts the long term position of bumps in the network (1.4). Previous authors have analyzed the impact of noise on waves in reaction-diffusion [9, 113, 126] and neural field models [16, 19, 90] using small-noise expansions, but those studies tend to be on one-dimensional domains. Noise

causes waves to execute an effective Brownian motion in their instantaneous position. As we will show, this analysis naturally extends to the effective stochastic dynamics of bumps in two-dimensional (2D) domains. The position $\boldsymbol{\Delta}(t) = (\Delta_1(t), \Delta_2(t))$ wanders diffusively, as a 2D random walk, as long as noise is small so that the profile of the bump remains close to the solution of the deterministic system (1.1). As mentioned, this relies upon the neutral stability of the noise free system; different behavior will arise when we break this symmetry with inputs, shown in Section 2.2.

To begin, we assume that the weak additive noise (of $\mathcal{O}(\varepsilon)$) in (1.4) affects the bump in two ways. Both are weak ($\mathcal{O}(\varepsilon)$) compared to the amplitude of the bump, allowing us to exploit regular perturbation theory to analyze the Langevin equation (1.4). First, the bump diffuses from its original position x on long timescales according to the stochastic variable $\boldsymbol{\Delta}(t) = (\Delta_1(t), \Delta_2(t))$ (see Fig. 2.2, for example). Second, there are fluctuations in the bump profile on short timescales [9], according to the expansion $\varepsilon\Phi + \varepsilon^2\Phi_1 + \varepsilon^3\Phi_2 + \cdots$. This suggests the following ansatz for the impact of noise on the bump solution $U(\mathbf{x})$:

$$u(\mathbf{x}, t) = U(\mathbf{x} - \boldsymbol{\Delta}(t)) + \varepsilon\Phi(\mathbf{x} - \boldsymbol{\Delta}(t), t) + \cdots . \tag{2.23}$$

Substituting (2.23) into (1.4) and truncating to $\mathcal{O}(1)$, we find that $U(\mathbf{x})$ still satisfies (2.1). Proceeding to linear order in ε, we find

$$d\Phi(\mathbf{x}, t) = \mathcal{L}\Phi(\mathbf{x}, t) + \varepsilon\nabla U(\mathbf{x}) \cdot d\boldsymbol{\Delta}(t) + dW(\mathbf{x}, t), \tag{2.24}$$

where $\nabla U(\mathbf{x}) = (U_{x_1}(\mathbf{x}), U_{x_2}(\mathbf{x}))^T$ denotes the gradient of $U(\mathbf{x})$ and $\mathcal{L}$ is a non-self-adjoint linear operator of the form

$$\mathcal{L}p(\mathbf{x}) = -p(\mathbf{x}) + \int_{\mathbb{R}^2} w(\mathbf{x}-\mathbf{y}) f'(U(\mathbf{y})) p(\mathbf{y}) d\mathbf{y} \tag{2.25}$$

for any L^2 integrable function $p(\mathbf{x})$ on $\mathbb{R}^2$. We ensure a bounded solution to (2.24) exists by requiring the inhomogeneous part is orthogonal to all elements of the null space of the adjoint operator $\mathcal{L}^*$. The adjoint is defined by utilizing the L^2 inner product

$$\int_{\mathbb{R}^2} \left[\mathcal{L}p(\mathbf{x})\right] q(\mathbf{x}) d\mathbf{x} = \int_{\mathbb{R}^2} p(\mathbf{x}) \left[\mathcal{L}^* q(\mathbf{x})\right] d\mathbf{x},$$

where $p(\mathbf{x})$, $q(\mathbf{x})$ are L^2 integrable on $\mathbb{R}^2$. Thus

$$\mathcal{L}^* q(\mathbf{x}) = -q(\mathbf{x}) + f'(U(\mathbf{x})) \int_{\mathbb{R}^2} w(\mathbf{x}-\mathbf{y}) q(\mathbf{y}) d\mathbf{y}. \tag{2.26}$$

The span of the nullspace of $\mathcal{L}^*$ can be described by two functions, which we can compute explicitly for a general firing rate function. That is, we can find an infinite number of solutions to the null space equation

$$\varphi(\mathbf{x}) = f'(U(\mathbf{x})) \int_{\mathbb{R}^2} w(\mathbf{x}-\mathbf{y}) \varphi(\mathbf{y}) d\mathbf{y}, \tag{2.27}$$

which can always be decomposed into a linear combination of two functions $\varphi_1(\mathbf{x})$ and $\varphi_2(\mathbf{x})$. Specifically, we take $\varphi_1(\mathbf{x}) = f'(U(\mathbf{x}))U_{x_1}(\mathbf{x})$ and $\varphi_2(\mathbf{x}) = f'(U(\mathbf{x}))U_{x_2}(\mathbf{x})$, and note that by plugging into (2.27), we have

$$f'(U(\mathbf{x}))U_{x_j}(\mathbf{x}) = f'(U(\mathbf{x})) \int_{\mathbb{R}^2} w(\mathbf{x}-\mathbf{y}) f'(U(\mathbf{x}))U_{x_j}(\mathbf{y}) d\mathbf{y},$$

which holds due to the equations in (2.12). Thus, we can derive an effective equation for the position variable $\boldsymbol{\Delta}(t)$ by taking the inner product of φ_1 and φ_2 with

both sides of (2.24) to yield

$$\int_{\mathbb{R}^2} f'(U(\mathbf{x}))U_{x_1}(\mathbf{x})\left(U_{x_1}(\mathbf{x})d\Delta_1(t)+U_{x_2}(\mathbf{x})d\Delta_2(t)+\varepsilon dW(\mathbf{x},t)\right)d\mathbf{x}=0 \quad (2.28)$$
$$\int_{\mathbb{R}^2} f'(U(\mathbf{x}))U_{x_2}(\mathbf{x})\left(U_{x_1}(\mathbf{x})d\Delta_1(t)+U_{x_2}(\mathbf{x})d\Delta_2(t)+\varepsilon dW(\mathbf{x},t)\right)d\mathbf{x}=0.$$

Moreover, we can exploit the odd and even symmetries of the spatial derivatives U_{x_1} and U_{x_2} that must hold since $U(\mathbf{x})$ is radially symmetric. Namely, U_{x_1} is odd-symmetric along the x_1-axis and even along the x_2-axis, and U_{x_2} is even-symmetric along the x_1-axis and odd along the x_2-axis. Lastly, $f'(U(\mathbf{x}))$ is radially symmetric since $U(\mathbf{x})$ is. This means $\int_{\mathbb{R}^2} f'(U(\mathbf{x}))U_{x_1}(\mathbf{x})U_{x_2}(\mathbf{x})d\mathbf{x}=0$. This allows us to rearrange the system (2.28), yielding a pair of independent equations for the diffusion of the bump along the x_1 and x_2 axes

$$d\Delta_j(t)=-\varepsilon\frac{\int_{\mathbb{R}^2} f'(U(\mathbf{x}))U_{x_j}(\mathbf{x})dW(\mathbf{x},t)d\mathbf{x}}{\int_{\mathbb{R}^2} f'(U(\mathbf{x}))U_{x_j}^2(\mathbf{x})d\mathbf{x}}, \quad j\in\{1,2\}. \quad (2.29)$$

With the stochastic system (2.29) in hand, we can approximate the effective diffusivity of the bump. First, note that the mean position of the bump averaged across realizations does not change in time ($\langle\boldsymbol{\Delta}(t)\rangle=(0,0)^T$) since noise has mean zero ($\langle W(\mathbf{x},t)\rangle=0$). Computing the variance of the stochastic variable $\boldsymbol{\Delta}(t)$, we find it obeys pure diffusion in two-dimensions:

$$\langle\Delta_j(t)^2\rangle=\varepsilon^2\frac{\int_{\mathbb{R}^2}\int_{\mathbb{R}^2} f'(U(\mathbf{x}))U_{x_j}(\mathbf{x})f'(U(\mathbf{y}))U_{x_j}(\mathbf{y})\langle W(\mathbf{x},t)W(\mathbf{y},t)\rangle d\mathbf{y}d\mathbf{x}}{\left[\int_{\mathbb{R}^2} f'(U(\mathbf{x}))U_{x_j}^2(\mathbf{x})d\mathbf{x}\right]^2}$$
$$\langle\Delta_j(t)^2\rangle=\varepsilon^2 D_j t, \quad j\in\{1,2\}, \quad (2.30)$$

and using the definition of the spatiotemporal noise $W(\mathbf{x},t)$ in (1.5), we find

$$D_j=\frac{\int_{\mathbb{R}^2}\int_{\mathbb{R}^2} f'(U(\mathbf{x}))U_{x_j}(\mathbf{x})f'(U(\mathbf{y}))U_{x_j}(\mathbf{y})C(\mathbf{x}-\mathbf{y})d\mathbf{y}d\mathbf{x}}{\left[\int_{\mathbb{R}^2} f'(U(\mathbf{x}))U_{x_j}^2(\mathbf{x})d\mathbf{x}\right]^2}. \quad (2.31)$$

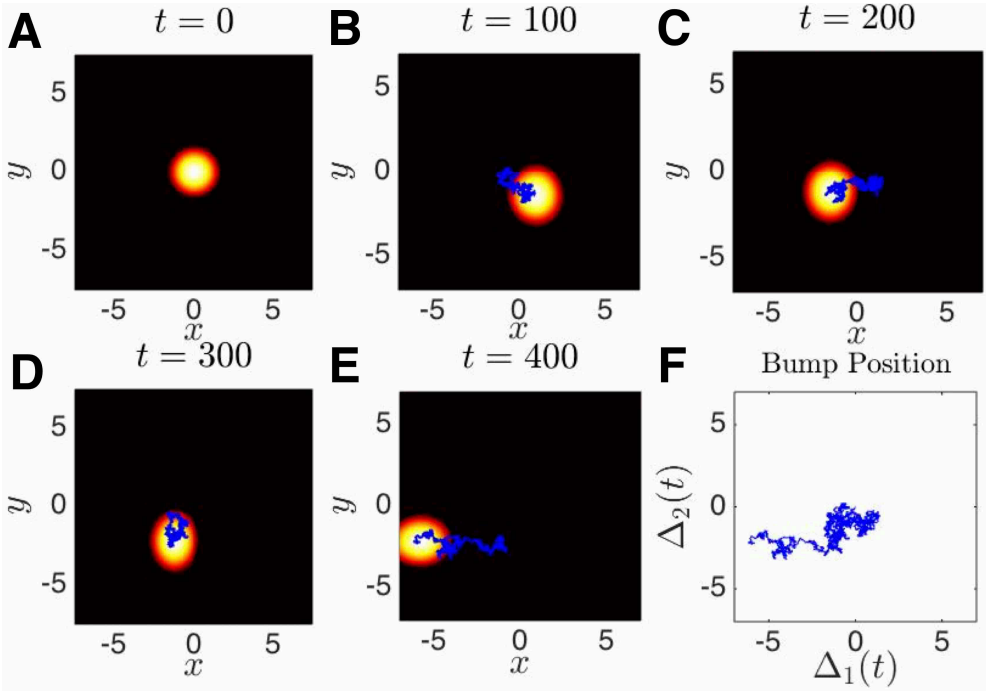

Figure 2.2: Numerical simulation of the stochastic neural field (1.4) on the plane $\mathbb{R}^2$ with Heaviside firing rate (1.3) and Bessel function weight (2.2). (**A**-**E**) Snapshots of a simulation of a bump wandering on the plane, due to noise with spatial correlation function $C(\mathbf{x}) = \cos(\mathbf{x})$, at time points $t = 0, 100, 200, 300, 400$. Thin lines represents the stochastic trajectory of the bump during the time between the previous and current snapshot. (**F**) Plot of the trajectory of the bump centroid for $t \in [0, 400]$ demonstrates how its stochastic trajectory behaves as 2D Brownian motion. Other parameters are $\kappa = 0.2$, $\epsilon = 0.04$, and w is (2.9) with $[c_1, c_2, c_3, c_4] = [5/3, -5/3, -1/2, 1/2]$. We approximate the center of mass of the bump using $\text{argmax}_{\mathbf{x}} u(\mathbf{x}, t)$.

This allows us to calculate the effective diffusion of bumps in the stochastic planar neural field (1.4). We simply need to compute the constituent functions U_{x_j} and $f'(U)$ and evaluate the integrals in (4.3.2), which we now do in the case of Heaviside firing rates (1.3).

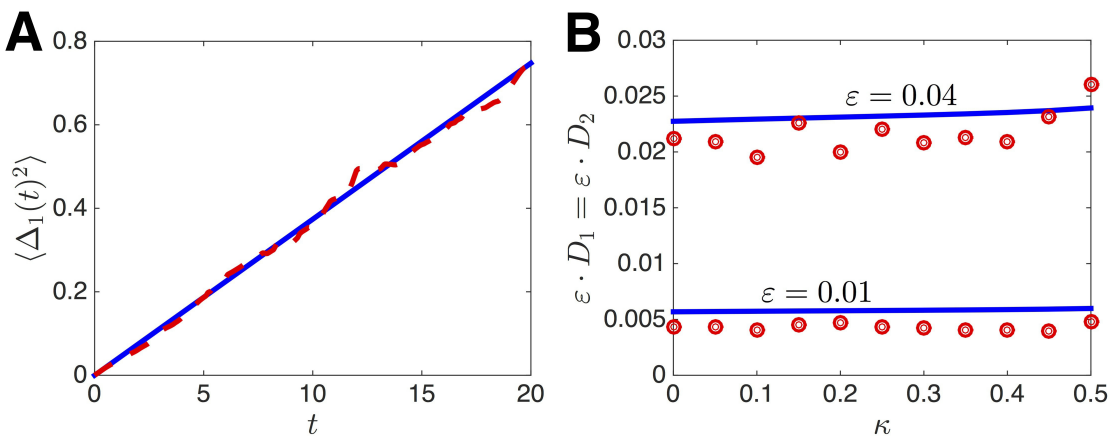

Figure 2.3: Variance of the bump position $\boldsymbol{\Delta}(t) = (\Delta_1(t), \Delta_2(t))$ evolving according to the stochastic model (1.4) with Heaviside firing rate (1.3) and Bessel function weight (2.2). (**A**) Long-term variance $\langle \Delta_1^2 \rangle \rangle$ scales linearly as pure diffusion, and the slope is given by the diffusion coefficient D defined by the formula (2.33). Parameters are $\kappa = 0.2$ and $\varepsilon^2 = 0.05$. (**B**) Plot of the effective diffusion coefficient $\varepsilon^2 \cdot D$ versus the activity threshold κ. The weight function w is (2.9) with $[c_1, c_2, c_3, c_4] = [5/3, -5/3, -1/2, 1/2]$. Numerical variances are computed using 1000 realizations each.

2.1.3 Explicit results for the Heaviside firing rate

We now show that we can explicitly calculate the effective diffusion coefficient (4.3.2) in the case of a Heaviside firing rate function (1.3), weight kernel comprised of modified Bessel functions (2.2), and the following cosine noise correlation function

$$C(\mathbf{x}) = \cos(x_1) + \cos(x_2). \tag{2.32}$$

Analogous to our linear stability calculations, by selecting a Heaviside firing rate function (1.3), we find that the associated functional derivative $f'(U)$ is given by (2.19). Thus, the domain of integration of the terms in (4.3.2) collapse from $\mathbb{R}^2$ to the closed curve $r = a$, in polar coordinates $\mathbf{r} = (r, \theta)$. Furthermore, the spatial

derivatives U_{x_1} and U_{x_2} are given by the formulas (2.17), so that we can simply rewrite the term in the denominator of (4.3.2) as an integral over the angular coordinate θ

$$\left(\int_{\mathbb{R}^2} f'(U(\mathbf{x}))U_{x_j}^2(\mathbf{x})d\mathbf{x}\right)^2 = \left(\frac{1}{|U'(a)|}\int_0^{2\pi}\int_0^{\infty}\delta(r-a)\left[U'(a)\cos\theta\right]^2 r dr d\theta\right)^2$$
$$= \left(\frac{a}{|U'(a)|}\int_0^{2\pi}\left[U'(a)\cos\theta\right]^2 d\theta\right)^2 = a^2\pi^2 U'(a)^2.$$

We can apply a similar approach to the calculation of the numerator of (4.3.2), given by

$$a^2\pi^2 U'(a)^2 D_j = \int_{\mathbb{R}^2}\int_{\mathbb{R}^2} f'(U(\mathbf{x}))U_{x_j}(\mathbf{x})f'(U(\mathbf{y}))U_{x_j}(\mathbf{y})C(\mathbf{x}-\mathbf{y})d\mathbf{y}d\mathbf{x}$$
$$= a^2\int_0^{2\pi}\int_0^{2\pi}\cos\theta\cos\phi\; C(a(\cos\theta,\sin\theta)^T - a(\cos\phi,\sin\phi)^T)d\theta d\phi.$$

Rewriting by using the cosine correlation function (2.32) and utilizing the identity $\cos(x-y) = \cos x\cos y + \sin x\sin y$, we have

$$\pi^2 U'(a)^2 D_j = \left(\int_0^{2\pi}\cos(a\cos\theta)\cos\theta d\theta\right)^2 + \left(\int_0^{2\pi}\cos(a\sin\theta)\cos\theta d\theta\right)^2$$
$$+ \left(\int_0^{2\pi}\sin(a\cos\theta)\cos\theta d\theta\right)^2 + \left(\int_0^{2\pi}\sin(a\sin\theta)\cos\theta d\theta\right)^2.$$

Applying the substitution $v = a\sin\theta$, we find that

$$\int_0^{2\pi}\cos(a\sin\theta)\cos\theta d\theta = \frac{1}{a}\int_{-a}^{a}\cos v dv + \frac{1}{a}\int_a^{-a}\cos v dv = 0,$$
$$\int_0^{2\pi}\sin(a\sin\theta)\cos\theta d\theta = \frac{1}{a}\int_{-a}^{a}\sin v dv + \frac{1}{a}\int_a^{-a}\sin v dv = 0.$$

Furthermore, breaking up the domain of integration of the first summand, we find

$$\int_0^{2\pi} \cos(a\cos\theta)\cos\theta d\theta = \int_{-\frac{\pi}{2}}^{\frac{\pi}{2}} \cos(a\cos\theta)\cos\theta d\theta + \int_{\frac{\pi}{2}}^{\frac{3\pi}{2}} \cos(a\cos\theta)\cos\theta d\theta$$
$$= \int_{-\frac{\pi}{2}}^{\frac{\pi}{2}} \cos(a\cos\theta)\cos\theta d\theta + \int_{-\frac{\pi}{2}}^{\frac{\pi}{2}} \cos(a\cos(\theta+\pi))\cos(\theta+\pi) d\theta$$
$$= \int_{-\frac{\pi}{2}}^{\frac{\pi}{2}} \cos(a\cos\theta)\cos\theta d\theta - \int_{-\frac{\pi}{2}}^{\frac{\pi}{2}} \cos(a\cos\theta)\cos\theta d\theta = 0.$$

Lastly, we must compute the remaining summand, for which we make use of integration by parts

$$\int_0^{2\pi} \sin(\cos\theta)\cos\theta d\theta = 2a\int_0^{\pi} \sin^2\theta\cos(a\cos\theta) d\theta = 2\pi J_1(a),$$

where we have made use of the explicit integral representation of a Bessel function of the first kind of order ν:

$$J_\nu(z) = \frac{1}{\pi}\frac{z^\nu}{(2\nu-1)!!}\int_0^{\pi} \sin^{2\nu}\theta\cos(z\cos\theta) d\theta.$$

Thus, we can finally write

$$D_j = \frac{4J_1(a)^2}{U'(a)^2}, \quad j = 1, 2. \tag{2.33}$$

Effective diffusion along both the x_1 and x_2 axes is identical, due to radial symmetry of the bump along with the D_4 symmetry of the correlation function (2.32). We demonstrate our analytical results, in comparison to statistics from numerical simulations, in Fig. 2.3.

2.2 Stimulus-pinned bumps in $\mathbb{R}^2$

In this section, we explore how the interaction of external inputs and noise determines the stochastic dynamics of bumps. Previous work has shown in one-dimensional domains that both external inputs [90] and coupling between bumps in multiple layers [24, 86, 88] can help stabilize bumps to the translating perturbations of noise. Inputs pin bumps in place so their motion is mostly restricted to the peak(s) of the input function, and the stochastic variable describing the bump's location can be approximated with a mean-reverting (Ornstein-Uhlenbeck) process. Thus, we consider an external stationary stimulus $I(\mathbf{x})$ acting on our system (1.8). The primary forms of input we employ are a radially symmetric Gaussian

$$I(\mathbf{x}) = I(r) = A_0 \mathrm{e}^{-r^2/\sigma^2}, \tag{2.34}$$

and a translationally symmetric Gaussian

$$I(\mathbf{x}) = I(x_1) = A_0 \mathrm{e}^{-x_1^2/\sigma^2}, \tag{2.35}$$

where $I(x_1)$ denotes independence from the second coordinate of the spatial vector $\mathbf{x} = (x_1, x_2)$. We begin by reviewing the existence and stability of radially symmetric bumps in the noise free system ($\varepsilon \to 0$), as this foreshadows the impact of inputs on the stochastic dynamics of bumps. Essentially, the local stability of bumps to translating perturbations is altered by the input's spatial heterogeneity.

2.2.1 Existence and stability of bumps

We begin by constructing the modified equations for radially symmetric bump solutions $u(\mathbf{x},t) = U(\mathbf{x}) = U(r)$ to the model (1.8) in the absence of noise ($\varepsilon \to 0$). Previous work has shown that inputs can stabilize stationary bumps in purely excitatory neural field models that incorporate linear adaptation [60] by altering the evolution of expanding/contracting ($O(2)$-symmetric) perturbations to bump profiles. Here, we show inputs stabilize bumps to translating (D_1-symmetric) perturbations. We focus on the case where the external input $I(\mathbf{x})$ is rotationally symmetric, so in polar coordinates, $I(r,\theta) = I(r,\theta+s)$ for $s \in [0,2\pi]$. Thus, our stationary bump solution satisfies the stationary equation

$$U(||\mathbf{x}||) = \int_{\mathbb{R}^2} w(\mathbf{x}-\mathbf{y}) f(U(\mathbf{y}))d\mathbf{y} + I(\mathbf{x}), \tag{2.36}$$

and by changing to polar coordinates $\mathbf{x} = (x_1,x_2) \mapsto (r,\theta)$, we have

$$U(r) = \int_0^{2\pi}\int_0^{\infty} w(|\mathbf{r}-\mathbf{r}'|) f(U(\mathbf{r}'))r'dr'd\theta' + I(r). \tag{2.37}$$

Assuming a Heaviside firing rate function (1.3), the integral in (2.37) collapses to a compact domain

$$U(r) = \int_0^{2\pi}\int_0^{a} w(|\mathbf{r}-\mathbf{r}'|) r'dr'd\theta' + I(r), \tag{2.38}$$

where $r \equiv a$ defines the boundary bump as in the input-free case (2.4). We can evaluate (2.38) explicitly by assuming the weight function formula is a sum of modified Bessel functions (2.2), finding

$$U(r) = 2\pi a \sum_{j=1}^{N} c_k \mathcal{I}(a,r,\alpha_k) + I(r),$$

where $\mathcal{I}(a, r, s)$ is defined by the formula (2.7). To relate the bump radius a to the threshold κ of the Heaviside firing rate function (1.3), we apply the condition $U(a) = \kappa$, which can be written

$$U(a) = 2\pi a \sum_{j=1}^{N} \frac{c_k}{\alpha_k} I_1(\alpha_k a) K_0(\alpha_k a) + I(a) = \kappa.$$

One can then solve this nonlinear equation using numerical root finding.

To determine the stability of the input-driven stationary bump solution (2.37), we study the impact of small smooth pertubations away from the stationary solution by employing the ansatz $u(\mathbf{x}, t) = U(\mathbf{x}) + \varepsilon\Psi(\mathbf{x}, t)$ where $\varepsilon \ll 1$. Substituting this expansion into (1.8), when $W \equiv 0$, and truncating to linear order yields the equation (2.10) as in the input-free case. The main difference is that bumps are defined by (2.37), incorporating the input term $I(\mathbf{x})$. Furthermore, applying separation of variables $\Psi(\mathbf{x}, t) = \Psi(\mathbf{x})e^{\lambda t}$ and rearranging terms yields the eigenvalue equation (2.11). However, when $U(\mathbf{x})$ satisfies (2.37), such bumps are no longer neutrally stable to perturbations that shift their position. It is straightforward to show this in the case of a Heaviside firing rate function (1.3), in which case eigenvalues associated with the Fourier modes $\Psi_n(\theta) = e^{in\theta}$ are given by the expression (2.21), so the eigenvalue λ_1 associated with shifts perturbations $\Psi_1(\theta) = e^{i\theta}$ is given by the formula

$$\lambda_1 = -1 + \frac{a}{|U'(a)|} \int_0^{2\pi} w(2a\sin(\theta/2))\cos(\theta)d\theta, \tag{2.39}$$

and since $U(r)$ is given by (2.38), then

$$|U'(a)| = a \int_0^{2\pi} w(2a\sin(\theta/2))\cos(\theta)d\theta - I'(a).$$

Thus, we can rewrite (2.39) as

$$\lambda_1 = \frac{I'(a)}{a\int_0^{2\pi} w(2a\sin(\theta/2))\cos(\theta)d\theta - I'(a)} < 0,$$

where the inequality holds when $I(r)$ is a monotone decreasing function, as we have assumed for the radially symmetric Gaussian (2.34). This indicates the bump will be linearly stable to perturbations that alter its position, indicative of the mean-reverting stochastic dynamics that emerge when weak noise is considered in (1.8). Eigenvalues of all Fourier modes, representing azimuthal perturbations of the bump (2.38), can be computed numerically from the formula (2.21).

2.2.2 Stochastic bump motion in the presence of weak inputs

Our analysis of the stochastic motion of bumps in the stationary input-driven system (1.8) employs a similar approach to our analysis of the input-free ($I(\mathbf{x}) \equiv 0$) system (1.4). However, the effective equations that emerge are no longer translationally invariant due to the spatial heterogeneity imposed by the input $I(\mathbf{x})$. Our analysis assumes that inputs are weak, having the same amplitude as the noise term [24], so we write $I(\mathbf{x}) = \varepsilon\tilde{I}(\mathbf{x})$. In this case, the $\mathcal{O}(1)$ terms are identical to the input-free deterministic system (1.1) with stationary bump solution (2.1). We can then derive a system of nonlinear stochastic differential equations for the effective motion of the bump's position $\boldsymbol{\Delta}(t) = (\Delta_1(t), \Delta_2(t))$, which we can then truncate to a multivariate Ornstein-Uhlenbeck (OU) process assuming $\boldsymbol{\Delta}(t)$ remains small. This captures the fact that bumps are systematically drawn back to the location of the peak(s) of the external input as demonstrated in Fig. 2.4 and

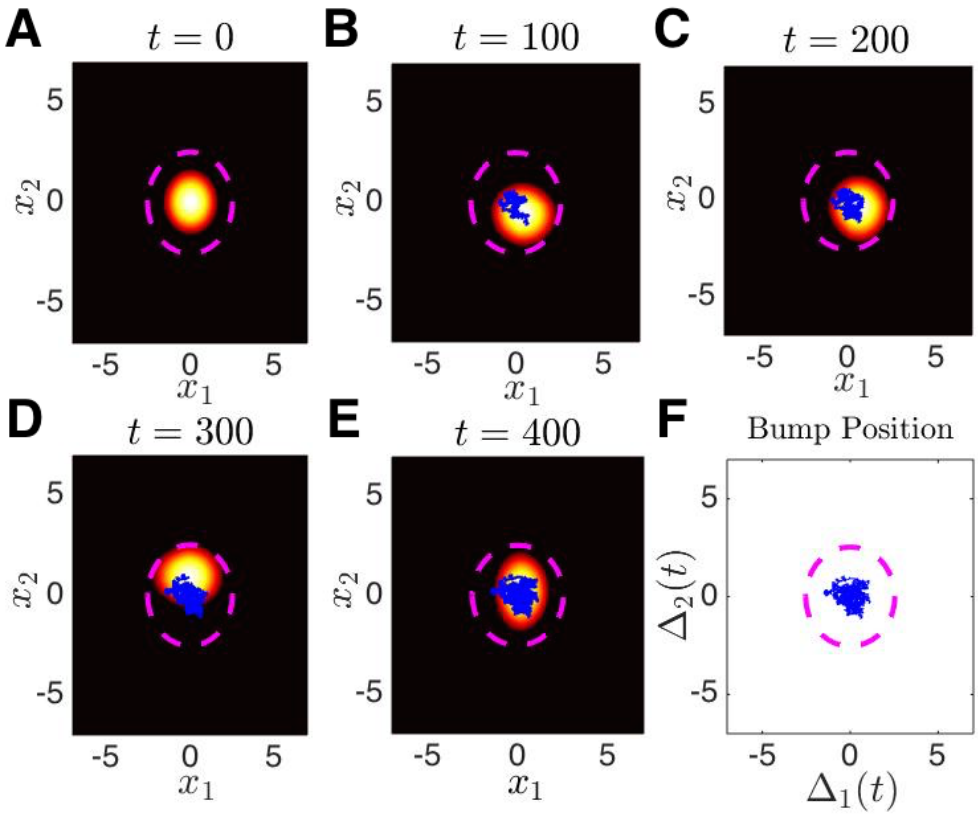

Figure 2.4: Numerical simulation of the stochastic neural field (1.8) on the plane $\mathbb{R}^2$ with Heaviside firing rate (1.3) and Bessel function weight (2.2), subject to radially symmetric Gaussian input (2.34). Thin lines represents the stochastic trajectory of the bump during the time between the previous and current snapshot. Dashed circle is a plot of the level set $I(\mathbf{x}) = \kappa$. (**A**-**E**) Snapshots of a simulation of a bump wandering on the plane, due to noise with spatial correlation function $C(\mathbf{x}) = \cos(\mathbf{x})$, at time points $t = 0, 100, 200, 300, 400$. Input causes the trajectory to stay in the vicinity of the peak of the radially symmetric Gaussian (2.34) at the origin $(x_1, x_2) = (0, 0)$. (**F**) Plot of the trajectory of the bump centroid for $t \in [0, 400]$ demonstrates how its stochastic trajectory behaves as 2D OU process. Parameters are $\varepsilon^2 = 0.04$, $\kappa = 0.2$, $A_0 = 1$, $\sigma = 2$, and w is (2.9) with $[c_1, c_2, c_3, c_4] = [5/3, -5/3, -1/2, 1/2]$.

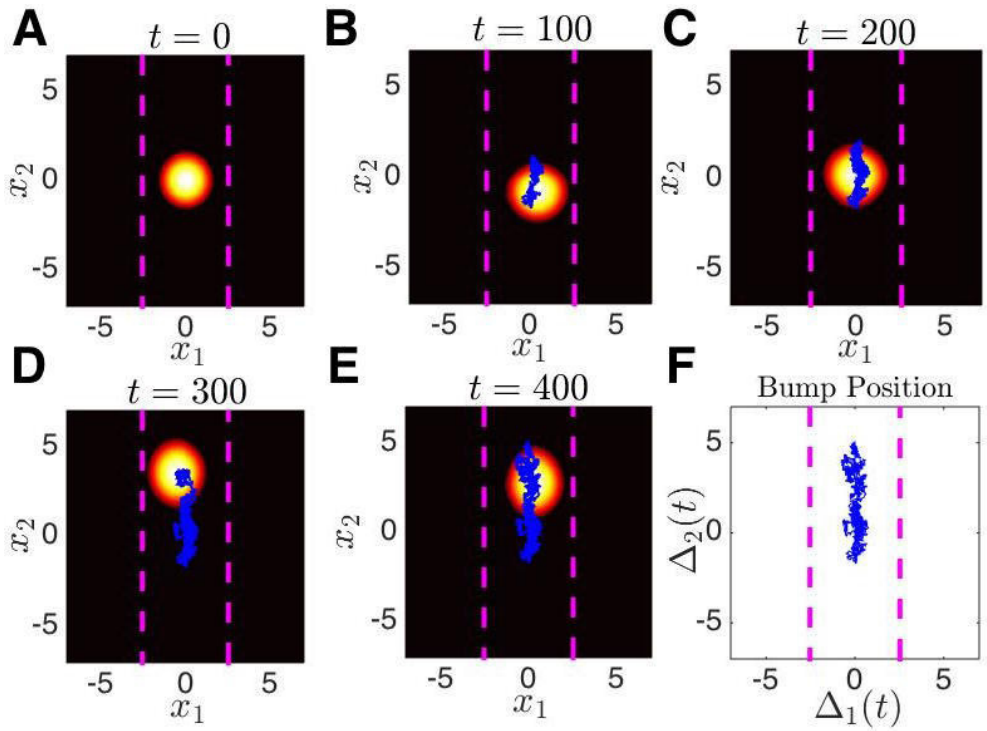

Figure 2.5: Numerical simulation of the stochastic neural field (1.8) on the plane $\mathbb{R}^2$ with Heaviside firing rate (1.3) and Bessel function weight (2.2), subject to translationally symmetric Gaussian input (2.35). Thin lines represents the stochastic trajectory of the bump during the time between the previous and current snapshot. Dashed lines are a plot of the level set $I(\mathbf{x}) = \kappa$. (**A**-**E**) Snapshots of a simulation of a bump wandering on the plane, due to noise with spatial correlation function $C(\mathbf{x}) = \cos(\mathbf{x})$, at time points $t = 0, 100, 200, 300, 400$. Input cause the trajectory to stay in the vicinity of the peak of the translationally symmetric Gaussian (2.35) along the line $x_1 = 0$. (**F**) Plot of the trajectory of the bump centroid for $t \in [0, 400]$ demonstrates how its stochastic trajectory behaves as 2D OU process. Parameters are $\varepsilon^2 = 0.04$, $\kappa = 0.2$, $A_0 = 1$, $\sigma = 2$, and w is (2.9) with $[c_1, c_2, c_3, c_4] = [5/3, -5/3, -1/2, 1/2]$.

Fig. 2.5.

Employing the ansatz (2.23), assuming the bump's profile has fluctuations $\varepsilon\Phi(\mathbf{x},t)$ on fast timescales and stochastically varying position $\boldsymbol{\Delta}(t)$ on longer timescales, we truncate to linear order in ε and find

$$d\Phi(\mathbf{x},t) = \mathcal{L}\Phi(\mathbf{x},t) + \varepsilon\nabla U(\mathbf{x})\cdot d\boldsymbol{\Delta}(t) + dW(\mathbf{x},t) + \tilde{I}(\mathbf{x}+\boldsymbol{\Delta}(t)), \tag{2.40}$$

where $\nabla U(\mathbf{x}) = (U_{x_1}(\mathbf{x}), U_{x_2}(\mathbf{x}))^T$ and $\mathcal{L}$ is the non-self-adjoint linear operator (2.25) with adjoint $\mathcal{L}^*$ given by (2.26). As before, the nullspace of $\mathcal{L}^*$ is spanned by the two functions $\varphi_1(\mathbf{x}) = f'(U(\mathbf{x}))U_{x_1}(\mathbf{x})$ and $\varphi_2(\mathbf{x}) = f'(U(\mathbf{x}))U_{x_2}(\mathbf{x})$. Thus, we can enforce solvability of the $\mathcal{O}(\varepsilon)$ equation (2.40) to yield the pair of nonlinear stochastic differential equations

$$d\Delta_j(t) = -\varepsilon G_j(\boldsymbol{\Delta}(t))dt - \varepsilon d\mathcal{W}_j(t), \tag{2.41}$$

where the restorative dynamics of the input are described by the nonlinear function

$$G_j(\boldsymbol{\Delta}) = \frac{\int_{\mathbb{R}^2} f'(U(\mathbf{x}))U_{x_j}(\mathbf{x})\tilde{I}(\mathbf{x}+\boldsymbol{\Delta})d\mathbf{x}}{\int_{\mathbb{R}^2} f'(U(\mathbf{x}))U_{x_j}^2(\mathbf{x})d\mathbf{x}}, \quad j\in\{1,2\}, \tag{2.42}$$

and spatiotemporal noise provides the effective noise perturbations to the bump position through the white noise terms

$$\mathcal{W}_j(t) = \frac{\int_{\mathbb{R}^2} f'(U(\mathbf{x}))U_{x_j}(\mathbf{x})W(\mathbf{x},t)d\mathbf{x}}{\int_{\mathbb{R}^2} f'(U(\mathbf{x}))U_{x_j}^2(\mathbf{x})d\mathbf{x}}, \quad j\in\{1,2\}. \tag{2.43}$$

Note that $\langle d\mathcal{W}_j(t)\rangle = 0$ and $\langle d\mathcal{W}(t)d\mathcal{W}(s)\rangle = 2D_j\delta(t-s)dtds$ with D_j given by (4.3.2). As we demonstrated in our analysis of stimulus-driven bump existence and stability, $\bar{\boldsymbol{\Delta}} = (0,0)$ is a stable fixed point of the noise-free system $\dot{\Delta}_j(t) =$

$-\varepsilon G_j(\boldsymbol{\Delta}(t))$; $j = 1, 2$. Linearizing about this solution yields the multivariate OU process

$$d\Delta_j(t) + \varepsilon\beta_j\Delta_j(t)dt = \varepsilon d\mathcal{W}_j(t), \tag{2.44}$$

where

$$\beta_j = G'(0) = \frac{\int_{\mathbb{R}^2} f'(U(\mathbf{x}))U_{x_j}(\mathbf{x})\tilde{I}_{x_j}(\mathbf{x})d\mathbf{x}}{\int_{\mathbb{R}^2} f'(U(\mathbf{x}))U_{x_j}^2(\mathbf{x})d\mathbf{x}}, \quad j \in \{1, 2\}, \tag{2.45}$$

assuming $\int_{\mathbb{R}^2} f'(U(\mathbf{x}))U_{x_j}(\mathbf{x})\tilde{I}_{x_k}(\mathbf{x})d\mathbf{x} \equiv 0$, when $j \neq k$, which is the case when $I(\mathbf{x})$ is even symmetric along the x_1 and x_2 directions as (2.34) and (2.35) are. In this case, we can use standard properties of an OU process to compute the mean $\langle\Delta_j(t)\rangle = \Delta_j(0)e^{-\varepsilon\beta_j t}$ and variance

$$\langle\Delta_j(t)^2\rangle = \frac{\varepsilon D_j}{\beta_j}\left(1 - e^{-2\varepsilon\beta_j t}\right), \tag{2.46}$$

so the variance $\langle\Delta_j(t)^2\rangle$ will approach a constant $\varepsilon D_j/\beta_j$ as $t \to \infty$ and the mean converges to the fixed point $\bar{\boldsymbol{\Delta}} = (0, 0)$. Thus, we can describe the stochastic dynamics of the position $\boldsymbol{\Delta}(t)$ approximately using a multivariate OU process (2.44) or with higher order corrections through the nonlinear SDE (2.41).

2.2.3 Explicit results for the Heaviside firing rate

We can explicitly calculate the variances $\langle\Delta_j(t)^2\rangle$ as described by the formula (2.46) in the case of a Heaviside firing rate function (1.3), Bessel function weight kernel (2.2), and cosine noise correlations (2.32). Thus, the derivative $f'(U)$ is given by (2.19), spatial derivatives U_{x_j} ($j = 1, 2$) are given by (2.17), and the diffusion coefficients D_j ($j = 1, 2$) are defined by the formula (2.33). Again, the impact

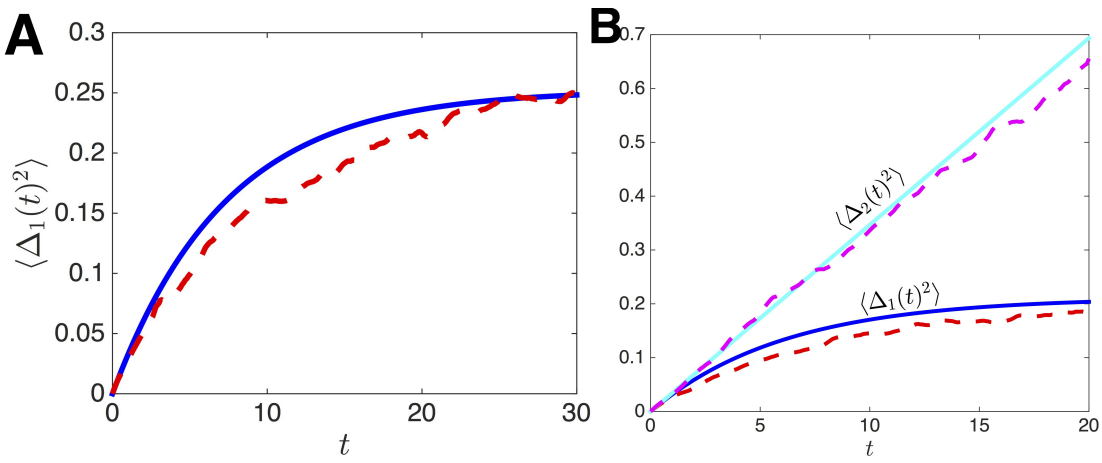

Figure 2.6: Variance of the bump position $\boldsymbol{\Delta}(t) = (\Delta_1(t), \Delta_2(t))$ evolving according to the stochastic model (1.8) with Heaviside firing rate (1.3) and Bessel function weight (2.2). (**A**) Long-term variance $\langle \Delta_1(t)^2 \rangle$ saturates according to a multivariate Ornstein-Uhlenbeck process when input is given by a radially symmetric Gaussian (2.34). Results from numerical simulations (dashed line) are well matched to our theoretical result (2.46). An identical picture exists for $\langle \Delta_2(t)^2 \rangle$, the variance along the x_2 direction. (**B**) Variance along the x_2 direction $\langle \Delta_2(t)^2 \rangle$ climbs linearly and variance $\langle \Delta_1(t)^2 \rangle$ along the x_1 direction saturates when input is given by a translationally symmetric Gaussian (2.35). Parameters are $\kappa = 0.2$, $A_0 = 1$, $\sigma = 2$, and w is (2.9) with $[c_1, c_2, c_3, c_4] = [5/3, -5/3, -1/2, 1/2]$. Numerical calculations of variance use 1000 realizations each.

of spatiotemporal noise in bump dynamics is primarily determined by interactions that occur at the bump boundary $r \equiv a$. Furthermore, in the case of a radially symmetric input such as the Gaussian (2.34), we can compute the coefficients

$$\beta_j = \frac{\int_{\mathbb{R}^2} f'(U(\mathbf{x}))U_{x_j}(\mathbf{x})\tilde{I}_{x_j}(\mathbf{x})d\mathbf{x}}{\int_{\mathbb{R}^2} f'(U(\mathbf{x}))U_{x_j}^2(\mathbf{x})d\mathbf{x}} = \frac{a\pi\tilde{I}'(a)}{a\pi U'(a)} = \frac{\tilde{I}'(a)}{U'(a)}, \quad j = \{1, 2\}. \tag{2.47}$$

Therefore, in the long time limit, the variances $\langle \Delta_j(t)^2 \rangle$ will saturate to

$$\lim_{t\to\infty} \langle \Delta_j(t)^2 \rangle = \frac{\varepsilon^2 D_j}{\beta_j} = \frac{4\varepsilon^2 J_1(a)^2}{I'(a)U'(a)}. \tag{2.48}$$

We compare our explicit calculation of the variance to results from numerical calculations for the case of a radially symmetric Gaussian (2.34) in Fig. 2.6**A**.

In the case of the translationally symmetric Gaussian (2.35), we have $I_{x_2}(\mathbf{x}) \equiv 0$, so $\beta_2 \equiv 0$. As a result $\langle \Delta_2(t)^2 \rangle = \varepsilon^2 D_2 t$, and the variance is only mean reverting along the x_1 direction, as demonstrated by the numerical simulation in Fig. 2.5. The coefficient describing the systematic dynamics along the x_1 direction is

$$\varepsilon\beta_1 = \frac{2aA_0 \int_0^{2\pi} \exp\left[-a^2\cos^2\theta/\sigma^2\right]\cos^2\theta d\theta}{\pi\sigma^2|U'(a)|}, \tag{2.49}$$

which can be computed using quadrature to evaluate the formula (2.46) for $j = 1$. We compare these theoretical results with averages across numerical realizations in Fig. 2.6**B**. Thus, the variance along the x_1-direction saturates, while the variance along the x_2-direction indefinitely climbs linearly.

2.2.4 Statistics of the nonlinear Langevin equation

More accurate approximations of the variances $\langle \Delta_j^2 \rangle$ can be obtained by performing an analysis of the full nonlinear Langevin equation (2.41) for the stochastic motion of the input-driven bump. In [24], it was recently shown this can be particularly useful when there are multiple distinct fixed points of the noise free equations $\dot{\Delta}_j = -\varepsilon G_j(\Delta)$ $(j = 1, 2)$, as noise can eventually cause a phase-slip so a linearized approximation is no longer valid. Here, we demonstrate that a derivation of nonlinear Langevin equations can be extended to spatiotemporal patterns evolving in two-dimensions. Also, even if the position $\boldsymbol{\Delta}(t) = (\Delta_1(t), \Delta_2(t))$ does remain close to a single stable fixed point, the stationary probability density $P_0(\boldsymbol{\Delta})$ of (2.41) can be considerably different than that of the truncated OU process (2.44). Thus, we briefly present the computation of this stationary probability density

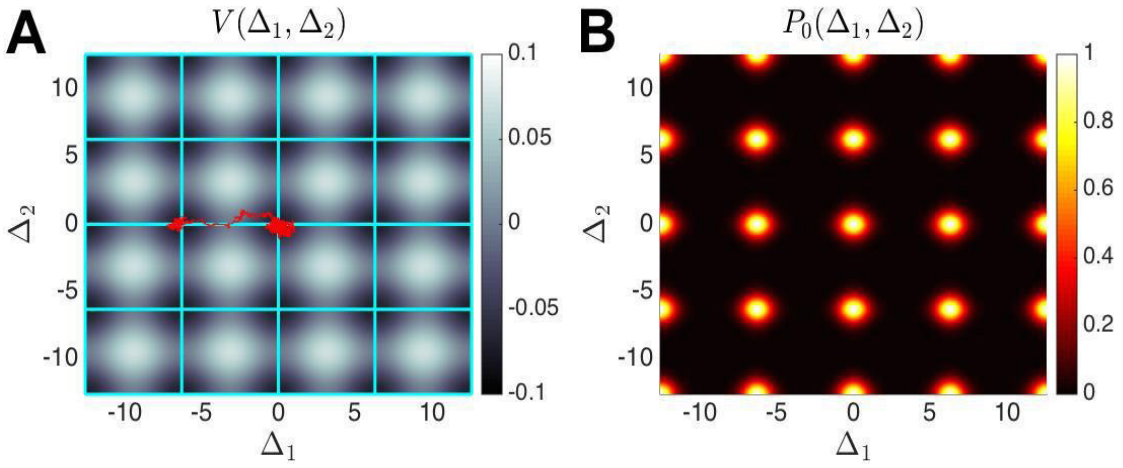

Figure 2.7: Nonlinear dynamics in the input driven neural field (1.8) on the plane $\mathbb{R}^2$ with Heaviside firing rate (1.3) and Bessel function weight (2.2), subject to the periodic input $\tilde{I}(\mathbf{x}) = 0.3(\cos x_1 + \cos x_2)$. (**A**) Bump position (thin line) sampled from a single realization of the system (1.8) for $t \in [0, 4000]$, superimposed on a plot of the potential $V(\boldsymbol{\Delta})$. Over long periods of time, the stochastically-driven position of bumps tends to dwell primarily in the vicinity of minima of the potential $V(\boldsymbol{\Delta})$ defined by (2.57). However, there are rare events whereby the bump transitions to a neighboring potential well. Thick lines represent the paths of least action between attractors at $(2m\pi, 2n\pi)$, $m, n \in \mathbb{Z}$. (**B**) Re-normalized stationary probability density $P_0(\mathbf{x})$ (so that $||P_0(\mathbf{x})||_{max} = 1$, otherwise $P_0(\mathbf{x})$ would be infinitesimally small everywhere) has peaks at the minima of the potential function $V(\boldsymbol{\Delta})$. Parameters are $\varepsilon^2 = 0.025$, $\kappa = 0$, and weight w is (2.9) with $[c_1, c_2, c_3, c_4] = [5/3, -5/3, -1/2, 1/2]$.

$P_0(\boldsymbol{\Delta})$ by utilizing the associated Fokker-Planck equation, saving a more extensive study for future work.

The stochastic dynamics is shaped by an underlying potential function $V(\boldsymbol{\Delta})$, which is the solution to the pair of equations

$$\frac{dV}{d\Delta_1} = \varepsilon G_1(\boldsymbol{\Delta}), \quad \frac{dV}{d\Delta_2} = \varepsilon G_2(\boldsymbol{\Delta}), \tag{2.50}$$

so that the attractors of the noise free system are the minima of $V(\boldsymbol{\Delta})$. While (2.50)

cannot always be solved explicitly, we will present an example below where they can, for illustration. To analyze the system, we reformulate (2.41) as an equivalent Fokker-Planck equation [67]

$$\frac{\partial P(\boldsymbol{\Delta},t)}{\partial t} = \sum_{j=1}^{2}\left\{\frac{\partial}{\partial \Delta_j}\left[\varepsilon G_j(\boldsymbol{\Delta})P(\boldsymbol{\Delta},t)\right] + \varepsilon^2 D_j \frac{\partial^2 P(\boldsymbol{\Delta},t)}{\partial \Delta_j^2}\right\}, \tag{2.51}$$

where $P(\boldsymbol{\Delta},t)$ is the probability of finding the bump at position $\boldsymbol{\Delta} = (\Delta_1,\Delta_2)$ at time t. Assuming there is a single stable attractor defined by the potential $V(\boldsymbol{\Delta})$, in the long time limit

$$\lim_{t\to\infty} P(\boldsymbol{\Delta},t) = P_0(\boldsymbol{\Delta}) = \chi \exp\left[-\frac{V(\boldsymbol{\Delta})}{\varepsilon^2 D}\right], \tag{2.52}$$

in the case of rotationally symmetric noise $D_1 = D_2 = D$, where χ is a normalization factor such that $\int_{\mathbb{R}^2} P_0(\boldsymbol{\Delta})d\boldsymbol{\Delta} = 1$. The long time variance $\langle ||\boldsymbol{\Delta}||^2\rangle = \langle \Delta_1^2\rangle + \langle \Delta_2^2\rangle$ is thus given by the integral

$$\langle \Delta_1^2\rangle + \langle \Delta_2^2\rangle = \int_{\mathbb{R}^2} (\Delta_1^2 + \Delta_2^2) P_0(\boldsymbol{\Delta})d\boldsymbol{\Delta}. \tag{2.53}$$

To demonstrate our analysis on a specific example, we focus on an input which allows explicit computation of the steady state distribution. Thus, we take the external input $\tilde{I}(\mathbf{x}) = A_0(\cos x_1 + \cos x_2)$ and assume we then wish to compute the statistics of the stationary probability density $P_0(\boldsymbol{\Delta})$. Furthermore, we take the Heaviside firing rate function (1.3), then the integrals (2.42) can be simplified by making the substitutions $x_1 = r\cos\theta$ and $x_2 = r\sin\theta$ and integrating out the radial coordinate r, so

$$G_1(\boldsymbol{\Delta}) = \frac{U'(a)\int_0^{2\pi}\cos(\theta)\tilde{I}(\mathbf{a}+\boldsymbol{\Delta})d\theta}{U'(a)^2\int_0^{2\pi}\cos^2\theta d\theta} = \frac{1}{U'(a)\pi}\int_0^{2\pi}\cos(\theta)\tilde{I}(\mathbf{a}+\boldsymbol{\Delta})d\theta \tag{2.54}$$

$$G_2(\boldsymbol{\Delta}) = \frac{U'(a)\int_0^{2\pi}\sin(\theta)\tilde{I}(\mathbf{a}+\boldsymbol{\Delta})d\theta}{U'(a)^2\int_0^{2\pi}\sin^2\theta d\theta} = \frac{1}{U'(a)\pi}\int_0^{2\pi}\sin\theta\tilde{I}(\mathbf{a}+\boldsymbol{\Delta})d\theta, \tag{2.55}$$

where $\mathbf{a} = (a, \theta)$. Selecting the doubly periodic function for our external input $\tilde{I}(\mathbf{x}) = A_0(\cos x_1 + \cos x_2)$, we generate terms similar to those that arose in our explicit calculation of the diffusion coefficient D_j (2.33). Subsequently, we find we can evaluate these explicitly, to arrive at the compact expression

$$G_j(\boldsymbol{\Delta}) = -\frac{2A_0 J_1(a)}{U'(a)} \sin(\Delta_j), \quad \{j = 1, 2\}. \tag{2.56}$$

Thus, the positions Δ_1 and Δ_2 evolve independently in nonlinear system (2.41), in the case of this specific input function. Thus, it is straightforward to evaluate the potential function as the solution to (2.50), finding

$$V(\boldsymbol{\Delta}) = -\frac{2\varepsilon A_0 J_1(a)}{|U'(a)|} \left[\cos(\Delta_1) + \cos(\Delta_2)\right], \tag{2.57}$$

which can then be utilized to compute the statistics of the stationary probability density (2.52). We demonstrate that stochastic trajectories of the bump tend to dwell mostly in the minima of the potential function defined by (2.57) in Fig. 4.7**A**. Such durations are interrupted by abrupt transitions of the bump between neighboring wells as in the one-dimensional case [90]. An example of the rescaled stationary probability density is given in Fig. 4.7**B**. We save a more thorough analysis of these results for subsequent work.

2.3 Conclusion

We have analyzed the impact of additive noise on the stochastic motion of bumps in planar neural field equations. In networks with no spatial heterogeneity, noise causes bumps to wander according to two-dimensional Brownian motion. The

diffusion coefficient associated with this motion can be approximated using an asymptotic expansion that treats the impact of noise perturbatively. Assuming the bump retains its profile, to first order, we can derive an effective diffusion equation for the bump's position as a function of time. Notably, the dynamics of the bumps can be separated into diffusion along the canonical directions (x_1, x_2) in $\mathbb{R}^2$. In the presence of spatially heterogeneous external inputs, the stochastic bumps no longer obey dynamics well described by pure diffusion. Rather, bumps are attracted to the local maxima of the input functions, so their motion can be approximated by multivariate Ornstein-Uhlenbeck processes. In particular, we find that the geometry of the external inputs define the manifold to which bumps are attracted. Radially symmetric inputs attract bumps to a single point and translationally symmetric peaked inputs attract bumps to a one-dimensional line through $\mathbb{R}^2$.

In Chapter 3, we aim to extend this work by introducing a mechanism to reduce error as a result of noise or heterogeneity. Since weak inputs can help guide the location of bumps, it is possible other networks in the brain are responsible for reducing diffusion caused by noise. Notably, this has applications in short term memory relating to spatial navigation. Thus, we also include a velocity input, which causes the bump to propagate around the domain. To simplify our analysis, we restrict our modified model to a one-dimensional domain on a periodic domain ($x \in [-\pi, \pi]$), with the expectation that our results could be extended to two-dimensional systems left as future work. We find our modified model performs adequately under a robust set of parameters.

Chapter 3

Incorporating Sensory Feedback

3.1 Sensory control in velocity-integrating place cell networks

In this chapter, we employ a neural field model of velocity integration that sustains a bump attractor of neural activity in the absence of any inputs. Amari pioneered the scalar neural field model as a reduction of the excitatory-inhibitory model of [159], but the incorporation of velocity inputs that shift the bump around the spatial domain is more recent. Originally developed as a model of the head direction system [168], velocity-integrating networks introduce an external input that alters the shape of the recurrent architecture [108]. As a result, a moving bump, rather than a stationary bump, becomes the stable solution to the model equations. This model has since been extended to account for place fields and grid cell fields in planar systems [30, 127]. The fully general form of our neural

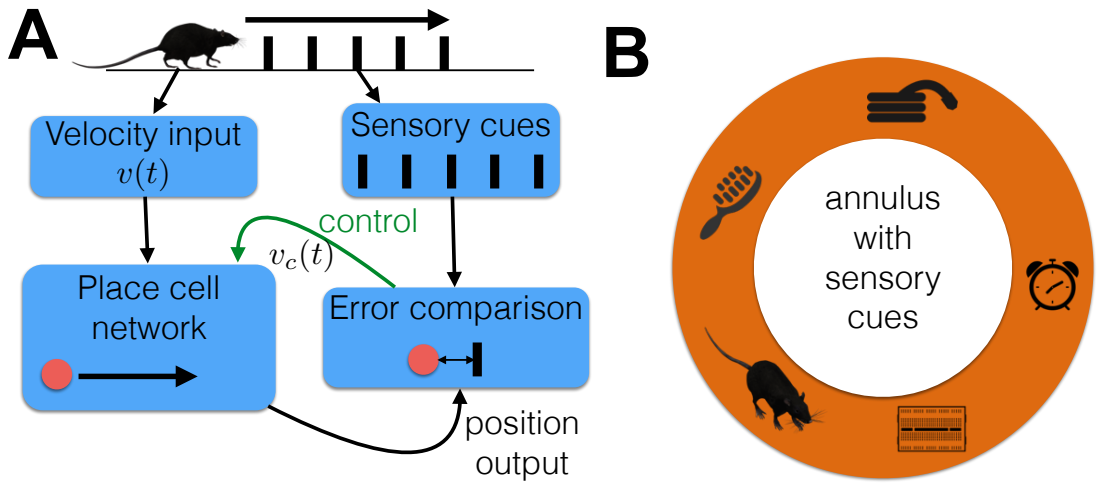

Figure 3.1: Mammalian spatial navigation network with sensory feedback. The animal utilizes its own velocity to update its remembered position (path integration) and corrects this memory with sensory cues that serve as position landmarks. (**A**) Schematic of the underlying neuronal network demonstrates the place cell network receives direction input from the animal's velocity signal $v(t)$. Its position estimate is compared with the true position read-out from a sensory cue, and this error is then used to generate a control input signal $v_c(t)$ back into the place cell network. (**B**) Illustration of the experiments by [12], showing an annular track with various objects placed in the environment to provide the animal with sensory cues.

field model is given

$$du(x,t) = -\Big[u(x,t) + \int_{-\pi}^{\pi} w(x,y) f(u(y,t)) dy + \tilde{v}(t) \int_{-\pi}^{\pi} w_v(x-y) f(u(y,t)) dy \Big] dt + \epsilon dW(x,t), \qquad (3.1)$$

where $u(x,t)$ denotes the total synaptic activity at a position $x \in [-\pi, \pi]$ at time t. The variable x labels the position of neurons in the network as well as a corresponding location in the environment, so the domain $\Omega = [-\pi, \pi]$ is taken to be periodic as it represents an annular track (Fig. 3.1**B**).

The function $w(x, y)$ represents the synaptic connectivity between neurons, which we model as a translationally symmetric unimodal function w_0, modified by spatial heterogeneity w_u with strength σ or odd asymmetry ϕ, so

$$w(x, y) := (1 + \sigma w_u(y))w_0(x - y - \phi) \tag{3.2}$$

with weak heterogeneity and asymmetry $\sigma,\ \phi \ll 1$. Note that in the limit $\sigma \to 0$ and $\phi \to 0$, we obtain $w(x, y) = w_0(x - y)$, a distance-dependent even function. However, in the fully general case ($\sigma > 0$ and/or $\phi > 0$), it is straightforward to see that the function $w(x, y)$ need not be distance-dependent or even symmetric. In particular, when $\sigma > 0$, discrete attractors form in the network Eq. (4.1) whereby bumps tend to drift away from their initial position to a finite number of linearly stable locations [82, 90, 168]. We consider this to be a major source of error in the network, since near-perfect integration of the velocity inputs could be achieved if $w(x, y) = w_0(x - y)$. For ease of analysis, the translationally symmetric function is typically taken to be a cosine $w_0(x) := \cos x$. We will allow w_u to be more general, by representing it as a series of N Fourier modes

$$w_u(x) := \sum_{n=1}^{N} \alpha_n \cos(nx) + \beta_n \sin(nx); \quad \langle \alpha_n \rangle = \langle \beta_n \rangle = 0; \quad \langle \alpha_n^2 \rangle = \langle \beta_n^2 \rangle = \sigma_n^2. \tag{3.3}$$

The coefficients α_n, β_n are random variables drawn from the normal distribution with mean zero and variance σ_n^2.

Velocity inputs are derived from a double ring model (Appendix A), which is represented by the shifting function $w_v(x - y) := -w_0'(x - y)$ as in the original head direction system model [168] and recent grid cell models [30]. In the absence

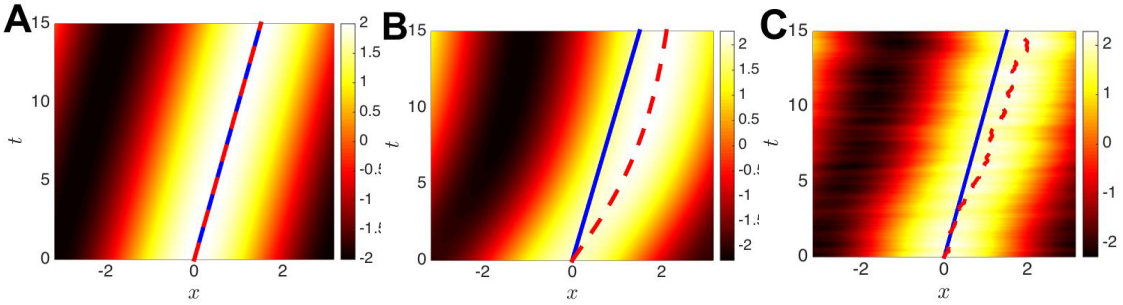

Figure 3.2: Velocity-integration with moving bump attractors in the neural field model Eq. (4.1) with a Heaviside firing rate function Eq. (1.3) with threshold $\theta = 0$ and a cosine base weight function $w_0(x) = \cos(x)$. (**A**) Bump of neural activity $u(x,t)$ perfectly integrates velocity inputs in the case of no heterogeneity ($\sigma = 0$) and no noise ($\varepsilon = 0$), showing the animal's true position (solid line) is perfectly tracked by the center of mass of the bump (dashed). (**B**) In a heterogeneous network ($\sigma = 0.1$ with $w_u = \sin(x)$), the bump initially moves too fast due to a discrete attractor of the input-free system at $x = \pi/2$, so the bump's center of mass is mismatched with the true position of the animal. (**C**) In the presence of spatiotemporal noise ($\varepsilon = 0.2$ with cosine correlations $C(x) = \cos(x)$), the bump wanders diffusively so the encoded position tends to slowly distance itself from the true position. Here the external velocity input is constant $\tilde{v}(t) = 0.1$.

of any heterogeneity or asymmetry, the sum $w(x,y) + \tilde{v}(t) \cdot w_v(x-y)$ would be translation symmetric but not even-symmetric, in general. This asymmetry produces a moving bump as the solution to Eq. (4.1) that will move at a speed given by $|\tilde{v}(t)|$ (Fig 3.2**A**). Incorporating heterogeneity, $\sigma > 0$, the system is no longer translation symmetric, and a moving bump will not move at the same speed as the velocity input $|\tilde{v}(t)|$ (Fig. 3.2**B**). Thus, assuming a sensory mechanism for correcting the place cell's encoded position when a cue is encountered, take the velocity input to be

$$\tilde{v}(t) := v(t) + v_c(t),$$

the sum of the animal's true velocity $v(t)$ and an external control signal $v_c(t)$. This is meant to account for the improved place representation observed when

animals can employ information about sensory landmarks [2, 12, 145]. As shown in the schematic in Fig. 3.1**A**, we assume there is a network that can access the place cell network's perceived position $\Delta(t)$ via a readout of the center of mass of neural activity [51]

$$\Delta(t) = \int_{-\pi}^{\pi} x f(u(x,t))\mathrm{d}x. \tag{3.4}$$

We note that for mass near the boundary, we take caution in calculation due to the periodic boundary conditions. For a symmetric bump, the center of mass can be calculated easily as the peak of the bump. The present positional error is then computed by comparing the perceived position $\Delta(t)$ to the animal's actual position given by a time integral of the velocity input

$$\Delta_T(t) = \int_0^t v(s)\mathrm{d}s,$$

so the error

$$r(t) = \Delta_T(t) - \Delta(t), \tag{3.5}$$

which will be positive (negative) if the estimated position is to the left (right) of the true position. Note, we extend the domain $x \in [-\pi, \pi]$ to compute Eq. (3.5) in cases where the closest distance between Δ_T and Δ is across the boundary cuts at $x = \pm\pi$. The error $r(t)$ is then translated either into a continuous velocity control signal

$$v_c(t) = \lambda r(t) = \lambda \cdot (\Delta_T(t) - \Delta(t)), \tag{3.6}$$

or a discrete control signal given by

$$\frac{\mathrm{d}v_c}{\mathrm{d}t} = -\frac{v_c(t)}{\tau} + \lambda \sum_{k=1}^{N_c} r(t_k)\delta(t - t_k), \tag{3.7}$$

where sensory cues occur at times t_k and λ and τ determine the strength and time decay of control. As we will show, in the case of continuous control Eq. (3.6), strengthening the sensory feedback λ always leads to a reduction of the error. This is not the case for discrete control Eq. (3.7), since the previous sensory cue at $t_k < t$ becomes less relevant as t increases toward t_{k+1}. One of the main goals of this study is to explore how the spacing between subsequent cues $t_{k+1} - t_k$ determines how strong λ the control signal should be.

The noise term, $dW(x,t)$, will be defined as in (1.5). As an example, consider $\mathcal{F}(x) = \cos(x) + \sin(x)$. Then, the spatial correlation C can be computed explicitly as

$$\int_{-\pi}^{\pi} \mathcal{F}(x-x')\mathcal{F}(y-x')dx' = \pi\cos(x-y) =: C(x-y).$$

As we demonstrate, the control introduced to account for the impact of synaptic spatial heterogeneity can also be utilized to decrease errors brought about by spatiotemporal noise (Fig. 3.2**C**).

We demonstrate the impact of discrete control Eq. (3.7) on the dynamics of neural fields that imperfectly integrate their velocity inputs, comparing to a perfectly integrating network for reference (Fig. 3.3**A**). Integrating Eq. (3.7), we find that the discrete perturbations to the velocity signal are given by a series of exponentially decaying impulses

$$v_c(t) = \lambda \sum_{k=1}^{N_c} r(t_k)\mathrm{e}^{-(t-t_k)/\tau} H(t-t_k). \tag{3.8}$$

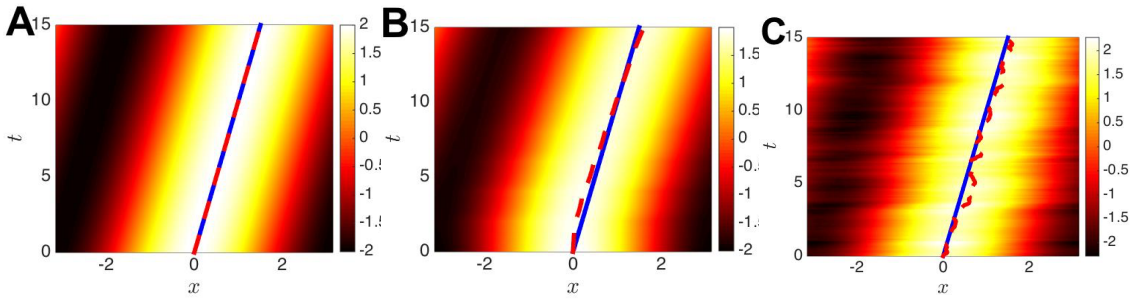

Figure 3.3: Discrete control reduces error in imperfect velocity-integrating networks. (**A**) Activity plot $u(x,t)$ shows perfect velocity-integrating network is unaffected by discrete control given by Eq. (3.7), since it accumulates no errors. (**B**) Spatially heterogeneous network with $\sigma = 0.1$ and $w_u(x) = \sin(x)$ is corrected by discrete control so that the represented position (dashed line) is much closer to the true position (solid line) than in the uncorrected case (compare with Fig. 3.2**B**). (**C**) Network perturbed by noise ($\varepsilon = 0.2$ and $C(x) = \cos(x)$) has its represented position corrected by discrete control (compare with Fig. 3.2**C**). Discrete control Eq. (3.8) is given at intervals $t_{k+1} - t_k = \Delta t = 2$ with strength $\lambda = 1$ and decay timescale $\tau = 1$. Other parameters and numerical simulations are as in Fig. 3.2.

Furthermore, in the limit of the timestep $t_{k+1} - t_k$ between subsequent cues tending to zero and $\tau \to 0$, Eq. (3.7) for discrete control approaches Eq. (3.6) for continuous control. Assuming for demonstration that cues are spaced in such a way that an animal utilizes one every 2 units of time ($t_{k+1} - t_k = 2$ for all $k = 1, ..., N_c - 1$), we demonstrate in a single realization that a network with spatially heterogeneous coupling can recover its ability to correctly integrate velocity (Fig. 3.3**B**). In a similar way, networks with additive noise can have their velocity integration corrected by the sensory feedback signal given by discrete control impulses, Eq. (3.8), as shown in Fig. 3.3**C**. In the next section, we will analyze the impact of heterogeneity and noise on the position of the bump in a low-dimensional approximation of the bump's center of mass $\Delta(t)$.

3.2 Analysis and low-dimensional reduction of bump solutions

To understand the impact the sensory feedback signal has on the statistics of bump position in Eq. (4.1), we derive a low-dimensional approximation of the model that projects the dynamics down to a single equation describing bump position $\Delta(t)$. Our analysis is adapted from recent studies of stochastic neural field equations, assuming the impact of perturbations to a translationally symmetric neural field can be separated into slow timescale changes of the position of bumps along with fast timescale changes to the profile of bumps [24, 25, 90]. Such analysis must begin by constructing the bump solutions of the unperturbed system. In our case we take the velocity inputs, heterogeneity, asymmetry, and noise all to be perturbations to a translationally symmetric system (taking $v = \sigma = \phi = \varepsilon = 0$ in Eq. (4.1)). While it is possible to develop exact analytical results in the case wherein we break the symmetry of this model, which we show, it is also helpful to collect the effects of all the possible perturbations to Eq. (4.1) into a single scalar equation. The resulting analysis then clearly demonstrates the interaction of such perturbations.

3.2.1 Stationary bump solutions to the translation symmetric network

We begin by assuming the homogeneous connectivity function $w_0(x)$ in Eq. (3.2) satisfies evenness ($w_0(x) = w_0(-x)$) and there is no heterogeneity ($\sigma = 0$) or asymmetry ($\phi = 0$) in $w(x, y)$. In this case, it is possible to show there is a stationary bump solution $u(x, t) = U(x)$ with $U(x) > \theta$ over an excited region $x \in [a_1, a_2]$ [4, 55] in the absence of velocity inputs ($\tilde{v} \equiv 0$) in Eq. (4.1). Furthermore, the weight function is translationally symmetric since

$$w_0((x+s)-(y+s)) = w_0(x-y+s-s) = w_0(x-y), \tag{3.9}$$

so there will be a continuum of bump locations associated with any single bump solution to Eq. (4.1). Stationary bumps satisfy the equation

$$U(x) = \int_{-\pi}^{\pi} w_0(x-y) f(U(y)) dy. \tag{3.10}$$

Note that $U(x+s)$ will also be a solution for any s, since

$$U(x+s) = \int_{-\pi}^{\pi} w_0(x-y) f(U(y+s)) dy,$$

and a change of variables $y + s \mapsto z$ yields

$$U(x+s) = \int_{-\pi}^{\pi} w_0(x+s-z) f(U(z)) dz,$$

and another change of variables $x + s \mapsto x'$ yields

$$U(x') = \int_{-\pi}^{\pi} w_0(x'-z) f(U(z)) dz,$$

which is precisely Eq. (3.10). Now, taking the high gain limit $\gamma \to \infty$, we employ the Heaviside firing rate function Eq. (1.3). Doing so allows us to generate an equation for the bump width $d = a_2 - a_1$ as in [4]. In this case, Eq. (3.10) becomes

$$U(x) = \int_{a_1}^{a_2} w_0(x-y)dy.$$

We then use the threshold crossing conditions $U(a_1) = U(a_2) = \theta$ and evenness of $w_0(x)$ to derive

$$\begin{aligned} U(a_1) &= \int_{a_1}^{a_2} w_0(a_1-y)dy = \int_0^{a_2-a_1} w_0(-z)dz = \int_0^d w_0(z)dz = \theta \\ U(a_2) &= \int_{a_1}^{a_2} w_0(a_2-y)dy = -\int_{a_2-a_1}^{0} w_0(z)dz = \int_0^d w_0(z)dz = \theta. \end{aligned}$$

Note that the evenness of $w_0(x)$ allows us to manipulate the above equations so they are the same equalities. If evenness did not hold, the above pair of equations would each be different and we would have an overdetermined system for the bump width d, meaning stationary bumps do not exist. Thus,

$$W(d) = \int_0^d w_0(x)dx = \theta \quad \Rightarrow \quad d = W^{-1}(\theta).$$

For example, in the case of a cosine weight $w_0(x) = \cos(x)$, we have

$$W(d) = \int_0^d \cos(x)dx = \sin(d) = \theta \quad \Rightarrow \quad d = \sin^{-1}\theta, \pi - \sin^{-1}\theta. \tag{3.11}$$

As mentioned, the threshold conditions specify the width d of the bump. Translation symmetry allows the position of the bump to be anywhere $x \in [-\pi, \pi]$, which allows this network to integrate and store velocity inputs as a position memory. As mentioned in Section 3.1, the position of the bump will be given by its center of

mass Eq. (3.4), which for unimodal and even symmetric bumps will also be given by the peak

$$\Delta = \text{argmax}_x U(x). \tag{3.12}$$

For example, in the case of cosine weight functions $w_0(x) = \cos(x)$, there is an even symmetric solution such that $a_1 = -a$ and $a_2 = a$, so

$$U(x) = \int_{-a}^{a} \cos(x-y)dy = 2\sin(a)\cos(x). \tag{3.13}$$

Thus, the location of the bump as computed by Eq. (3.12) is $\Delta = 0$. Similarly, if we compute the center of mass using Eq. (3.4), we find

$$\Delta = \int_{-\pi}^{\pi} xf(U(x))dx = \int_{-a}^{a} xdx = 0,$$

which is consistent.

3.2.2 Perfect velocity integration by traveling bumps

Now we explore the impact of velocity inputs ($v(t) \neq 0$) on the translationally symmetric network ($w(x,y) = w_0(x-y)$). For now, we assume constant velocity inputs, $v(t) \equiv v_0$. Assuming the bump subsequently moves at a constant speed c, we look for a traveling wave solution $u(x,t) = U(\xi)$ where $\xi = x - ct$. We will show that the traveling wave speed c is exactly equal to the velocity input amplitude v_0, under the assumption that $w_v(x) = -w_0'(x)$ in Eq. (4.1). Plugging these conditions into Eq. (4.1), we find

$$-cU'(\xi) + U(\xi) = \int_{-\pi}^{\pi} [w_0(\xi - y) + v_0 w_v(\xi - y)]\, f(U(y))dy.$$

Now plugging in our requirement that the velocity portion of the weight function $w_v(x) = -w_0'(x)$, we have

$$-cU'(\xi) + U(\xi) = -v_0 \int_{-\pi}^{\pi} w_0'(\xi - y) f(U(y)) dy + \int_{-\pi}^{\pi} w_0(\xi - y) f(U(y)) dy. \tag{3.14}$$

Under the assumption that the function $U(\xi)$ satisfies the equality Eq. (3.10), we can differentiate this equation to yield

$$U'(\xi) = \int_{-\pi}^{\pi} w_0'(\xi - y) f(U(y)) dy. \tag{3.15}$$

Canceling the Eq. (3.10) portion of Eq. (3.14), we find that

$$cU'(\xi) = v_0 \int_{-\pi}^{\pi} w_0'(\xi - y) f(U(y)) dy. \tag{3.16}$$

The equality Eq. (3.16) follows from Eq. (3.15) as long as we set $c \equiv v_0$. Another implication of our analysis is that the shape of the bump $U(\xi)$ will be the same no matter what c (equivalently v_0) is, suggesting there will be no relaxation time if the external drive v_0 were to be changed abruptly. In this way, we can expect the translation symmetric version of the network Eq. (4.1) to integrate inputs perfectly, as was originally proposed by [168].

3.2.3 Imperfect integration due to heterogeneity, asymmetry, and noise

Now that we have explored the dynamics of the perfect velocity-integrating network, we study the impact of introducing heterogeneities (σ), asymmetry (ϕ), and

noise (ε) into the network Eq. (4.1). Rather than deriving exact solutions as we did for the translationally symmetric system, we take a perturbative approach under the assumption that alterations to the symmetric system are weak. Following perturbation methods originally developed for the study of front propagation in reaction-diffusion systems [113, 126], we employ a separation of time scales to decompose these effects into a slowly evolving displacement $\Delta(t)$ of the bump from its uniformly translating position and perturbations to the bump profile $\Phi(x,t)$. This yields the following decomposition

$$u(x,t) = U(x - \Delta(t)) + \varepsilon\Phi(x - \Delta(t), t) + \mathcal{O}(\varepsilon^2), \tag{3.17}$$

where we assume $\sigma, \phi, \tilde{v}(t) \sim \mathcal{O}(\varepsilon)$. Plugging the ansatz Eq. (3.17) into Eq. (4.1) and expanding in powers of ε, we find that at $\mathcal{O}(1)$, the system has a stationary bump solution given by Eq. (3.10). At linear order $\mathcal{O}(\varepsilon)$, we find the following equation

$$\begin{aligned} \varepsilon d\Phi(x,t) =& \varepsilon\mathcal{L}\Phi(x,t)dt + U'(x)\mathrm{d}\Delta(t) + \sigma\int_{-\pi}^{\pi} w_u(y + \Delta(t))w_0(x-y)f(U(y))dydt \\ &- (\tilde{v}(t) + \phi)\int_{-\pi}^{\pi} w_0'(x-y)f(U(y))dydt + \varepsilon dW(x,t) \end{aligned} \tag{3.18}$$

where $\mathcal{L}$ is a linear functional given by

$$\mathcal{L}p(x) := -p(x) + \int_{-\pi}^{\pi} w_0(x-y)f'(U(y))p(y)dy$$

and its adjoint operator

$$\mathcal{L}^* q(x) = -q(x) + f'(U(x))\int_{-\pi}^{\pi} w_0(x-y)q(y)dy.$$

To ensure a solution to Eq. (3.18), we require that the inhomogeneous portion of the equation be orthogonal to the nullspace of the adjoint operator $\mathcal{L}^*$. Indeed, the nullspace of $\mathcal{L}^*$ is spanned by $\varphi(x) = f'(U(x))U'(x)$, where $U(x)$ is defined by Eq. (3.10), which we can verify using integration by parts

$$\begin{aligned}\mathcal{L}^*\varphi(x) &= -\varphi(x) + f'(U(x))\int_{-\pi}^{\pi} w_0(x-y)\varphi(y)dy \\ &= f'(U(x))\Big(-U'(x) + \int_{-\pi}^{\pi} w_0(x-y)f'(U(y))U'(y)dy\Big) \\ &= f'(U(x))\Big(-U'(x) + \int_{-\pi}^{\pi} \frac{d}{dy}\big(w_0(x-y)\big)f(U(y))dy\Big) \\ &= f'(U(x))\Big(-U'(x) + \frac{d}{dx}\Big(\int_{-\pi}^{\pi} w_0(x-y)f(U(y))dy\Big)\Big) = 0.\end{aligned} \tag{3.19}$$

The last line holds by differentiating the bump existence equation as in Eq. (3.15). Now, by taking inner products of the null vector φ with the $\mathcal{O}(\varepsilon)$ Eq. (3.18), we can derive an evolution equation for $\Delta(t)$, the position of the bump

$$\begin{aligned}-\langle\varphi(x), U'(x)\rangle d\Delta(t) =& \sigma\Big\langle\varphi(x), \int_{-\pi}^{\pi} w_u(y+\Delta(t))w_0(x-y)f(U(y))dy\Big\rangle dt \\ &- (\tilde{v}(t)+\phi)\langle\varphi(x), U'(x)\rangle dt + \varepsilon\langle\varphi(x), dW(x,t)\rangle,\end{aligned} \tag{3.20}$$

where we have applied the Eq. (3.15). We can simplify the Eq. (3.20) further by isolating $d\Delta(t)$ to yield the stochastic differential equation

$$d\Delta(t) = \left[F(\Delta(t)) + v(t) + v_c(t) + \phi\right]dt + d\mathcal{W}(t), \tag{3.21}$$

where the impact of synaptic spatial heterogeneities is described by the nonlinear function

$$F(\Delta) = -\sigma\frac{\int_{-\pi}^{\pi} f'(U(x))U'(x)\int_{-\pi}^{\pi} w_u(y+\Delta)w_0(x-y)f(U(y))dydx}{\int_{-\pi}^{\pi} f'(U(x))U'(x)^2dx}, \tag{3.22}$$

and the noise term has been projected to a temporal white noise process $\mathcal{W}(t)$ with mean zero ($\langle \mathcal{W}(t) \rangle = 0$) and variance $\langle \mathcal{W}(t)^2 \rangle = Dt$ with associated diffusion coefficient

$$D = \varepsilon^2 \frac{\int_{-\pi}^{\pi} \int_{-\pi}^{\pi} f'(U(x)) U'(x) f'(U(y)) U'(y) C(x-y) dy dx}{\left[\int_{-\pi}^{\pi} f'(U(x)) U'(x)^2 dx \right]^2}. \tag{3.23}$$

Setting $v_c(t) \equiv 0$ and $v(t) \equiv v_0$ (constant), the dynamics of the position variable $\Delta(t)$ can be equivalently described by a potential function

$$V(\Delta) = -\int \left[F(\Delta) + v_0 + \phi \right] d\Delta = -\int F(\Delta) d\Delta - (v_0 + \phi)\Delta, \tag{3.24}$$

so $\Delta(t)$ will descend the gradient of $V(\Delta)$ toward its local minima. Note that in the case $F(\Delta) \equiv -\phi$ and $\mathcal{W}(t) \equiv 0$, the control term will vanish $v_c(t) \equiv 0$ and the bump will perfectly integrate the velocity input, $\Delta(t) = \int_0^t v(s) ds$. We find that the low-dimensional approximation is in excellent agreement with simulations of the full system in this case of perfect integration (Fig. 3.4**A**).

Ignoring the control for the time being in Eq. (3.21), we can also identify how different network imperfections contribute to the resultant error in path integration. To do so, we simply compute the error function $r(t) = \Delta_T(t) - \Delta(t)$ as given in Eq. (3.5). First, note that in a network with asymmetry $\phi \neq 0$ and no heterogeneity $F(\Delta) \equiv 0$, the long term error accumulates linearly in time

$$r(t) = \Delta_T(t) - \Delta(t) = \int_0^t v(s) ds - \int_0^t \left[v(s) + \phi \right] ds = -\phi t,$$

so the animal's true position Δ_T will be behind (in front of) the estimated position Δ when $\phi > 0$ ($\phi < 0$). We will demonstrate the impact external control via sensory cues has upon this error in Section 3.3. Errors due to arbitrary heterogeneities

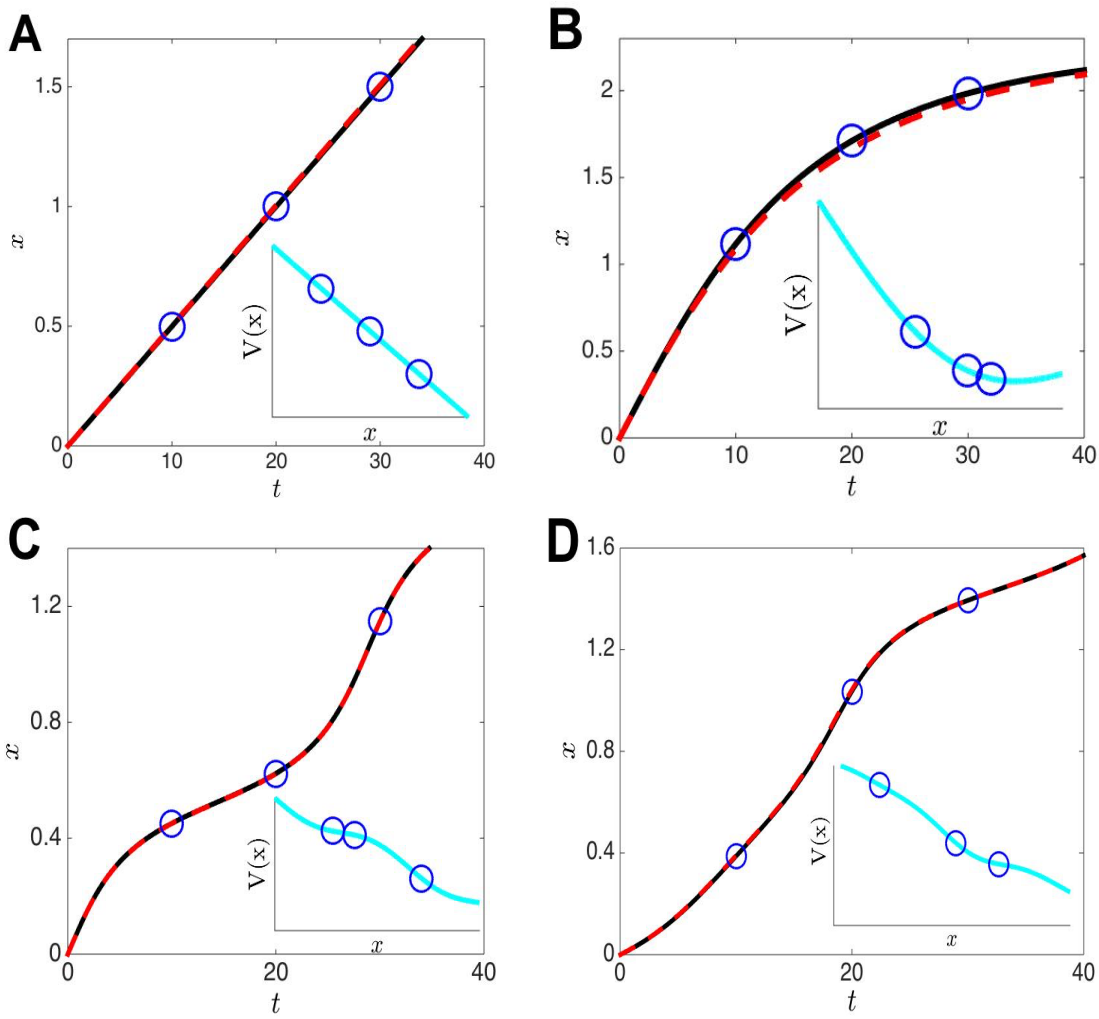

Figure 3.4: The low-dimensional Eq. (3.21) for the bump position $\Delta(t)$ provides an accurate approximation of the bump's movement in the full neural field model Eq. (4.1). (**A**) Perfect integration of the constant velocity input $v(t) = 0.05$ leads to a constantly drifting bump (solid line) whose position is well approximated by the projected variable $\Delta(t)$ (dashed line). Inset shows the tilted potential $V(\Delta)$ resulting from the constant velocity input. Circles provide corresponding locations between the two plots at $t = 10, 20, 30$. (**B**) Spatial heterogeneity $w_u(x) = \sin(x)$ with $\sigma = 0.1$ causes bumps to drift toward local attractors of the network. Inset shows potential with a local minimum to which the trajectory is attracted. (**C**) Spatial heterogeneity $w_u(x) = \sin(6x)$ with $\sigma = 0.2$ leads to a more rapid oscillation in the trajectory $\Delta(t)$. (**D**) Spatial heterogeneity $w_u(x) = \sin(4x) + \cos(8x)$ with $\sigma = 0.1$ leads to a less regular deviation in the trajectory $\Delta(t)$. Heaviside firing rate function Eq. (1.3) has threshold $\theta = 0$. Numerical simulations are run using the same parameters as in Fig. 3.2.

are more difficult to express explicitly. In general, we can express the solution to Eq. (3.21) implicitly in this case if we assume the velocity is constant $v(t) \equiv v_0$:

$$G(\Delta(t)) = \int_0^{\Delta} \frac{dy}{F(y) + v_0} = t. \tag{3.25}$$

If indeed the function $G(\Delta)$ is invertible, then we can express $\Delta(t) = G^{-1}(t)$, so

$$r(t) = \Delta_T(t) - \Delta(t) = v_0 t - G^{-1}(t). \tag{3.26}$$

We will demonstrate some cases where we can perform this calculation explicitly in Subsection 3.2.4. Note that the main impact of heterogeneities is to establish a finite number of discrete attractors, in the velocity input-free system, so that bumps drift toward these locations (Fig. 3.4**B**). Even in the velocity-driven network, spatial heterogeneities lead to a sinuous trajectory of the bump that is mismatched to a straight integration of velocity input (Fig. 3.4**C**,**D**). Lastly, note that the impact of noise can be quantified by averaging across realizations of the stochastic process

$$\Delta(t) = \int_0^t v(s)ds + \mathcal{W}(t) = \Delta_T(t) + \mathcal{W}(t).$$

While the mean position will be the same for the true and encoded positions ($\Delta_T(t) - \langle \Delta(t) \rangle = 0$), the variance will grow linearly in time

$$\langle r(t)^2 \rangle = \langle (\Delta_T(t) - \Delta(t))^2 \rangle = \langle \mathcal{W}(t)^2 \rangle = Dt,$$

where the diffusion coefficient D can be computed using Eq. (3.23). Previous work has characterized the impact of the bump profile and spatiotemporal noise correlation structure on the diffusion coefficient D, providing some explicit calculations [90]. In general, the main effects of noise perturbations on the bump will be experienced by the bump edges, where the activity variable $u(x,t)$ crosses the firing

rate threshold θ. We now provide some explicit calculations demonstrating the impact of spatial heterogeneity on the long term position of the bump.

3.2.4 Explicit results for spatially heterogeneous networks with a Heaviside firing rate

Several previous studies have characterized the impact of periodic microstructure on the propagation of waves in neural media [17, 44, 92]. Typically, periodic heterogeneities can slow down waves and even cause propagation failure. We extend these previous results here, showing that the low-dimensional Eq. (3.21) allows us to estimate the location of bifurcations separating detectable and undetectable constant velocity inputs $v(t) \equiv v_0$. Again, we are ignoring the impact of control at this point, studying its effects in more detail in Section 3.3. To allow for more general weight heterogeneities, we consider the decomposition given by Eq. (3.3). Thus, we can integrate each of the Fourier modes independently to derive the function $F(\Delta)$ given by Eq. (3.22). Furthermore, we assume a cosine for the homogeneous weight function $w_0(x) = \cos(x)$ and a Heaviside firing rate Eq. (1.3).

To begin, note that the bump solution is given by Eq. (3.13) and the half-width is $a = \frac{1}{2}\left[\pi - \sin^{-1}\theta\right]$ as given by Eq. (3.11). Therefore, the spatial derivative $U'(x) = -2\sin(a)\sin(x)$. Furthermore, the null vector defined by Eq. (3.19) is spanned by the difference of delta distributions $\delta(x+a) - \delta(x-a)$. This means that the frequency n cosine Fourier components of the heterogeneity, with scaling

α_n, contribute the function $F(\Delta)$ in the following way

$$\begin{aligned} F_{\alpha_n}(\Delta) =& \frac{\int_{-\pi}^{\pi} (\delta(x+a) - \delta(x-a)) \int_{-a}^{a} \cos(n(y+\Delta)) \cos(x-y) dy dx}{2 \sin a \int_{-\pi}^{\pi} (\delta(x+a) - \delta(x-a)) \sin x dx} \\ =& \frac{n \cos(na) - \cot(a) \sin(na)}{n^2 - 1} \sin(n\Delta). \end{aligned}$$

In a similar way, we can compute the coefficients arising from the sine Fourier components with scaling β_n as

$$\begin{aligned} F_{\beta_n}(\Delta) =& \frac{\int_{-\pi}^{\pi} (\delta(x+a) - \delta(x-a)) \int_{-a}^{a} \sin(n(y+\Delta)) \cos(x-y) dy dx}{2 \sin a \int_{-\pi}^{\pi} (\delta(x+a) - \delta(x-a)) \sin x dx} \\ =& \frac{\cot(a) \sin(na) - n \cos(na)}{n^2 - 1} \cos(n\Delta). \end{aligned}$$

Thus, we can write the resultant heterogeneity in general as

$$F(\Delta) = \sigma \sum_{n=1}^{N} \mathcal{C}_n \left[\alpha_n \sin(n\Delta) - \beta_n \cos(n\Delta) \right], \tag{3.27}$$

where

$$\mathcal{C}_n = \frac{n \cos(na) - \cot(a) \sin(na)}{n^2 - 1}, \tag{3.28}$$

and notice in the special case $n = 1$, we can take the limit $n \to 1$ to find

$$\mathcal{C}_1 = \frac{\sin(a) \cos(a) - a}{2 \sin(a)}. \tag{3.29}$$

We can explicitly compute the solution to Eq. (3.21) in some special cases of the heterogeneity $F(\Delta)$, defined by Eq. (3.27). In particular, we focus on a single cosine-shaped heterogeneity so that $\alpha_m = 1$, $\alpha_n = 0$ ($n \neq m$), and $\beta_n = 0$ ($\forall n$). Furthermore, we assume a constant input velocity $v(t) \equiv v_0$, so that the scalar Eq. (3.21) for $\Delta(t)$ is given by

$$\dot{\Delta}(t) = \kappa \sin(m\Delta) + v_0, \tag{3.30}$$

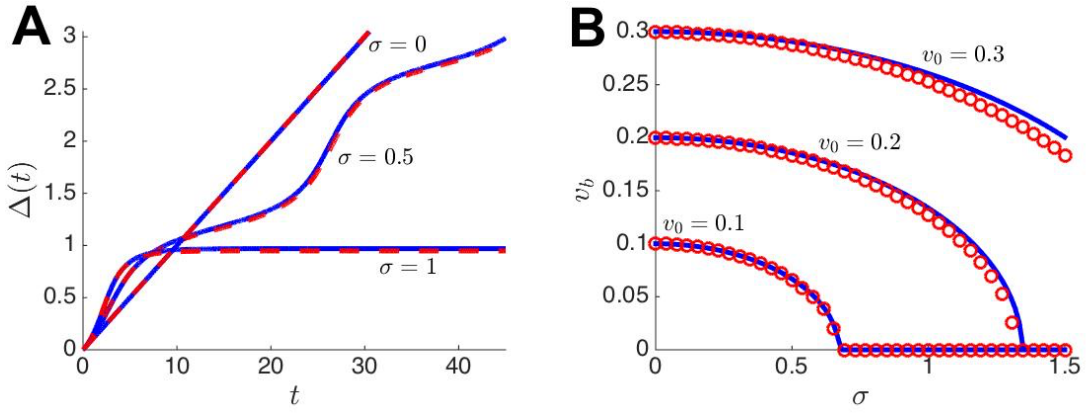

Figure 3.5: Spatial heterogeneity slows and even stops the propagation of velocity-driven bumps. (**A**) Bump position $\Delta(t)$ demonstrates the variant propagation velocity occurring when heterogeneity ($\sigma = 0.5$) is introduced as opposed to the homogeneous network ($\sigma = 0$). For strong enough heterogeneity ($\sigma = 1$), propagation fails. Theory (solid line) given by Eq. (3.31) is well matched to simulations (dashed line) of the full model Eq. (4.1). (**B**) Bump velocity v_b decreases as a function of heterogeneity strength σ until propagation failure occurs at $\sigma = (m^2 - 1)|v_0|/|\cot(a)\sin(ma) - m\cos(ma)|$. Firing rate function is Heaviside Eq. (1.3), heterogeneity is $w_u(x) = \cos(mx)$, with$\theta = 0.5$ and $m = 4$.

where $\kappa = \sigma\mathcal{C}_n$. Now, assuming $\Delta(0) = 0$, the Eq. (3.30) can be integrated to yield an explicit solution

$$\Delta(t) = \frac{2}{m}\tan^{-1}\left[\frac{\chi\tan\left(\tan^{-1}\left[\frac{\kappa}{\chi}\right] + \frac{mt}{2}\chi\right) - \kappa}{v_0}\right], \tag{3.31}$$

with $\chi = \sqrt{\kappa^2 - v_0^2}$. There is a partition in (κ, v_0) parameter space given by the equation $|\kappa| = |v_0|$. When $|\kappa| > |v_0|$, so the arguments $\kappa^2 - v_0^2$ of the square roots in Eq. (3.31) are positive, then there is a family of fixed points of the Eq. (3.30), so that the bump position $\Delta(t)$ will eventually become pinned to a single position. In this case, velocity inputs are not detectable by the network, since they do not result in the propagation of a bump. Consistent with this, the Eq. (3.31) has a defined limit at $t \to \infty$, $\Delta(t) \to \frac{2}{m}\tan^{-1}\left[\sqrt{\kappa^2 - v_0^2}/v_0 - \kappa/v_0\right]$. The general formulas for

all equilibria of Eq. (3.30) are given by

$$\bar{\Delta}_{k+} = \frac{2k\pi}{m} + \frac{1}{m}\sin^{-1}\frac{v_0}{\kappa}, \qquad k = 0, ..., m-1, \tag{3.32}$$

$$\bar{\Delta}_{k-} = \frac{(2k+1)\pi}{m} - \frac{1}{m}\sin^{-1}\frac{v_0}{\kappa}, \qquad k = 0, ..., m-1. \tag{3.33}$$

On the other hand, when $|\kappa| < |v_0|$, the heterogeneity $F(\Delta)$ will not lead to pinning of bumps, so bumps will propagate indefinitely in response to velocity inputs. However, the heterogeneity will ultimately reduce the speed of propagation of bumps, as found in previous studies of periodically heterogeneous neural fields [17, 44, 92]. We can determine the average reduction in the bump's speed by calculating the time T at which $\Delta(t)$ crosses $\Delta = 2\pi/m$, completing one period of the heterogeneity $\sin(m\Delta)$:

$$T = \frac{2\pi}{m\sqrt{v_0^2 - \kappa^2}}, \tag{3.34}$$

which means that the average speed of the bump v_b is given

$$v_b = \frac{2\pi/m}{T} = \sqrt{v_0^2 - \kappa^2}, \tag{3.35}$$

similar to the speed scaling formulas found in [17, 44]. This allows us to directly compute the curve in parameter space at which wave propagation failure occurs, $|v_0| = |\kappa|$ as stated above. Note that the bump speed Eq. (3.35) depends on the frequency and amplitude of the heterogeneity through the term

$$\kappa = \sigma\frac{\cot(a)\sin(ma) - m\cos(ma)}{m^2 - 1}. \tag{3.36}$$

Thus, we can approximate the average, temporally-evolving error in path integration for this network as

$$r(t) = \Delta_T(t) - \Delta(t) \approx \left(v_0 - \sqrt{v_0^2 - \kappa^2}\right)t. \tag{3.37}$$

A more precise estimate is obtained by using the formula for $\Delta(t)$ given by Eq. (3.31). We demonstrate the accuracy of this full approximation in Fig. 3.4**C**,**D**. The bump position approximation Eq. (3.31) and average speed approximation computed from Eq. (3.35) are compared with the full neural field model Eq. (4.1) in Fig. 3.5. We find the low-dimensional approximation Eq. (3.30) is in excellent agreement with simulations. In particular, the points in parameter space at which propagation failure occur are well matched, and the sinuous trajectory of the bump is well tracked by our low-dimensional theory. This suggests we can gain many insights concerning the full model by analyzing this simpler Eq. (3.21).

As noted above, the existence of spatial heterogeneities in networks can lead to pinning or a reduction in the speed of propagating bumps, which should be accurately tracking velocity-input. However, several previous experiments have suggested that sensory feedback is incorporated into the neural representation of spatial navigation [12, 77, 145, 169]. As discussed in Section 3.1, we propose a simple external control mechanism that incorporates a comparison of an animal's current estimate of position with an external sensory cue (Fig. 3.1**A**). In Section 3.3, we will demonstrate the improvement in position encoding afforded by sensory feedback control. Furthermore, we will show that there is an optimal weighting and timescale of control feedback when sensory cues appear discretely in space or time.

3.3 Incorporating sensory cues with online control

Recent experimental studies have shown that the presence of sensory landmarks reduces the size of mammalian place fields as compared to the case of no landmarks [2, 12, 169]. Interestingly, such a reduction in place field size can occur quite quickly, in response to the temporary presence of sensory information, as show in echolocating bats [145]. Note here, we are referring to sensory information beyond the animal's proprioceptive experience of its own motion. Specifically, we are referring to objects placed along the track of navigation that may provide visual, auditory, or olfactory feedback (Fig. 3.1**B**). This suggests an online interaction between the sensory system and the path integration system that passes some positional information acquired by sensory cues [144]. We suggest that such mechanisms could counteract errors in position encoding that arise due to synaptic heterogeneity [26, 75, 82] or noise [31, 40, 99]. However, when cues occur discretely in space, tuning the strength of feedback introduces a tradeoff between the immediate benefits of recent cues and the deleterious influence of older irrelevant cues. We explore this in the low-dimensional model Eq. (3.21) derived in Section 3.2.

3.3.1 Error due to network asymmetry and heterogeneity

We first examine the case of instantaneous cues and updates, modeled as a continuous update to the position variable $\Delta(t)$, as described by Eq. (3.6). This would be

the case in which landmark cues are continuously apparent to an animal, allowing the sensory system to send a constant stream of information to the position-encoding network. For the time being, we also ignore the impact of noise, exploring its effect in Subsection 3.3.2. Under these assumptions, the low-dimensional equation for bump position is

$$\dot{\Delta}(t) = F(\Delta(t)) + \phi + v(t) + \lambda(\Delta_T(t) - \Delta(t)). \tag{3.38}$$

As a simple example of the impact of the control term in Eq. (3.38), we examine the case of no heterogeneity $F(\Delta) \equiv 0$ and non-zero asymmetry $\phi > 0$. In this case, we can analytically calculate the long term trajectory of the error $r(t) = \Delta_T(t) - \Delta(t)$. To do so, we can write down the first order differential equation for the error [137]

$$\begin{aligned} \dot{r}(t) + \lambda r(t) &= \dot{\Delta}_T(t) - \dot{\Delta}(t) + \lambda(\Delta_T(t) - \Delta(t)) \\ &= v(t) - \phi - v(t) - \lambda(\Delta_T(t) - \Delta(t)) + \lambda(\Delta_T(t) - \Delta(t)) \\ &= -\phi. \end{aligned} \tag{3.39}$$

It is straightforward to calculate the solution to the linear differential Eq. (3.39) in the case $r(0) = 0$, finding $r(t) = -\phi(1 - \mathrm{e}^{-\lambda t})/\lambda$ so that $\lim_{t\to\infty} r(t) = -\phi/\lambda$. Thus, perfect convergence of the trajectory $\Delta(t)$ to $\Delta_T(t)$ can only be obtained in the limit of infinitely strong control $\lambda \to \infty$. It is also important to note that as long as the control strength is positive $\lambda > 0$, the error $r(t)$ will be bounded in the long time limit $t \to \infty$.

We can extend our analysis of the Eq. (3.38) to the case of arbitrary heterogeneities using regular perturbation theory. Writing the linear expansion of $\Delta(t) =$

$\Delta_0(t) + \Delta_1(t)/\lambda$ under the assumption $\lambda \gg 1$, we find that the zeroth order equation for $\Delta_0(t)$ is simply given by $\Delta_0(t) = \Delta_T(t)$. Extending to the first order equation in $1/\lambda$, we find

$$\dot{\Delta}_T(t) = F(\Delta_T(t)) + \phi + v(t) - \Delta_1(t).$$

Applying the equation $\dot{\Delta}_T(t) = v(t)$, we thus find that $\Delta_1(t) = F(\Delta_T(t)) + \phi$, which means that the long term error can be approximated by

$$r(t) = F\left(\int_0^t v(s)ds\right) + \phi + \mathcal{O}(1/\lambda^2)$$

to first order in $1/\lambda$. Thus, as long as $F(\Delta)$ is a bounded function, then the error will remain bounded, reaching a maximum amplitude of $\max_x |F(x) + \phi|$ [137].

Thus far, we have considered the case of a continuous flow of sensory information providing an accurate estimate of an animal's position in space. However, in more realistic scenarios, animals receive external sensory information discretely in time via local landmarks [12, 144] or echolocation [145]. Sensory cues that provide a landmark for an animal's present position may be captured periodically in time or more randomly; we account for both forms of sensory cue acquisition. As discussed in our formulation of the model in Section 3.1, we assume the influence of sensory cues weakens as time elapses from the time at which they were received. This is consistent with recent observations concerning the evolution of place fields in bats as a function of the time since the last echo signal [145]. Thus

we consider the following model combing path integration with sensory cues acquired at times t_k:

$$\dot{\Delta}(t) = F(\Delta(t)) + \phi + v(t) + v_c(t), \tag{3.40}$$

$$\dot{v_c}(t) = -v_c(t)/\tau + \lambda \sum_{k=1}^{N_c} r(t_k)\delta(t - t_k), \tag{3.41}$$

$$r(t_k) = \Delta_T(t_k) - \Delta(t_k).$$

Analogous to the continuous control case, the error term r_k computes the instantaneous difference between the true position $\Delta_T(t)$ and the encoded position $\Delta(t)$ at time t_k. This is then incorporated into the discretely incremented control term $v_c(t)$ with strength λ, and the temporal decay of cue influence is determined by the timescale τ. We will demonstrate that for any given τ, there is an optimal strength of feedback that trades off the error reduction of recent cues (t_k) with the error increase potentially arising for older cues ($t_1, ..., t_{k-1}$). Assuming $v_c(0) = 0$ and treating the pointwise values of $r(t)$ as constant, we can integrate Eq. (3.41) to yield the piecewise smooth function

$$v_c(t) = \lambda \sum_{k=1}^{N_c} r(t_k)e^{-(t-t_k)/\tau}H(t - t_k),$$

as we did in Section 3.1 for the full neural field model in Eq. (3.8). Thus, adjustments in velocity are discretely incremented and then decay over time. Also, note in the limit $\tau \to 0$ and $t_{k+1} - t_k \to 0$, we obtain the continuous control function $v_c(t) = \lambda r(t)$. This can be seen by performing this limit on Eq. (3.41) and then integrating.

To demonstrate the impact of discrete control in more detail, we begin by studying the case of a network subject only to asymmetry ($F(\Delta) \equiv 0$ and $\phi > 0$).

Furthermore, we focus on the case of constant velocity input $v(t) \equiv v_0$, so we can write the discretely controlled position Eq. (3.40) as

$$\dot{\Delta}(t) = \phi + v_0 + \lambda \sum_{k=1}^{N_c} \left[v_0 t_k - \Delta(t_k)\right] \mathrm{e}^{-(t-t_k)/\tau} H(t - t_k). \tag{3.42}$$

We can solve the piecewise smooth differential Eq. (3.42) recursively, integrating with a new initial condition $\Delta(t_k)$ at each cue time t_k. In the initial time domain $[0, t_1)$, $\Delta(0) = 0$ and $\dot{\Delta}(t) = v_0 + \phi$, so $\Delta(t) = (v_0 + \phi)t$ and $\Delta(t_1) = (v_0 + \phi)t_1$. On the subsequent time domain $[t_1, t_2)$, we have

$$\dot{\Delta}(t) = v_0 + \phi + r(t_1)\mathrm{e}^{-(t-t_1)/\tau},$$

so

$$\Delta(t) = (v_0 + \phi)t + \lambda\tau r(t_1) \left[1 - \mathrm{e}^{-(t-t_1)/\tau}\right].$$

In a similar way, we can solve for $\Delta(t)$ on $[t_2, t_3)$ to find

$$\Delta(t) = (v_0 + \phi)t + \lambda\tau \sum_{k=1}^{2} r(t_k) \left[1 - \mathrm{e}^{-(t-t_k)/\tau}\right],$$

and in general, we can express

$$\Delta(t) = (v_0 + \phi)t + \lambda\tau \sum_{k=1}^{N_c} r(t_k) \left[1 - \mathrm{e}^{-(t-t_k)/\tau}\right] H(t - t_k).$$

Thus, we can express the error as a function of time

$$r(t) = -\phi t - \lambda\tau \sum_{k=1}^{N_c} r(t_k) \left[1 - \mathrm{e}^{-(t-t_k)/\tau}\right] H(t - t_k). \tag{3.43}$$

Expressing $r_k := r(t_k)$ and focusing on the error at the cue timepoints t_k, we can write Eq. (3.43) as

$$r_l = -\phi t - \lambda\tau \sum_{k=1}^{l-1} r_k \left[1 - \mathrm{e}^{-(t_l - t_k)/\tau}\right].$$

Furthermore, in the case of periodically spaced cues, we can write $t_{k+1} - t_k = (\Delta t)$, $\forall k$, so that

$$r_l = -\phi \cdot l \cdot \Delta t - \lambda\tau \sum_{k=1}^{l-1} r_k \left[1 - \mathrm{e}^{-(l-k)\Delta t/\tau}\right]. \tag{3.44}$$

Assuming that λ is not too large, the discrete Eq. (3.44) will have a fixed point in the long time limit $r_l \to r^*$, which we can compute by taking the difference between r_{l+1} and r_l and approximating $r_k \approx r^*$:

$$r_l = r^* = -\phi \cdot l \cdot \Delta t - \lambda\tau r^* \sum_{k=1}^{l-1} \left[1 - \mathrm{e}^{-(l-k)\Delta t/\tau}\right],$$

$$r_{l+1} = r^* = -\phi \cdot (l+1) \cdot \Delta t - \lambda\tau r^* \sum_{k=1}^{l} \left[1 - \mathrm{e}^{-(l+1-k)\Delta t/\tau}\right],$$

and we can make the approximation $\mathrm{e}^{-l\Delta t/\tau} \to 0$, so that $r_l - r_{l+1}$ yields

$$0 = \phi \cdot \Delta t + \lambda\tau r^* \quad \Rightarrow \quad r^* = -\phi \cdot \Delta t/(\lambda\tau). \tag{3.45}$$

We demonstrate the accuracy of the formula in Fig. 3.6**A**,**B**, showing that the error remains bounded due to the periodic perturbations of the discrete control term. Of course, the fixed point value given by Eq. (3.45) is contingent on its existence and stability. In cases where either condition is violated, the error r_l will diverge in the long time limit (Fig. 3.6**C**). Essentially, negative feedback overcorrects for the previously observed errors at each cue time, leading to unstable oscillations in the error. Analytically identifying the cases in which r_l diverges would require a more thorough study of the discrete Eq. (3.44). Numerical simulations suggest there is a boundary value of λ above which these unstable oscillations occur. Thus, the maximal value λ for which the fixed point r^* exists and is stable would correspond to the optimal control strength, all other parameters being fixed.

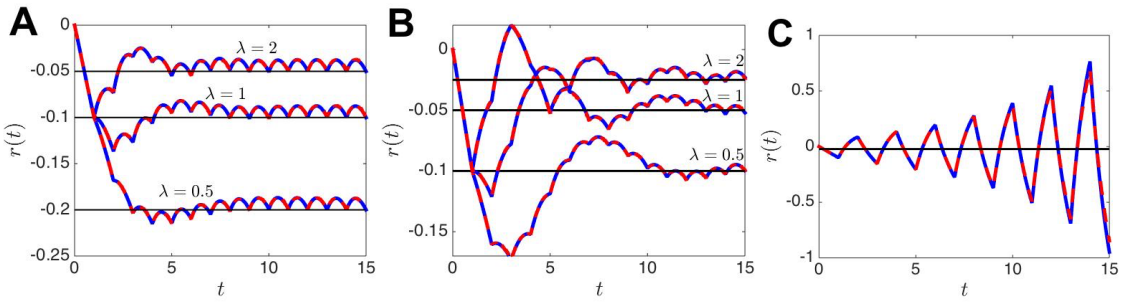

Figure 3.6: Path integration error in a network with asymmetry $\phi = 0.1$, discretely controlled according to Eq. (3.41). (**A**) Error resulting from asymmetry plus discrete control with time decay $\tau = 1$ quickly reaches the fixed point r^* (thin lines) given by Eq. (3.45). Notice as the strength of control λ is increased, the amplitude $|r(t)|$ of long term error decreases. Low-dimensional approximations (solid lines) given by Eq. (3.42) are in excellent agreement with simulations (dashed lines) of the full model Eq. (4.1). (**B**) Increasing the control decay timescale $\tau = 2$ leads to longer lasting oscillations in the error. (**C**) Making the control too strong, $\lambda = 4.5$, leads to instability in the error. Negative feedback produces oscillations that grow in amplitude. Time spacing between cues is $\Delta t = 1$. Other parameters $\theta = 0.5$, $v_0 = 0.1$. Numerical simulations utilize the same parameters as in Fig. 3.2.

We now study the case of heterogeneities and explore the impact of sensory cues on the long term error. Note, in the case of no asymmetry and constant velocity input $v(t) = v_0$, the low-dimensional equation for bump position takes the form

$$\dot{\Delta}(t) = F(\Delta(t)) + v_0 + \lambda \sum_{k=1}^{N_c} \left[v_0 t_k - \Delta(t_k)\right] \mathrm{e}^{-(t-t_k)/\tau} H(t - t_k). \tag{3.46}$$

While we cannot solve Eq. (3.46) explicitly for general heterogeneities $F(\Delta)$, we can numerically analyze the impact of both the control strength λ and the control decay timescale τ on the long term error $r(t) = \Delta_T(t) - \Delta(t)$. Specifically, we associate error with a scalar quantity by computing the log of the L^2-norm

$$R := \ln ||\Delta_T(t) - \Delta(t)||_2 = \ln \left[\sqrt{\int_0^{t_f} |\Delta_T(t) - \Delta(t)|^2 dt} \right], \tag{3.47}$$

where t_f is time at which the path ends. We compare the effects of varying the spacings $t_{k+1} - t_k$ between subsequent cues, testing both time-periodic cues ($t_{k+1} - t_k = \Delta t$, $\forall k$) and exponentially distributed spacings ($p(\Delta t) = \mu e^{-\mu \Delta t}$). Furthermore, we randomize the heterogeneity according to the formula Eq. (3.3) with variance $\sigma_n^2 = 1$ with four total modes ($N = 2$). To average error across many realizations, we simulate the controlled version Eq. (3.46) for many different randomly generated heterogeneities, compute an L^2-norm of error R_j for the jth realization and averaged $\langle R \rangle = \frac{1}{N_r} \sum_{j=1}^{N_r} R_j$ for N_r realizations.

We are mainly interested in the (λ, τ) values that minimize the average log error $\langle R \rangle$. Our findings are summarized in Fig. 3.7. First, we note that there is always a curve through (λ, τ) space determining the values of the control term that minimize the average error $\langle R \rangle$. In all plots, the associated τ value decreases with λ and vice versa. In general, we find this relationship to be roughly inversely proportional $\lambda \propto 1/\tau$. This means that stronger control should decay more quickly, and equivalently weaker control can last longer. Furthermore, by comparing plots for periodic cues with $\Delta t = 4$ (Fig. 3.7**A**) versus $\Delta t = 2$ (Fig. 3.7**B**), we find longer decay timescales associated with each λ value in the case $\Delta t = 2$. Such a trend may arise due to the fact that more frequent updates in sensory information via cues prevents overcorrection that could occur in the case of less frequent cues. A similar trend arises in the case of exponentially distributed time spacings between cues ($\mu = 0.5$ in Fig. 3.7**C** versus $\mu = 1$ in Fig. 3.7**D**). When cues are more frequent, the optimal timescale of decay τ is slightly larger for each value of λ.

In addition, we have studied the average error as a function of time for both

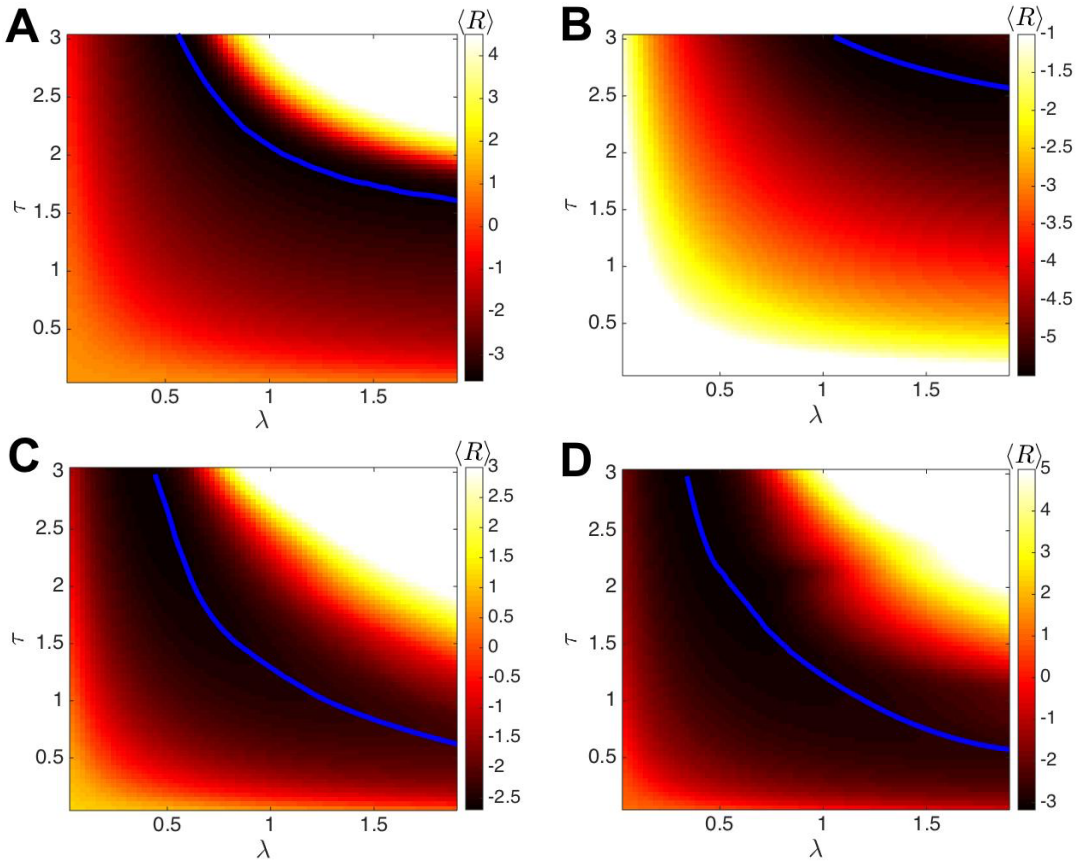

Figure 3.7: Average log error $\langle R \rangle$ computed across realizations of Eq. (3.47) for the discretely controlled low-dimensional approximation Eq. (3.46) with spatial heterogeneity resulting from Eq. (3.3) with $N = 2$ and coefficient variance $\sigma_n^2 = 1$. (**A**) For periodically appearing control cues with $\Delta t = 4$, we find there is an intermediate curve (solid) of (λ, τ) values that minimizes $\langle R \rangle$. In particular, as the control decay timescale τ is increased, the optimal value of λ decreases. (**B**) The same trend is consistent for periodic cues with spacing $\Delta t = 2$, but the curve of optimal (λ, τ) values shifts so there are higher values of τ associated with each value of λ as compared with **A**. (**C**,**D**) When spacings between cue times are exponentially distributed $p(\Delta t) = \mu e^{-\mu \Delta t}$ with $\mu = 0.5$ in **C** and $\mu = 1$ in **D**, we find the optimal curve shifts to shorter values of τ for more frequent cues. Other parameters $v_0 = 0.15$, $\theta = 0$, $\sigma = 0.1$, and simulation time $t_f = 40$. Numerical simulations are performed using Euler's method with a timestep of 0.05, and each grid point used 1000 realizations.

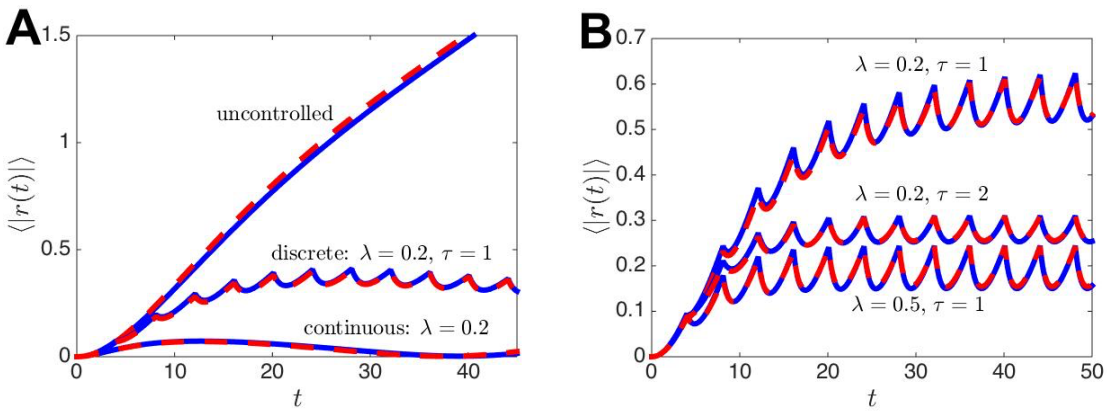

Figure 3.8: Average error $\langle |r(t)| \rangle$ as a function of time in a heterogeneous network ($w_u(x) = \alpha_1 \cos(x)$) with control. Velocity-input is constant $v(t) = v_0 = 0.05$. (**A**) Numerical simulations (dashed lines) of the neural field Eq. (4.1) are well matched by the low-dimensional approximation (solid lines) given by Eq. (3.46). As demonstrated, continuous control provides the best reduction in error, but discrete control with $\Delta t = 4$ still provides an appreciable reduction. (**B**) Plot demonstrates the impact of varying the control strength λ and the control decay timescale τ. Other parameters are $\theta = 0.2$ and $\sigma = 0.1$.

continuously and discretely controlled networks with heterogeneities. Note that we randomize the heterogeneity $w_u(x) = \alpha_1 \cos(x)$ so that α_1 is normally distributed with variance unity. To compute the average error, we take the mean of the absolute value $\langle |r(t)| \rangle$ as shown in Fig. 3.8. In the case of strong continuous control, it is possible to substantially decrease the impact of heterogeneities as compared with the uncontrolled case (Fig. 3.8**A**). Discrete control maintains an intermediate level of error, since there is not a constant stream of information provided to reduce error. Varying the strength λ and timescale τ of control alters the long term variance in the error (Fig. 3.8**B**). As suggested by Fig. 3.7, strong and fast decaying control tends to lead to substantial reductions in error.

3.3.2 Error due to dynamic fluctuations

We now examine the impact of sensory feedback on networks subject to temporal noise fluctuations. Dynamic variability in networks can arise from ion channel fluctuations [37], synaptic variability [123], or finite size effects [18]. As demonstrated in our analysis in Section 3.2, we can reduce the equation for the position of a noise- and velocity-driven bump to a single stochastic differential Eq. (3.21). Focusing specifically on the impact of noise, taking constant speed $v(t) \equiv v_0$, and ignoring heterogeneities, we find that the controlled equation for the bump position takes the form

$$d\Delta(t) = [v_0 + v_c(t)]\, dt + d\mathcal{W}(t). \tag{3.48}$$

We begin by examining the case of continuous sensory feedback, so that Eq. (3.48) becomes

$$d\Delta(t) = [v_0 + \lambda v_0 t - \lambda\Delta(t)]\, dt + d\mathcal{W}(t). \tag{3.49}$$

Note that Eq. (3.49) is a non-autonomous Ornstein-Uhlenbeck process, and we can use integrating factors to identify an explicit solution. Utilizing the change of variables $h(\Delta, t) = \Delta e^{\lambda t}$ and differentiating with respect to t, we find

$$\begin{aligned} dh(\Delta, t) &= d\Delta e^{\lambda t} + \lambda\Delta e^{\lambda t} = e^{\lambda t}\left[v_0 + \lambda v_0 t - \lambda\Delta + \lambda\Delta\right] dt + e^{\lambda t} d\mathcal{W} \\ &= e^{\lambda t}\left[v_0 + \lambda v_0 t\right] dt + e^{\lambda t} d\mathcal{W} = d\left(v_0 t e^{\lambda t}\right) + e^{\lambda t} d\mathcal{W}. \end{aligned} \tag{3.50}$$

Assuming $\Delta(0) = 0$, we can integrate Eq. (3.50) and multiply through by $e^{-\lambda t}$ to yield the solution

$$\Delta(t) = v_0 t + e^{-\lambda t} \int_0^t e^{\lambda s} d\mathcal{W}(s),$$

whose mean is $\langle \Delta(t) \rangle = v_0 t$ and variance is given

$$\langle \Delta(t)^2 \rangle - \langle \Delta(t) \rangle^2 = \frac{\sqrt{D}}{2\lambda} \left[1 - \mathrm{e}^{-2\lambda t} \right],$$

where the diffusion coefficient D can be calculated from the neural field model parameters as in Eq. (3.23). The long term variance is thus given by $\lim_{t\to\infty} \langle \Delta(t)^2 \rangle - \langle \Delta(t) \rangle^2 = \frac{\sqrt{D}}{2\lambda}$. Note that in the limit $\lambda \to \infty$, the variance goes to zero $\langle \Delta(t)^2 \rangle - \langle \Delta(t) \rangle^2 \to 0$, suggesting that strengthening continuous control will always reduce the average error further. Continuous control substantially reduces the long term variance in the bump position $\Delta(t)$ as well as the error

$$r(t) = \Delta_T(t) - \Delta(t) = -\mathrm{e}^{-\lambda t} \int_0^t \mathrm{e}^{\lambda s} d\mathcal{W}(s).$$

Note that $\langle r(t) \rangle = 0$ and $\langle r(t)^2 \rangle = \frac{\sqrt{D}}{2\lambda} \left[1 - \mathrm{e}^{-2\lambda t} \right]$. We compare the continuously controlled system to the control-free system in Fig. 3.9**A**, revealing the long term saturation in the position variance.

We also study the effect of discrete control on the variance in position, using the low-dimensional approximation of bump position

$$\begin{aligned} d\Delta(t) &= \left[v(t) + v_c(t) \right] dt + d\mathcal{W}(t), \\ \dot{v_c}(t) &= -\frac{v_c}{\tau} + \lambda \sum_{k=1}^{N_c} r(t_k) \delta(t - t_k). \end{aligned} \tag{3.51}$$

Again, this is under the assumption that cues are spaced discretely in time or space, and they provide sensory input for a brief period of time. As in Subsection 3.3.1, we can solve Eq. (3.51) iteratively. To begin, note that when $t \in [0, t_1)$, $\Delta(t)$ has yet to be affected by the feedback control term in Eq. (3.51), so $\Delta(t) = v_0 t +$

$\mathcal{W}(t)$. Subsequently, we can integrate Eq. (3.51) to find the stochastic formula for $\Delta(t)$ after the first cue at t_1:

$$\Delta(t) = v_0 t + \lambda\tau(v_0 t_1 - \Delta(t_1))\left[1 - \mathrm{e}^{-(t-t_1)/\tau}\right] + \mathcal{W}(t), \quad t \in [t_1, t_2).$$

Each realization will typically produce a different value for $\Delta(t_1) = v_0 t_1 + \mathcal{W}(t_1)$. Note that $\langle\Delta(t)\rangle = v_0 t$, so the impact of noise and control can be observed by calculating the variance [67]

$$\langle\Delta(t)^2\rangle - \langle\Delta(t)\rangle^2 = Dt + \lambda\tau D t_1\left(1 - \mathrm{e}^{-(t-t_1)/\tau}\right)\left(\lambda\tau\left(1 - \mathrm{e}^{-(t-t_1)/\tau}\right) - 2\right). \tag{3.52}$$

One insight to be gained from the formula Eq. (3.52) is that infinitely strong and fast decaying control, even when it is discrete, will minimize the variance in the position. Specifically, if we take $\lambda = \lambda_0/\tau$, then we can write

$$\langle\Delta(t)^2\rangle - \langle\Delta(t)\rangle^2 = Dt + \lambda_0 D t_1\left(1 - \mathrm{e}^{-\lambda(t-t_1)/\lambda_0}\right)\left(\lambda_0\left(1 - \mathrm{e}^{-\lambda(t-t_1)/\lambda_0}\right) - 2\right).$$

Taking the limit as $\lambda \to \infty$, we find that

$$\lim_{\lambda\to\infty}\left[\langle\Delta(t)^2\rangle - \langle\Delta(t)\rangle^2\right] = Dt + \lambda_0 D t_1(\lambda_0 - 2),$$

which is minimized when the scaling term $\lambda_0 = 1$, yielding $\langle\Delta(t)^2\rangle - \langle\Delta(t)\rangle^2 = D(t - t_1)$.

We can solve Eq. (3.51) explicitly for an arbitrary number of cue times, yielding

$$\Delta(t) = v_0 t + \lambda\tau\sum_{k=1}^{N_c} r(t_k)\left[1 - \mathrm{e}^{-(t-t_k)/\tau}\right] H(t - t_k) + \mathcal{W}(t). \tag{3.53}$$

While it is clear that the mean $\langle\Delta(t)\rangle = v_0 t$, it is more complicated to compute the variance $\langle\Delta(t)^2\rangle - \langle\Delta(t)\rangle^2$ in general. This is chiefly due to the fact that $r(t_k)$

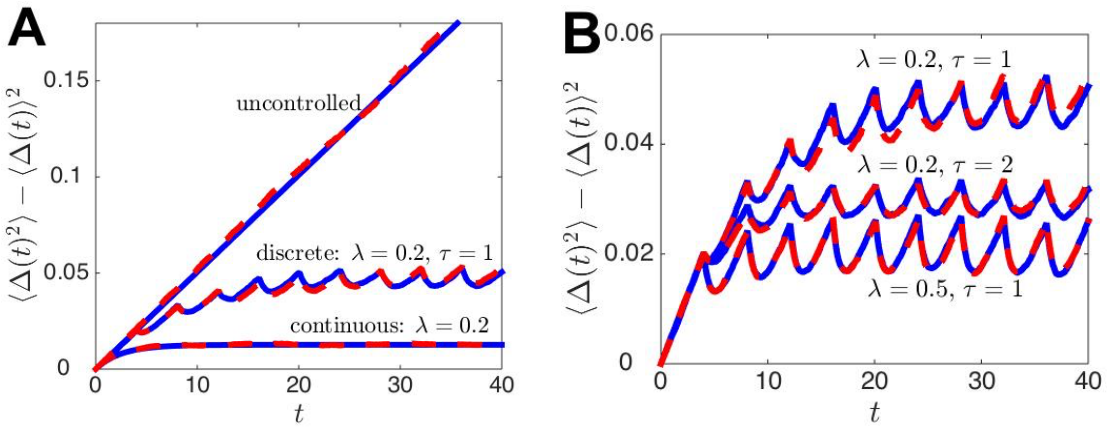

Figure 3.9: Variance $\langle \Delta(t)^2 \rangle - \langle \Delta(t) \rangle^2$ computed for the noise-driven network with control. Velocity-input is constant $v(t) = v_0 = 0$. (**A**) Numerical simulations (dashed lines) of the neural field model Eq. (4.1) are well matched to low-dimensional approximation (solid lines) given by Eq. (3.48). Continuous control substantially reduces the variance, but discrete control with $\Delta t = 4$ also provide a variance reduction. Notably, the variance saturates in the case of discrete control as well. (**B**) Similar to the case of quenched variability through heterogeneity in Fig. 3.8, varying the strength and timescale of control alters the long term variance. Other parameters are $\theta = 0.2$ and $\varepsilon = 0.1$.

will depend on $(r(t_1), ..., r(t_{k-1}))$, and this long-lasting history-dependence will accumulate indefinitely. To gain some analytical understanding, we make the assumption of brief control impulses, so that $\tau \ll 1$ and $\mathrm{e}^{-(t_{k+1}-t_k)/\tau} \ll 1$, $\forall k$. In this case, we can write the equation for the update of the error term $r_k := r(t_k)$ as

$$r_{k+1} \approx (1 - \lambda\tau) r_k + \mathcal{W}(t_{k+1}) - \mathcal{W}(t_k),$$

where $r_1 = \mathcal{W}(t_1)$. Again, it should be clear there is an inverse relationship between the impact of λ and τ on the long term error in this limiting case. We compute the variance numerically from Eq. (3.53) for the case of discrete control in Fig. 3.9, demonstrating an excellent match with the neural field model Eq. (4.1).

We conclude by computing the average log error Eq. (3.47) across realizations

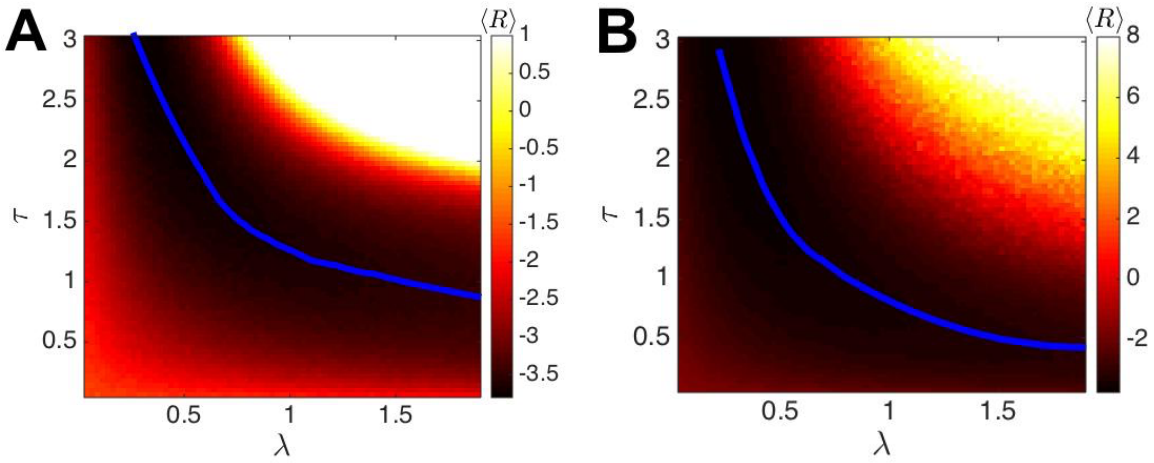

Figure 3.10: Average log error $\langle R \rangle$ computed across realizations of Eq. (3.47) for the discretely controlled low-dimensional approximation Eq. (3.53) driven by additive noise with amplitude $\varepsilon = 0.1$ as described in Eq. (4.1). (**A**) For periodic cues with spacing $\Delta t = 4$, we find that the curve (solid line) of optimal (λ, τ) values has τ decreasing with λ as in Fig. 3.7. (**B**) A similar tend is observed for exponentially distributed $p(\Delta t) = \mu e^{-\mu \Delta t}$ spacings between cue times with $\mu = 0.5$. Other parameters $v_0 = 0.15$, $\theta = 0$, and simulation time $t_f = 40$. Numerical simulations are performed using the same method as in Fig. 3.7.

of Eq. (3.51) in Fig. 3.10. Notice again that the optimal value of τ, which minimizes $\langle R \rangle$ is inversely related to the strength of control. Furthermore, this trend is preserved whether cues appear periodically in time (Fig. 3.10**A**) or at exponentially distributed intervals (Fig. 3.10**B**).

3.4 Conclusion

We have introduced and studied a neural field model of velocity integration that incorporates sensory feedback. Velocity input results in the propagation of a

bump attractor whose position encodes an animal's estimate of its position. Sensory information is assumed to come in the form of cues that are either constantly present, in the case of continuous feedback, or present at discrete points in time, in the case of discrete feedback. Our analysis has focused on one-dimensional periodic systems, wherein it is assumed the animal is navigating along a narrow annular track (Fig. 3.1**B**). This was based on the protocol used in the experiments of [12], which were used to study the effect of local cues on the sharpness of neuronal place fields. We find there is an optimal control strength λ that minimizes the long term error in the model's position estimate. This pattern holds when errors originate from spatial heterogeneities as well as dynamic fluctuations.

In Chapter 4, we introduce another method that a large scale network may employ to reduce errors. In homogeneous networks, excitatory coupling between layers can reduce diffusion [86]. We extend this idea to include the impacts of heterogeneity. In fact, we suggest heterogeneity could act as a method of storing spatial landmarks. Indeed, through a drift-diffusion approximation, we are able to derive the effective velocity and diffusion of bumps through a multilayer heterogeneous network. Heterogeneity tends to reduce diffusion, but also impacts the speed of the traveling bump. Thus, there is a cost to storing spatial landmarks. However, this trade-off positively impacts stationary bumps, as these landmark storage locations will pin the bump in place.

Chapter 4

Extensions to Multiple Bump Layers

4.1 Multilayer neural field with spatial heterogeneity

Neural field models of persistent activity have been used extensively to understand the relationships between network properties and spatiotemporal activity dynamics [19, 43]. Stable bump attractors arise as solutions to these models when network connectivity is locally excitatory and broadly inhibitory, and these solutions are translationally invariant when connectivity is also strictly distance-dependent [4, 55]. However, the incorporation of multiple neural field layers and spatial heterogeneity can break the translation invariance of single network layers, so that bumps have preferred positions within their respective layer [62, 63, 90, 91]. Our analysis focuses on a multilayer neural field model with general connectivity between layers. Spatial heterogeneity within layers, velocity input, and

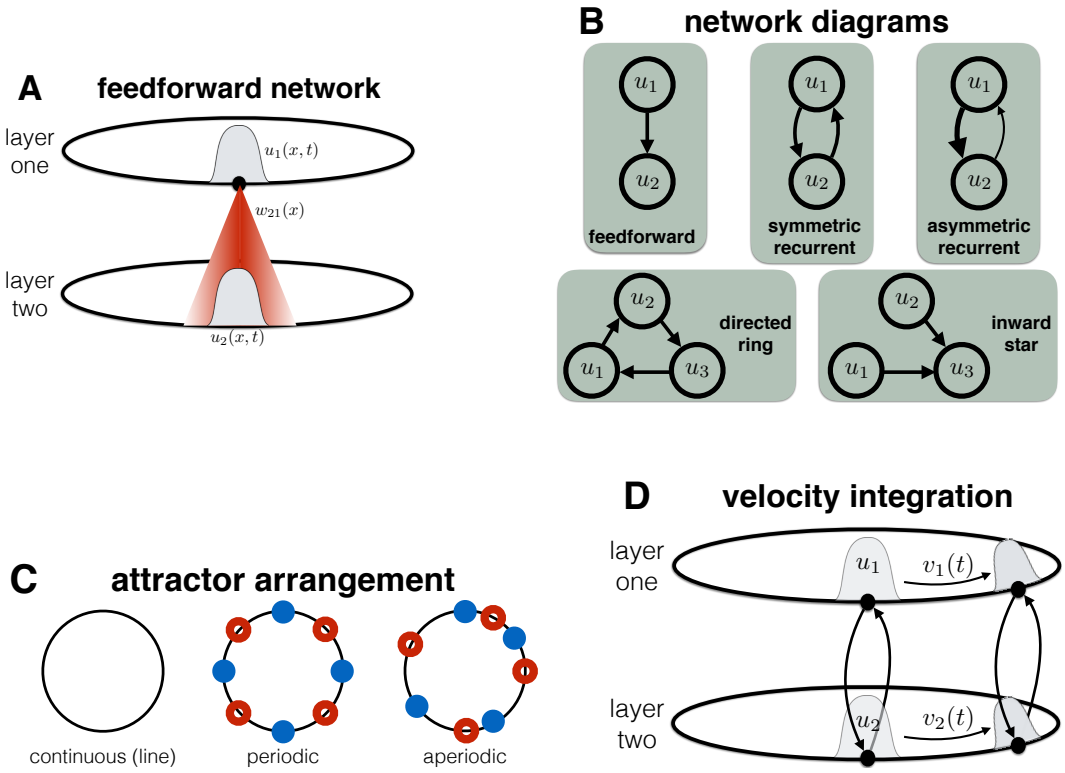

Figure 4.1: Schematic of multilayer network features. (**A**) Purely excitatory long-range interlaminar connectivity is activated by regions of high activity such as the bump attractor solution in layer 1 ($u_1(x,t)$), projecting to similarly tuned locations in layer 2, reinforcing the position of the activity bump there ($u_2(x,t)$). (**B**) Different network topologies as specified by the weight functions (w_{jk}, $j \neq k$) are explored in two layer networks (feedforward, symmetric, and asymmetric) as well as three layers (directed ring, inward star). (**C**) Local heterogeneities within each layer introduced into the recurrent weight functions w_{jj}, Eq. (4.1), generate preferred locations for the bump attractor solutions to the model Eq. (4.2). We consider a variety of networks, which possess different attractor structures in each of their constituent layers. Continuous attractors possess marginally stable bump solutions at each location around the ring, while chains of discrete attractors possess stable nodes (blue dots) where bumps prefer to reside separated by saddles (red circles). (**D**) Velocity integration via the asymmetric integral term involving w_{vjk} in Eq. (4.1) causes bump attractor solutions to move about the domain, incrementing position in proportion to the velocity amplitude.

noise are all assumed to be weak ($\mathcal{O}(\varepsilon)$):

$$\mathrm{d}u_j = \left[-u_j + \sum_{k=1}^{N} \int_{-\pi}^{\pi} w_{jk}(x,y) f(u_k(y,t)) \mathrm{d}y + \varepsilon v(t) \sum_{k=1}^{N} w_{vjk} * f(u_k) \right] \mathrm{d}t + \varepsilon dZ_j, \tag{4.1}$$

where $u_j(x,t)$ denotes the average neural synaptic input at location $x \in [-\pi, \pi]$ at time t in network layer $j \in \{1, 2, ..., N\}$, and $w_{vjk} * f(u_k) = \int_{-\pi}^{\pi} w_{vjk}(x - y) f(u_k(y,t)) \mathrm{d}y$ is a convolution. Note that we have restricted the spatial domain to be one-dimensional and periodic. There are several experimental examples of spatial working memory which operate on such a domain including oculomotor delayed-response tasks for visual memory [65, 160] as well as spatial navigation along linear tracks [12, 167]. While we suspect that several of our findings extend to two-dimensional spatial domains [117], we reserve such analysis for future work. Recurrent synaptic connectivity within layers is given by the collection of kernels $w_{jj}(x,y)$, and we allow these functions to be spatially heterogeneous, rather than simply distance-dependent. We thus define them as

$$w_{jj}(x,y) := (1 + \varepsilon h_j(y)) w_{jj}(x - y), \tag{4.2}$$

where the impact of the heterogeneity $h_j(y)$ is weak ($\varepsilon \ll 1$), and $w_{jj}(x - y)$ is only dependent on the distance $|x - y|$. As opposed to recurrent connectivity, we assume the interlaminar connectivity (w_{jk}, $j \neq k$) is homogeneous, so we can always write $w_{jk}(x,y) = w_{jk}(x - y)$. The homogeneous portion of the recurrent connectivity in each layer is locally excitatory and laterally inhibitory: e.g., the unimodal cosine function

$$w_{jj}(x - y) = \cos(x - y), \tag{4.3}$$

which we use in some of our computations. Similarly, we will often consider a cosine shaped excitatory weight function for interlaminar connectivity:

$$w_{jk}(x-y) = \bar{w}_{jk}(1+\cos(x-y)). \tag{4.4}$$

We introduce homogeneous, distance-dependent kernels for the connectivity between layers. This is motivated by recent experimental work demonstrating that several brain areas involved in spatial working memory are reciprocally coupled to one another [42, 50], and these areas all tend to have similar topographically organized delay period activity [65, 84, 131]. Thus, we expect that topologically organized connectivity would be re-enforced via Hebbian plasticity rules [95, 119]. Such connectivity functions tend to generate stationary bump solutions within each layer [76, 86, 90, 100], and we will analyze these solutions in some detail in Section 4.2. Other lateral inhibitory functions, such as sums of multiple cosine modes, will also generate stationary bump solutions but they do not qualitatively alter the dynamics of the system.

Note, the general form of the weight functions $w_{jk}(x)$ allows us to explore a variety of network topologies, and their impact on the dynamics of bump attractors. For example, it is clear that a feedforward network (Fig. 4.1**A**) will primarily be governed by the dynamics of the upstream layer. However, the dynamics of bumps in more intricate networks (Fig. 4.1**B**) are more nuanced. Applying both linear stability analysis and perturbation theory to bumps in Section 4.2, we can explore the specific impacts of different conformations of $w_{jk}(x)$. Furthermore, we expect the heterogeneities arising in local connectivity Eq. (4.2) will interact with interlaminar connectivity to shape the overall dynamics of bumps (Fig. 4.1**C**).

The effects of velocity inputs are accounted for by the second integral term in Eq. (4.1), based on a well tested model of the head direction system [141] as well as spatial navigation models that implement path integration [107, 127]. We explicitly derive this form by reducing a double ring model (Appendix A) or a $2N$ ring model (Appendix B). While some of these models use multiple layers to account for different velocity directions [30, 164], the essential dynamics are captured by a single-layer with recurrent connections modulated by velocity input [118, 168]. Since we are studying motion along a one-dimensional space, the weak ($\varepsilon \ll 1$) velocity input $\varepsilon v(t)$ to each neural activity layer $u_j(x,t)$ is given by a scalar variable which can be positive (for rightward motion) or negative (for leftward motion) as shown in Fig. 4.1**D**. We derive a reduction of the double ring model (one ring for each velocity direction) of velocity integration presented in [164] to a single layer for velocity (positive or negative) in the Appendices. The connectivity functions $w_{vjk}(x-y)$ targeting each layer j should be interpreted as interactions that are shaped by an incoming velocity signal to that layer. Essentially, this connectivity introduces asymmetry into the weight functions, which will cause shifts in the position of spatiotemporal solutions. Typically, this weight function is chosen to be of the form $w_v(x-y) = -w'(x-y)$, in single layers [168]. In the absence of any heterogeneity, such a layer will have bumps that propagate at velocity precisely equal to $\varepsilon v(t)$ [118]. As shown in the Appendices A and B, we can extend this previous assumption to incorporate velocity-related connectivity that respects the interlaminar structure of the network, so that

$$w_{vjk}(x-y) = -\frac{\mathrm{d}}{\mathrm{d}x}\left[w_{jk}(x-y)\right]. \tag{4.5}$$

As we demonstrate in Section 4.2.3, this results in bump solutions that propagate with velocity $\varepsilon v(t)$.

Dynamic fluctuations are a central feature of neural activity, and they can often serve to corrupt task pertinent signals, creating error in cognitive tasks [57]. The error in spatial working memory tasks tends to build steadily in time, in ways that suggest the process underlying the memory may evolve according to a continuous time random walk [13, 160]. As there is no evidence of long timescale correlations in the underlying noise process, we are satisfied to model fluctuations in each individual layer of our model using a spatially correlated white noise process:

$$\mathrm{d}Z_j(x,t) = \int_\Omega \mathcal{F}_j(x-y)\mathrm{d}Y_j(y,t)\mathrm{d}y,$$

where $\mathcal{F}_j$ is the spatial filter of the noise in layer j and $\mathrm{d}Y_j(x,t)$ is a spatially and temporally white noise increment. We define the mean and covariance of the vector $(\mathrm{d}Z_1, \mathrm{d}Z_2, ..., \mathrm{d}Z_n)$:

$$\langle \mathrm{d}Z_j(x,t)\rangle \equiv 0 \qquad \langle \mathrm{d}Z_j(x,t)\mathrm{d}Z_k(y,s)\rangle = C_{jk}(x-y)\delta(t-s)\mathrm{d}t\mathrm{d}s, \tag{4.6}$$

where $C_{jk}(x-y)$ is the even symmetric spatial correlation term, and $\delta(t)$ is the Dirac delta function.

Subsequently, we will analyze the existence and stability of stationary bump solutions to Eq. (4.1) in Section 4.2.1. Since we will perform this analysis under the assumption of spatially homogeneous synaptic weight functions ($h_j(x) \equiv 0$ in Eq. (4.2)), these solutions will be marginally stable to perturbations that shift their position. However, once we incorporate noise, heterogeneity, and velocity inputs in Section 4.2.3, we can perturbatively analyze their effects by linearizing about

the stationary bump solutions. The low-dimensional stochastic system we derive will allow us to study the impact of multilayer architecture on the processing of velocity inputs in Section 4.3.

4.2 Bump attractors in a multilayer neural field

Our analysis begins by constructing stationary bump solutions to Eq. (4.1) for an arbitrary number of layers N and even, translationally-symmetric synaptic weight functions $w_{jk}(x-y)$. Note, there are a few recent studies that have examined the existence and stability of stationary bump solutions to multilayer neural fields [62, 63, 86]. In particular, Folias and Ermentrout studied bifurcations of stationary bumps in a pair of lateral inhibitory neural field equations [63]. They identified solutions in which bumps occupied the same location in each layer (syntopic) as well as different locations (allotopic), and they also demonstrated traveling bumps and oscillatory bumps that emerged from these solutions. However, they did not study the general problem of an arbitrary number of N layers, and their analysis of networks with asymmetric coupling was relatively limited. Since the solutions will form the basis of our subsequent perturbation analysis of heterogeneity and noise, we will outline the existence and stability analysis of bumps first, for an arbitrary number of layers N. The reader is advised to consult the works of Folias and Ermentrout for a more detailed characterization of the possible bifurcations of stationary patterns in a pair of neural fields [62, 63]. We also note that, while we are restricting our analysis to the case of one-dimensional

domains, we expect our results to extend to two or more dimensions as demonstrated in [117]. Furthermore, previous experiments in rats have probed the behavior and neurophysiological underpinnings of spatial navigation along linear tracks [12, 167]. Thus, we believe the model we analyze here would be pertinent to these cases in which the environment is nearly one-dimensional. After we characterize the stability of stationary bump solutions, we will consider the effects of weak perturbations to these solutions, which will help reveal how noise, heterogeneity, and interlaminar coupling shape the network's processing of velocity inputs.

4.2.1 Existence of bump solutions

In the absence of a velocity signal ($v(t) \equiv 0$) and heterogeneity ($h_j(x) \equiv 0$, $\forall j$), we can characterize stationary solutions to Eq. (4.1), given by $u_j(x,t) = U_j(x)$. Conditions for the existence of stable stationary bumps in single layer neural fields have been well-characterized [4, 19, 72, 102], but much remains in terms of understanding how the form of $w_{jk}(x-y)$ would impact the existence and stability of bumps in a multilayer network. Furthermore, the stationary equations for bump solutions are a form of the well-studied Hammerstein equation [8, 74], and bump stability is characterized by Fredholm integral equations of the second kind [10]. For our purposes, we will construct bumps under the assumption that they exist. Then, we will employ self-consistency, to determine solution validity. This is straightforward in the case of a Heaviside nonlinearity $f(u) = H(u-\theta)$, Eq. (1.3), but we can derive some results for general nonlinearities $f(u)$. First, note that, in

the case of translationally symmetric kernels $w_{jk}(x-y)$, we obtain the following convolution relating stationary solutions $U_j(x)$ in each layer to one another:

$$U_j(x) = \sum_{k=1}^{N} \int_{-\pi}^{\pi} w_{jk}(x-y) f(U_k(y)) \mathrm{d}y, \quad j = 1, ..., N. \tag{4.7}$$

In later analysis, we will also find the formula for the spatial derivative useful:

$$U_j'(x) = \sum_{k=1}^{N} \int_{-\pi}^{\pi} \frac{\mathrm{d}}{\mathrm{d}x} w_{jk}(x-y) f(U_k(y)) \mathrm{d}y, \quad j = 1, ..., N. \tag{4.8}$$

Next, since each $U_j(x)$ must be periodic in $x \in [-\pi, \pi]$, we can expand it in a Fourier series

$$U_j(x) = \sum_{l=0}^{M} A_{lj} \cos(lx) + \sum_{m=1}^{M} B_{mj} \sin(mx), \tag{4.9}$$

where M is the maximal integer index of a mode for bumps in all N layers. Indeed, there will be a finite number of terms in the Fourier series, Eq. (4.9), under the assumption that the weight functions $w_{jk}(x-y)$ all have a finite Fourier expansion. Since most typical smooth weight functions are well approximated by a few terms in a Fourier series [148], we take this assumption to be reasonable. Once we do so, we can construct solvable systems for the coefficients of the bumps, Eq. (4.9), and their stability as in [35]. For even symmetric weight kernels, we can write

$$\begin{aligned} w_{jk}(x-y) &= \sum_{m=0}^{M} C_{jkm} \cos(m(x-y)) \\ &= \sum_{m=0}^{M} C_{jkm} \left[\cos(mx)\cos(my) + \sin(mx)\sin(my)\right], \end{aligned}$$

so that Eq. (4.7) implies that

$$A_{lj} = \sum_{k=1}^{N} C_{jkl} \int_{-\pi}^{\pi} \cos(lx) f(U_k(x)) \mathrm{d}x, \tag{4.10a}$$

$$B_{mj} = \sum_{k=1}^{N} C_{jkm} \int_{-\pi}^{\pi} \sin(mx) f(U_k(x)) \mathrm{d}x. \tag{4.10b}$$

Since the noise-free, heterogeneity-free system is translationally invariant, there is a family of solutions with center of mass at any location on $x \in [-\pi, \pi]$. Furthermore, the evenness of the weight functions $w_{jk}(x-y)$ we have chosen implies the resulting system is reflection symmetric, so we can restrict our examination to even solutions, so $B_{mj} \equiv 0$ for all m, j, so Eq. (4.9) becomes

$$U_j(x) = \sum_{l=0}^{N} A_{lj} \cos(x). \tag{4.11}$$

Plugging the formula Eq. (4.11) into Eq. (4.10), we find

$$A_{lj} = \sum_{k=1}^{N} C_{jkl} \int_{-\pi}^{\pi} \cos(lx) f\left(\sum_{m=0}^{N} A_{mk} \cos(mx) \right) \mathrm{d}x. \tag{4.12}$$

The coefficients A_{lj} can be found using numerical root finders [148]. However, for particular functions f and w_{jk}, we can project the system Eq. (4.12) to a much lower-dimensional set of equations, which can sometimes be solved analytically.

For instance, consider the Heaviside nonlinearity $f(u) = H(u-\theta)$, Eq. (1.3). In this case, stationary bump solutions $u_j(x,t) = U_j(x)$ centered at $x = 0$ are assumed to have superthreshold activity on the interval $x \in [-a_j, a_j]$ in each layer $j = 1, ..., N$; i.e. $U_j(x) > \theta$ for $x \in [-a_j, a_j]$. Applying this assumption to the stationary Eq. (4.7) yields

$$U_j(x) = \sum_{k=1}^{N} \int_{-a_k}^{a_k} w_{jk}(x-y) \mathrm{d}y.$$

Self-consistency then requires that $U_j(\pm a_j) = \theta$, as originally pointed out by Amari [4], which allows us to write

$$\theta = \sum_{k=1}^{N} \int_{-a_k}^{a_k} w_{jk}(a_j - y) \mathrm{d}y, \quad j = 1, ..., N. \tag{4.13}$$

Again, Eq. (4.13) is a system of nonlinear equations, which can be solved numerically via root-finding algorithms. However, as opposed to the integral terms in Eq. (4.12), the integrals in Eq. (4.13) are tractable, which makes for a more straightforward implementation of a root-finder. If we utilize the canonical cosine-weight functions, Eq. (4.3) and (4.4), we find we can carry out the integrals in Eq. (4.13) to yield:

$$\theta = \sin(2a_j) + \sum_{k \neq j} 2\bar{w}_{jk} \left[a_k + \cos(a_j) \sin(a_k) \right] . \tag{4.14}$$

Henceforth, we mostly deal with the specific case of cosine-weight connectivity, although we suspect our results extend to the case of more general weight functions. This allows us to define connectivity simply using the scalar strength values of the interlaminar coupling, which comprise the off-diagonal entries of the following matrix: $\mathcal{W}_{jk} = \left\{ \bar{w}_{jk} : j \neq k; \;\; 1 : j = k \right\}$ for $j, k = 1, ..., N$. As discussed in Section 4.1, and specifically Fig. 4.1**B**, we categorize the network graphs of primary interest to our work here into the main cases of a two-layer network and some specific cases of a network with more layers. We now briefly demonstrate how such graph structures can impact the stationary solutions, as it foreshadows the impact on the non-equilibrium dynamics of the network.

Two-layer symmetric network ($\bar{w}_{12} \equiv \bar{w}_{21} = \bar{w}$). In this case, we can derive a few analytical results concerning the bifurcation structure of stationary bump solutions. However, to identify the half-widths a_1 and a_2, it is typically necessary to solve Eq. (4.14) numerically to produce the plots shown in Fig. 4.2**A**. First of all, for double-bump solutions, in which both layers possess stationary superthreshold activity, if we assume symmetric solutions, so that $a_1 = a_2 = a$, then we can

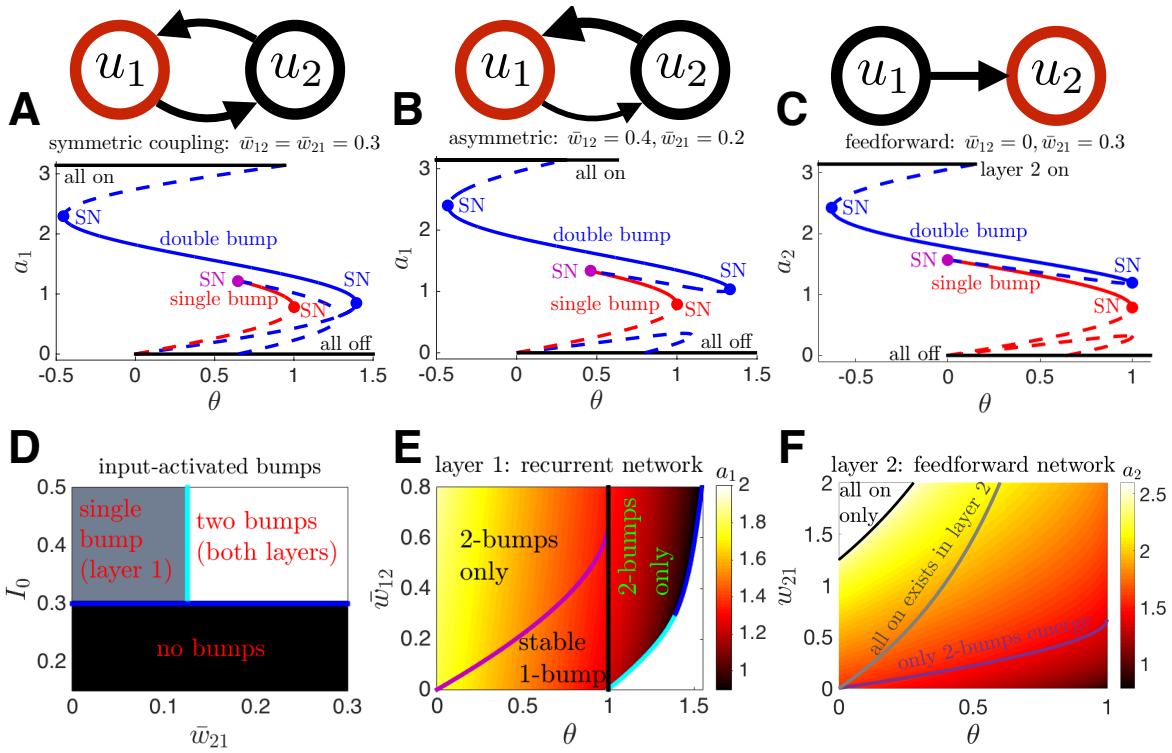

Figure 4.2: Bump half-width plots for two-layer ($N = 2$) networks with $f(u) = H(u - \theta)$, Eq. (1.3), and coupling functions Eq. (4.3) and (4.4), as given by Eq. (4.14). (**A**,**B**,**C**) Bifurcation diagrams for half-width of bumps in the red layer shown in network diagram above. (**A**) Half-width a_1 of the bump in layer u_1 in a symmetric network, plotted as a function of threshold θ, as given by Eq. (4.16). Stable (solid) and unstable (dashed) branches of double bumps annihilate in a saddle-node (SN) bifurcation at low threshold θ, and at high threshold θ. (**B**) Half-width a_1 as a function of θ in an asymmetric network, as given by Eq. (4.16). (**C**) Bump half-width a_2 in a feedforward network, given by the single Eq. (4.17), shows both single bumps and double bump branches annihilate at the same upper threshold $\theta = 1$. (**D**) Critical coupling $\bar{w}_{21}$ and input strength I_0 for $I(x) = I_0 \cos(x)$ needed to instantiate a single bump in layer 1 or a double bump solution, in a feedforward network, where $\theta = 0.3$. Shaded regions are generated by numerically simulating Eq. (4.1), and thick blue lines are calculated theoretically. (**E**) Half-width a_1 of the layer 1 bump of a double-bump solution for a recurrent network with $\bar{w}_{21} = 0.3$ over a range of coupling strength $\bar{w}_{12}$ and threshold θ. Partitions demonstrate that a stable 1-bump solution also coexists in a subregion of the domain. No 2-bumps exist in the white region. (**F**) Half-width a_2 of the layer 2 bump of a double bump solution for a feedforward network over a range of coupling strength $\bar{w}_{21}$ and threshold θ. Stable 1-bumps exist below the magenta line. For sufficiently large coupling $\bar{w}_{21}$ and low threshold, only the 'all-on' solution exists in layer 2.

write Eq. (4.14) as

$$\theta = (1 + \bar{w}) \sin(2a) + 2\bar{w}a \equiv G(a). \tag{4.15}$$

We cannot solve the transcendental Eq. (4.15) explicitly for the bump half-width a. In order to gain some insight, we can identify the range over which solutions to the equations exist. This can be determined explicitly by finding the turning points of the right hand side of Eq. (4.15) (See blue dots in Fig. 4.2**A**,**B**,**C**), corresponding to the extrema of the function between which solutions exist. Thus, we can determine the location of these turning points, which are saddle-node (SN) bifurcations, by differentiating the right hand side $G(a)$:

$$G'(a) = 2(1 + \bar{w}) \cos(2a) + 2\bar{w},$$

so by requiring $G'(a_c) = 0$, we have

$$a_c = \frac{1}{2} \cos^{-1} \left[\frac{\bar{w}}{1 + \bar{w}} \right], \; \pi - \frac{1}{2} \cos^{-1} \left[\frac{\bar{w}}{1 + \bar{w}} \right],$$

matching the locations of the double-bump SN bifurcations (blue dots) shown in Fig. 4.2**A**.

Furthermore, SN bifurcations associated with the coalescing of stable single-bump branches with unstable double-bump branches (purple dots in Fig. 4.2**A**,**B**,**C**) can be determined using a threshold condition. For instance, given a layer 1 bump with half-width a_1, we require the stationary solution in layer 2 ($u_2 = U_2(x)$) remains subthreshold ($U_2(x) < \theta$, $x \in [-\pi, \pi]$). Given $a_2 = 0$ in Eq. (4.14), single bump solutions in layer 1 satisfy $\theta = \sin(2a_1)$, so $a_u = \frac{1}{2} \sin^{-1} \theta, a_s = \frac{\pi}{2} - \frac{1}{2} \sin^{-1} \theta$ are solutions with a_s corresponding to the stable bump [90]. Thus,

we require $U_2(x) = 2\bar{w}(a_1 + \sin(a_1)\cos(x)) < \theta$, so selecting for the maximal value of $U_2(x)$ and plugging in a_s, we have an explicit equation for the critical interlaminar strength $\bar{w}$ above which there are no stable single bump solutions: $\bar{w}_c = \sin(2a_s)/\left[a_s + \sin(a_s)\right]$, providing an implicit equation for the SN locations in Fig. 4.2**A**,**B**,**C**, and corresponding to the magenta curves in Fig. 4.2**E**,**F**.

Two-layer asymmetric network ($\bar{w}_{12} \neq \bar{w}_{21}$). Double-bump solution half-widths tend to differ in this case $a_1 \neq a_2$, obeying the pair of implicit equations

$$\theta = \sin(2a_1) + 2\bar{w}_{12}\left[a_2 + \cos(a_1)\sin(a_2)\right], \tag{4.16a}$$

$$\theta = \sin(2a_2) + 2\bar{w}_{21}\left[a_1 + \cos(a_2)\sin(a_1)\right], \tag{4.16b}$$

which we solve numerically to generate the branches plotted in Fig. 4.2**B**, as well as the surface plot in Fig. 4.2**E**. Note, however, it is still possible to determine the range of values in which stable single-bump solutions exist in layer j using the requirement $\bar{w}_{kj} < \sin(2a_s)/\left[a_s + \sin(a_s)\right]$, as derived in the symmetric network case.

Two-layer feedforward network ($\bar{w}_{12} \equiv 0$). This is a special case of the asymmetric network, where the nonlinear system, Eq. (4.14), defining the bump half-widths reduces to:

$$\theta = \sin(2a_1), \quad \theta = \sin(2a_2) + 2\bar{w}_{21}\left[a_1 + \cos(a_2)\sin(a_1)\right],$$

which can further be reduced to a single implicit equation for the half-width in the target layer 2 (see schematic in Fig. 4.2**C**):

$$\theta = \sin(2a_2) + 2\bar{w}_{21}\left[\frac{\pi}{2} - \frac{1}{2}\sin^{-1}\theta + \frac{\cos(a_2)}{2}\left(\sqrt{1-\theta} + \sqrt{1+\theta}\right)\right], \tag{4.17}$$

which can be solved using numerical root finding to yield the curves in Fig. 4.2**C**,**F**.

'All-on' solutions in the two-layer network. Given excitatory interlaminar connections, it is possible to generate 'all-on' solutions in one and sometimes two layers of the network. An 'all-on' solution is one in which a layer has a stationary solution $U_j(x)$ that is entirely superthreshold, $U_j(x) > \theta$ for all $x \in [-\pi, \pi]$. In the case of a feedforward network (Fig. 4.2**C**,**F**), the target layer 2 will have an 'all-on' solution when the minimal value of $U_2(x) > 0$ given a stable bump solution $U_1(x)$ in layer 1. As a result, an 'all-on' solution in layer 2 would have the form

$$U_2(x) = 2\bar{w}_{21}\left[a_1 + \sin(a_1)\cos(x)\right],$$

so requiring $\min_x[U_2(x)] > \theta$ yields

$$\bar{w}_{21}\left[\pi - \sin^{-1}\theta - \sqrt{1-\theta} - \sqrt{1+\theta}\right] > \theta,$$

obtaining equality along the grey line plotted in Fig. 4.2**F**. For recurrent networks, we can easily identify the threshold curves $(\bar{w}_{jk}, \theta)$ above which double 'all-on' solutions exist. These have the simpler forms:

$$U_1(x) = 2\bar{w}_{12}\pi, \quad U_2(x) = 2\bar{w}_{21}\pi,$$

so we need to require that $\bar{w}_{12} > \theta/(2\pi)$ and $\bar{w}_{21} > \theta/(2\pi)$.

Critical input needed for activation of bumps. We are studying multilayer networks wherein we assume bump solutions can be instantiated by an external input. However, it is important to identify the critical input needed to nucleate and maintain such bumps in the two layers of the network. As demonstrated in Fig.

4.2**A**,**B**,**C**, there are multiple stable stationary solutions across a range of threshold θ and coupling values $(\bar{w}_{12}, \bar{w}_{21})$.

We wish to demonstrate that it is possible to instantiate a two-bump solution given only an input, $I(x) = I_0 \cos(x)$, to layer 1, and we focus exclusively on the feedforward network. This single layer will only have subthreshold activity if $I_0 \cos(x) < \theta$ everywhere. If input is superthreshold ($I_0 > \theta$), stationary bump solutions, driven by an input in layer 1, are then given [60, 76]: $U_1(x) = [2\sin(a_1) + I_0]\cos(x)$. Thus, bumps driven by inputs just beyond the critical level $I_0 = \theta$, will have half-widths approximately satisfying $\theta = \sin(2a_1) + \theta\cos(a_1)$. These bumps will have half-widths then given by the implicit equation $\theta(a_1) := \sin(2a_1)/(1-\cos(a_1)) = 2\cos(a_1)\cot(a_1/2)$. For values of $\theta(a_1) > 0$ with $a_1 \in [0, \pi]$, we can show that this function is monotone decreasing, since $\theta'(a_1) = -2\cos(a_1) - \csc^2(a_1/2) < 0$ when $0 < a_1 < a_1^c \approx 2.2372$. In this case, $\theta(a_1) \approx -0.6006$. Therefore, as $\theta(a_1)$ will tend to increase as a_1 is decreased from a_1^c, so for $\theta > 0$ we expect a single stable stationary bump solution in layer 1 (See also [60, 90]). This suggests either single-bump or double-bump solutions will emerge as long as $I_0 > \theta$, as shown in Fig. 4.2**D**. Increasing the strength of input I_0 will only serve to further stabilize this stationary bump. To determine the critical strength needed to propagate this bump forward to layer 2, we must solve for the half-width a_1 in $\theta = \sin(a_1) + I_0\cos(a_1)$, and require that layer 2 is driven superthreshold, so that $U_2(0) = 2\bar{w}_{21}\left[a_1 + \sin(a_1)\right] > \theta$. This admits an explicit inequality $\bar{w}_{21} > \frac{\theta}{2[a_1+\sin(a_1)]}$, so we need only solve for a_1 numerically to obtain the vertical boundary between single and double bump solutions in Fig. 4.2**D**.

4.2.2 Linear stability of bumps

Linear stability of the bump solutions $U_j(x)$, Eq. (4.7), can be determined by analyzing the evolution of small, smooth, separable perturbations such that $u_j(x,t) = U_j(x) + \varepsilon e^{\lambda t}\psi_j(x)$. We expect $u_j = U_j(x)$ $(j = 1, ..., N)$ to be neutrally stable to translating perturbations $\psi_j = U_j'(x)$, arising from the translation symmetry of Eq. (4.1) given $w_{jk}(x,y) = w_{jk}(x-y)$. On the other hand, the bump may be linearly stable or unstable to perturbations of its half-width a_j [4]. The results we derive here for such perturbations are what determine the stability of branches plotted in Fig. 4.2.

To begin, consider $u_j(x,t) = U_j(x) + \varepsilon\Psi_j(x,t)$, where $\Psi_j(x,t)$ thus describes perturbations to the shape of the bump $U_j(x)$ that may evolve temporally. Plugging this into the full neural field Eq. (4.1) with $h_j \equiv 0$, $Z_j \equiv 0$, and $v \equiv 0$, we can apply the stationary Eq. (4.7), and subsequently write the $\mathcal{O}(\varepsilon)$ equation as

$$\frac{\partial\Psi_j(x,t)}{\partial t} = -\Psi_j(x,t) + \sum_{k=1}^{N}\int_{-\pi}^{\pi} w_{jk}(x-y)f'(U_k(y))\Psi_k(y,t)\mathrm{d}y. \tag{4.18}$$

Due to the linearity of the equation, we may apply separation of variables to each Ψ_j, such that $\Psi_j(x,t) = b_j(t)\psi_j(x)$ [128, 148]. Substituting into Eq. (4.18), we have for each $j = 1, ..., N$:

$$\frac{b_j'(t)}{b_j(t)} = -1 + \frac{1}{\psi_j(x)}\sum_{k=1}^{N}\int_{-\pi}^{\pi} w_{jk}(x-y)f'(U_k(y))\psi_k(y)\mathrm{d}y. \tag{4.19}$$

Thus, each side of Eq. (4.19) depends exclusively on a different variable, x or t, so both must equal a constant λ. Therefore, $b_j(t) = c_j e^{\lambda t}$ for all $j = 1, ..., N$, suggesting perturbations will grow indefinitely as $t \to \infty$ for $\mathrm{Re}\lambda > 0$, indicating

instability. While oscillatory instabilities are plausible (Re$\lambda > 0$ with Im$\lambda \neq 0$), given specific forms of interlaminar coupling (e.g., combinations of interlaminar excitation and inhibition [63]), we did not identify such instabilities in the mutual excitatory layered networks we studied (Fig. 4.2). Thus, we expect instabilities emerging where Re$\lambda = 0$ will typically be of saddle-node type (Im$\lambda = 0$). Furthermore, the equation for $\psi_j(x)$ is now given for all $j = 1, ..., N$, as

$$(\lambda + 1)\psi_j(x) = \sum_{k=1}^{N} \int_{-\pi}^{\pi} w_{jk}(x - y) f'(U_k(y))\psi_k(y) \mathrm{d}y. \tag{4.20}$$

Eigenvalues λ are thus determined by consistent solutions $(\lambda, \boldsymbol{\psi}(x))$ for $\boldsymbol{\psi} = (\psi_1, \psi_2, ..., \psi_N)^T$, to Eq. (4.20). One such solution is $(\lambda, \boldsymbol{\psi}(x)) = (0, \mathbf{U}'(x))$ for $\mathbf{U}' = (U_1', U_2', ..., U_N')^T$, as can be shown by applying Eq. (4.8). As mentioned above, this demonstrates the neutral stability of bump solutions to translating perturbations, due to the translational invariance of Eq. (4.1).

Further analysis in the case of a general firing rate function $f(u)$ can be difficult. However, if we consider the Heaviside nonlinearity $f(u) = H(u - \theta)$ given by Eq. (1.3), we obtain a specific case of Eq. (4.20), which is easier to analyze [4, 45]:

$$(\lambda + 1)\psi_j(x) = \sum_{k=1}^{N} \gamma_k \Big(w_{jk}(x - a_k)\psi_k(a_k) + w_{jk}(x + a_k)\psi_k(-a_k) \Big), \tag{4.21}$$

where we have made use of the fact that

$$f'(U_j(x)) = \delta(U_j(x) - \theta) = \frac{\delta(x + a_j)}{U_j'(-a_j)} - \frac{\delta(x - a_j)}{U_j'(a_j)} = \frac{\delta(x + a_j) + \delta(x - a_j)}{|U_j'(a_j)|}, \tag{4.22}$$

since $U_j'(-a_j) = -U_j(a_j) > 0$, and we have assigned

$$\gamma_j^{-1} = |U'(a_j)| = \sum_{k=1}^{N} \left[w_{jk}(a_j - a_k) - w_{jk}(a_j + a_k) \right], \quad j = 1, ..., N, \tag{4.23}$$

under the assumption that $w_{jk}(x)$ is monotone decreasing in $|x|$, which is the case for cosine weight functions, Eq. (4.3) and (4.4). Note, all eigenfunctions $\boldsymbol{\psi}(x)$ of Eq. (4.21) that satisfy the conditions $\psi_j(\pm a_j) = 0$, for all $j = 1, ..., N$, have associated eigenvalue given by $(\lambda + 1)\boldsymbol{\psi} = 0$ so $\lambda = -1$, which does not contribute to any instabilities. To specify other eigensolutions, we examine cases where $\psi_j(\pm a_j) \neq 0$ for at least one $j = 1, ..., N$. In such cases, we can obtain expressions for the eigenvalues by examining Eq. (4.21) at the points $x = \pm a_1, \pm a_2, ..., \pm a_N$. In this case, the eigenfunctions $\boldsymbol{\psi}$ are defined by their values at the threshold-crossing points: $\psi_j(\pm a_j)$ for each $j = 1, ..., N$. Thus, defining these unknown values $A_j^{\pm} := \psi_j(\pm a_j)$, we simplify Eq. (4.21) to a linear system of $2N$ equations of the form

$$(\lambda + 1)\mathbf{v} = \mathbf{W}\mathbf{v}, \quad \mathbf{v} = (A_1^+, ..., A_N^+, A_1^-, ..., A_N^-)^T, \quad \mathbf{W} = \begin{bmatrix} \mathcal{A}_- & \mathcal{A}_+ \\ \mathcal{A}_+ & \mathcal{A}_- \end{bmatrix}, \quad (4.24)$$

where the elements of the blocks of the $2N \times 2N$ matrix $\mathbf{W}$ are $(\mathcal{A}_\pm)_{jk} = \gamma_k w_{jk}(a_j \pm a_k)$. We make use of the result $|\mathbf{W}| = |\mathcal{A}_- + \mathcal{A}_+||\mathcal{A}_- - \mathcal{A}_+|$ [136], which implies the set of eigenvalues λ_W of $\mathbf{W}$ is the union of the set of the eigenvalues of $\mathcal{A}_- + \mathcal{A}_+$ and $\mathcal{A}_- - \mathcal{A}_+$. Subsequently, the eigenvalues of $\mathbf{W} - I$ will be $\lambda = \lambda_W - 1$. We now outline a few examples in which we can compute these eigenvalues analytically.

Two-layer feedforward network. Assuming $w_{12} \equiv 0$, layer 1 sends input to layer 2, but receives no feedback from layer two. Linear stability associated with the stationary bump solutions to this model is then determined in part by computing

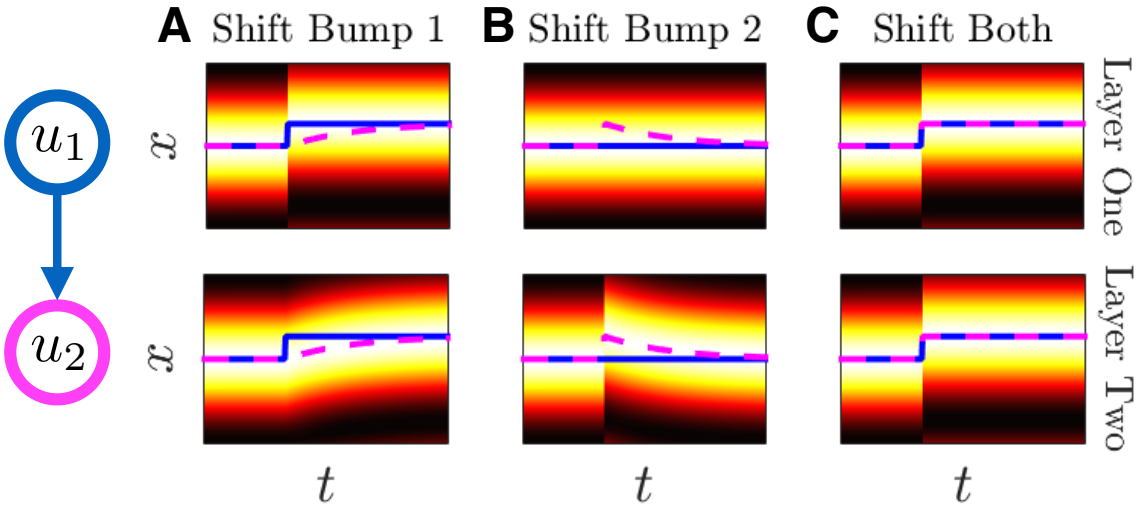

Figure 4.3: Linear stability of bumps in a feedforward two-layer network, demonstrated by simulations of the model Eq. (4.1) with $N = 2$. (**A**) When the bump in layer 1 is shifted, the bump in layer 2 (dashed line) relaxes to the new position of bump 1 (solid line). (**B**) When the bump in layer 2 is shifted, it relaxes back to the fixed position of bump 1. (**C**) When both bumps are shifted, both retain their new position, respecting the translation symmetry of the underlying Eq. (4.1).

the eigenvalues of:

$$\mathcal{A}_- + \mathcal{A}_+ = \begin{bmatrix} \gamma_1 w_{11}^+ & 0 \\ \gamma_1 w_{21}^+ & \gamma_2 w_{22}^+ \end{bmatrix}, \quad \mathcal{A}_- - \mathcal{A}_+ = \begin{bmatrix} \gamma_1 w_{11}^- & 0 \\ \gamma_1 w_{21}^- & \gamma_2 w_{22}^- \end{bmatrix}, \tag{4.25}$$

where $w_{jk}^{\pm} := \gamma_j \big(w_{jk}(a_j - a_k) \pm w_{jk}(a_j + a_k) \big)$. Since the matrices in Eq. (4.25) are triangular, their eigenvalues λ_W are given by their diagonal entries. Applying Eq. (4.23), $\gamma_j^{-1} = \sum_{k=1}^N w_{jk}^-$, we can express eigenvalues $\lambda = \lambda_W - 1$ of $\mathbf{W} - I$ as:

$$\lambda = \{\lambda_1^-, \lambda_2^-, \lambda_1^+, \lambda_2^+\} = \left\{ 0, -\frac{w_{21}^-}{w_{21}^- + w_{22}^-}, \frac{2w_{11}(2a_1)}{w_{11}^-}, \frac{2w_{22}(2a_2) - w_{21}^-}{w_{21}^- + w_{22}^-} \right\}.$$

Neutral stability with respect to the eigenfunction $\boldsymbol{\psi} = \mathbf{U}'$ ensures the existence of $\lambda_1^- = 0$. Concerning the other three eigenvalue formulae, the terms w_{jk}^- will be positive by our assumptions on the weights w_{jk} made after Eq. (4.23), so $\lambda_2^- < 0$,

corresponding to the fact that the bump in layer 2 is linearly stable to translating perturbations, when the position of the bump in layer 1 is held fixed. In Fig. 4.3, we show that the upstream layer (1) governs the long term location of both bumps. The layer 2 bump always relaxes to the layer 1 bump's location. In a related way, the eigenvalues λ_1^+ and λ_2^+ correspond to expansions/contractions of the bump widths in layers 1 and 2, respectively. Typically, there are two bump solutions in a single-layer network, whose width perturbations correspond with the eigenvalue λ_1^+: one that is narrow and unstable to such perturbations ($\lambda_1^+ > 0$), and another that is wide and stable to such perturbations ($\lambda_1^+ < 0$) [4, 45, 90]. Lastly, the bump in layer 2, driven by activity in layer 1 is influenced by features of layers 1 and 2, as shown in the formula for λ_2^+. When $2w_{22}(2a_2) < 0$, we expect $\lambda_2^+ < 0$, and the bump will be stable to width perturbations.

Exploding star network. Another example architecture involves a single layer with feedforward projections to multiple $(N-1)$ layers. In this case, $w_{jk} \equiv 0$ for $j = 2, ..., N$ and $k \neq j$. Only perturbations that shift the bump in layer 1 have a long term impact on the position of bumps in the network. The translation modes of bumps in layers $j = 2, ..., N$ have associated negative eigenvalues, as we will show, which is a generalization of the two-layer feedforward case. Linear stability is computed by first determining the eigenvalues of:

$$\mathcal{A}_- \pm \mathcal{A}_+ = \begin{bmatrix} \gamma_1 w_{11}^{\pm} & 0 & ... & 0 \\ \gamma_1 w_{21}^{\pm} & \gamma_2 w_{22}^{\pm} & ... & 0 \\ \vdots & \vdots & \ddots & \vdots \\ \gamma_1 w_{N1}^{\pm} & 0 & ... & \gamma_N w_{NN}^{\pm} \end{bmatrix}. \tag{4.26}$$

Subtracting one from the eigenvalues of the matrices in Eq. (4.26) and applying the formula for γ_j, Eq. (4.23), we find $2N$ eigenvalues, given by $\lambda_j^{\pm}$ for $j = 1, ..., N$, where

$$\lambda_1^- = 0, \quad \lambda_1^+ = \frac{2w_{11}(2a_1)}{w_{11}^-},$$

and

$$\lambda_j^- = -\frac{w_{j1}^-}{w_{j1}^- + w_{jj}^-}, \quad \lambda_j^+ = \frac{2w_{jj}(2a_j) - w_{j1}^-}{w_{j1}^- + w_{jj}^-}, \quad j = 2, ..., N.$$

As in the two-layer network, bumps are neutrally stable to perturbations of the form $\boldsymbol{\psi} = \mathbf{U}'$, corresponding to $\lambda_1^- = 0$. In addition, we expect $\lambda_j^- < 0$ for $j = 2, ..., N$ since $w_{jk}^- > 0$. As mentioned above, we would expect wide bumps to be stable to expansion/contraction perturbations, whose stability is described by the eigenvalues λ_j^+ for $j = 1, ..., N$.

Two-layer recurrent network. In the case of a fully recurrent network, where $\bar{w}_{jk} > 0$ for all $j \neq k$, all matrix entries are nonzero: $\mathcal{A}_- \pm \mathcal{A}_+ = \begin{bmatrix} \gamma_1 w_{11}^{\pm} & \gamma_2 w_{12}^{\pm} \\ \gamma_1 w_{21}^{\pm} & \gamma_2 w_{22}^{\pm} \end{bmatrix}$. First, note that $\lambda_W = 1$ is an eigenvalue of $\mathcal{A}_- - \mathcal{A}_+$, since $(w_{11}^- + w_{12}^-)(w_{22}^- + w_{21}^-) \cdot |\mathcal{A}_- - \mathcal{A}_+ - I| = w_{12}^- w_{21}^- - w_{12}^- w_{21}^- = 0$, so we denote $\lambda_1^- = 0$ as the eigenvalue describing the translation symmetry of bumps. To gain further insight, we can also compute the other three eigenvalues:

$$\lambda_2^- = -\frac{w_{12}^-}{w_{11}^- + w_{12}^-} - \frac{w_{21}^-}{w_{22}^- + w_{21}^-},$$
$$\lambda_{1,2}^+ = \frac{\gamma_1 w_{11}^+ + \gamma_2 w_{22}^+ - 2 \pm \sqrt{\omega}}{2}.$$

where

$$\omega = \left[\gamma_1 w_{11}^+ + \gamma_2 w_{22}^+ - 2\right]^2 - 4\gamma_1\gamma_2 \left[(w_{11}^+ - \gamma_1^{-1})(w_{22}^+ - \gamma_2^{-1}) - w_{12}^+ w_{21}^+\right].$$

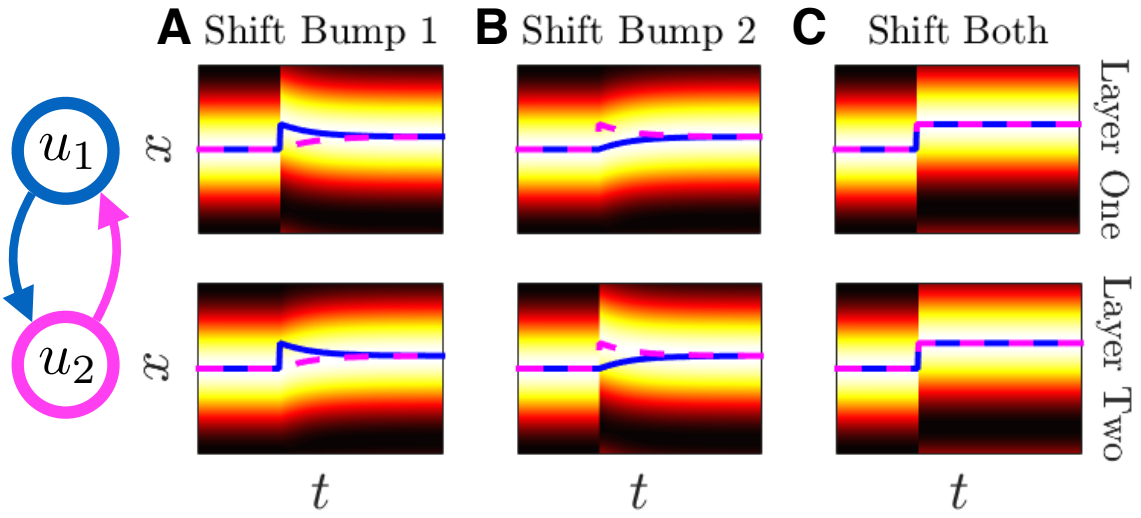

Figure 4.4: Linear stability of bumps in a two-layer symmetric recurrent network with $\bar{w}_{12} = \bar{w}_{21} > 0$, demonstrated by simulations of the model Eq. (4.1) with $N = 2$. Bumps initially at the same position $x = 0$ are perturbed to examine the resulting evolution of their positions. (**A**) When the bump in layer 1 (solid line) is shifted, both bumps relax to the average of their initially perturbed position. (**B**) When the bump in layer 2 (dashed line) is shifted, again, both bumps relax to an intermediate position. (**C**) When both bumps are shifted to the same location, both retain their new position.

For a symmetric recurrent network: $w_{jj} \equiv w$, $w_{jk} \equiv w_c$, and $\gamma_j = \gamma$ ($j = 1, 2$, $k \neq j$), these formulas reduce to $\lambda_2^- = -\dfrac{2w_c^-}{w^- + w_c^-}$ and $\lambda^+ := \lambda_{1,2}^+ = \gamma w^+ - 1 \pm w_c^+$. Bumps are linearly stable to perturbations that move them apart (Fig. 4.4**A**,**B**), and neutrally stable to translations that move them to the same location (Fig. 4.4**C**).

Imploding star graphs. Additional dimensions of neutral stability can arise in the case of more than two layers, depending on the graph defining interlaminar connectivity. For instance, if there are multiple layers $j = 1, ..., l$ that receive no feedback from other layers, then $\gamma_j w_{jj}^- = 1$ for $j = 1, ..., l$, so the first l rows of the matrix $\mathcal{A}_- - \mathcal{A}_+$ are the canonical unit vectors $\mathbf{e}_1, ..., \mathbf{e}_l$. Thus, there are at least l unity eigenvalues of $\mathbf{W}$, implying $\lambda = 0$ has multiplicity at least l in Eq. (4.24),

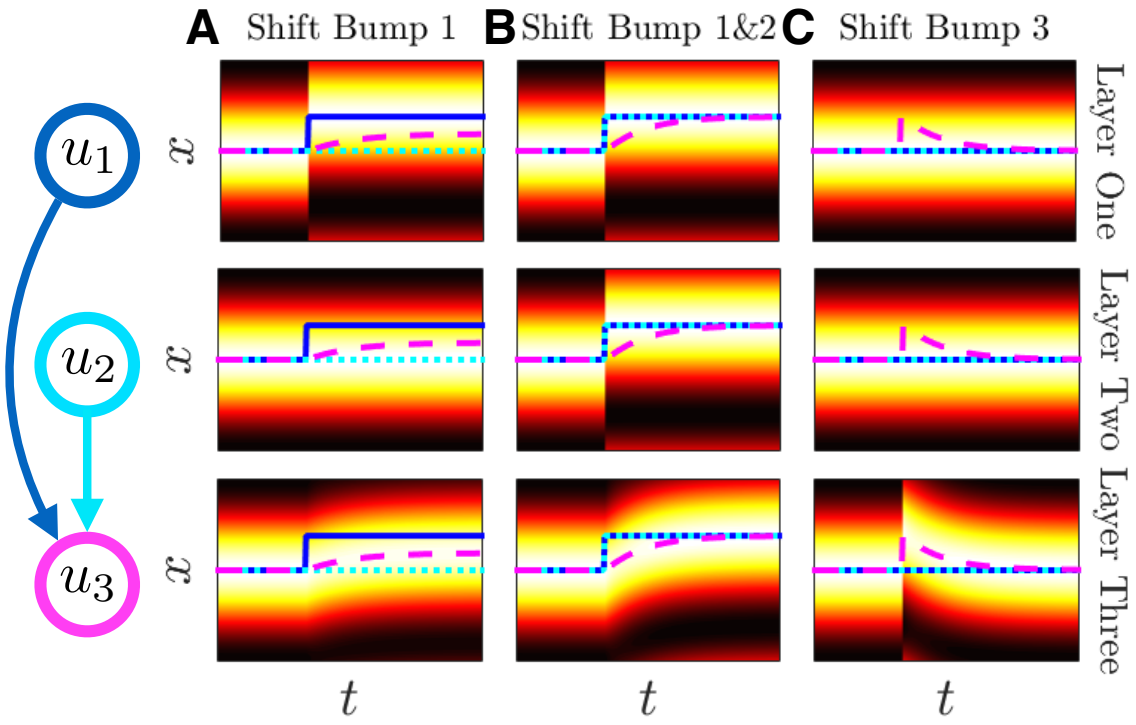

Figure 4.5: Linear stability of bumps in a $N = 3$ layer imploding star network with $\bar{w}_{jk} \equiv 0$ for $j \neq 3, k \neq j$. (**A**) When the bump in layer 1 (solid line) is shifted, the bump in layer 3 (dashed line) relaxes to a position between the layer 1 and layer 2 (dotted line) bump. (**B**) When both bumps in layers 1 and 2 are perturbed to a new location, the bump in layer 3 relaxes to that new location. (**C**) When only the bump in layer 3 is perturbed, it relaxes back to the locations of the bumps in layer 1 and 2.

corresponding to the neutral stability of bumps in the l layers that receive no feedback. We consider such an example when $N = 3$:

$$\mathcal{A}_- + \mathcal{A}_+ = \begin{bmatrix} \gamma_1 w_{11}^+ & 0 & 0 \\ 0 & \gamma_2 w_{22}^+ & 0 \\ \gamma_1 w_{31}^+ & \gamma_2 w_{32}^+ & \gamma_3 w_{33}^+ \end{bmatrix}, \quad \mathcal{A}_- - \mathcal{A}_+ = \begin{bmatrix} 1 & 0 & 0 \\ 0 & 1 & 0 \\ \gamma_1 w_{31}^- & \gamma_2 w_{32}^- & \gamma_3 w_{33}^- \end{bmatrix}.$$

Eigenvalues of Eq. (4.24) are then $\lambda_j^- = 0$ and $\lambda_j^+ = \dfrac{w_{jj}^+ - w_{jj}^-}{w_{jj}^-}$ for $j = 1, 2$, and

$$\lambda_3^- = \frac{-(w_{12}^- + w_{13}^-)}{w_{11}^- + w_{12}^- + w_{13}^-}, \qquad \lambda_3^+ = \frac{w_{33}^+ - (w_{31}^- + w_{32}^- + w_{33}^-)}{w_{31}^- + w_{32}^- + w_{33}^-}.$$

Bumps in both layers 1 and 2 are neutrally stable to translations (Fig. 4.5**A**,**B**), whereas the bump in layer 3 is linearly stable to translation, relaxing to a weighted average of the positions of the layers 1 and 2 bumps (Fig. 4.5**C**). Adding dimensions to the space of translation symmetric perturbations will change the low-dimensional approximation that captures the dynamics of multilayer bump solutions in response to noise perturbations (Compare Sections 4.2.3 and 4.4).

Directed loop of N layers. As a last example, we consider an N-layer directed loop, wherein each layer provides feedforward synaptic input to a subsequent layer. As a result, there is a band of nonzero interlaminar coupling along $w_{j+1,j}$ for $j = 1, .., N$ (replace $N + 1$ with 1). Again, there is a zero eigenvalue λ in Eq. (4.24), since

$$\mathcal{A}_- - \mathcal{A}_+ = \begin{bmatrix} \gamma_1 w_{11}^- & 0 & \cdots & \gamma_N w_{1N}^- \\ \gamma_1 w_{21}^- & \gamma_2 w_{22}^- & 0 & \cdots \\ 0 & \ddots & \ddots & 0 \\ 0 & 0 & \gamma_{N-1} w_{N,N-1}^- & \gamma_N w_{NN}^- \end{bmatrix}.$$

Our desired result can be demonstrated by computing the determinant of the bidiagonal matrix:

$$|\mathcal{A}_- - \mathcal{A}_+ - I| = \prod_{j=1}^{N} (\gamma_j w_{jj}^- - 1) - \prod_{j=1}^{N} \left[-\gamma_j w_{j+1,j} \right] = 0,$$

replacing $j-1=0$ with N in the case $j=1$. We have applied the fact that $\gamma_j^{-1}=w_{jj}^{-}+w_{j,j-1}^{-}$ to transform the first product to the form of the second.

4.2.3 Derivation of the effective equations

Our stability analysis has provided us insight into the qualitative behavior of the multilayer bump solutions when small perturbations are applied. The underlying architecture both within and between layers shapes the response. We now extend our linear stability results to study the impact of persistent noise perturbations to stationary bump solutions, with heterogeneity as described by Eq. (4.2) and velocity input described by Eq. (4.5). We begin by assuming that first, we only need to consider a single stochastically-evolving position, $\Delta(t)$, corresponding to the relative location of the entire multilayer bump solution. This assumes a single dimension of translation symmetry in the linear stability problem of the bump solution, computed in Section 4.2.2. Cases in which more than one such dimension exists will be analyzed in Section 4.4. Secondly, we assume a separation of timescales between the position and width perturbations of each bump, leading to the ansatz: $u_j(x,t):=U_j(x-\Delta(t))+\varepsilon\Phi_j(x-\Delta(t),t)$, where Φ_j describes the dynamics of shape perturbations to the bump in layer j. In line with previous studies of the impact of noise on patterns in neural fields [19, 90], the displacement of the bump from its initial position is assumed to be weak and slow, so that $\Delta(t)$ and $\mathrm{d}\Delta(t)$ are $\mathcal{O}(\varepsilon)$. We find that the results of our perturbation analysis are consistent with this assumption. Since the spatial heterogeneity, velocity, and noise are all scaled by ε, we expect them to enter into the derived effective equation. Note, in

the case of weak interlaminar coupling, we would consider a separate stochastic variable Δ_j for each layer's bump [24, 86]. Plugging our ansatz into Eq. (4.1) and disregarding higher order terms $\mathcal{O}(\varepsilon^2)$, the following equation in $\mathcal{O}(\varepsilon)$ remains:

$$\begin{aligned} \mathrm{d}\Phi_j(x,t) = &\Bigg[\mathcal{L}_j\big[\mathbf{\Phi}(x,t)\big] + \int_{-\pi}^{\pi} h_j(y+\Delta) w_{jj}(x-y) f(U_j(y))\mathrm{d}y \\ &\quad + v(t)\sum_{k=1}^{N}\int_{-\pi}^{\pi} w_{vjk}(x-y) f(U_k(y))\mathrm{d}y\Bigg]\mathrm{d}t \\ &\quad + \varepsilon^{-1}\mathrm{d}\Delta U_j'(x) + \mathrm{d}Z_j(x,t), \end{aligned} \tag{4.27}$$

where $\mathcal{L}_j$ is the j^{th} element of the linear functional $\mathcal{L}:\mathbf{p}\mapsto\mathbf{q}$ for $\mathbf{p}=(p_1,p_2,...,p_N)^T$ and $\mathbf{q}=(q_1,q_2,...,q_N)^T$, defined as

$$\mathcal{L}_j\big[\mathbf{p}(x)\big] = -p_j(x) + \sum_{k=1}^{N}\int_{-\pi}^{\pi} w_{jk}(x-y) f'(U_k(y)) p_k(y)\mathrm{d}y, \qquad j=1,...,N,$$

with adjoint operator $\mathcal{L}^*:\mathbf{q}\mapsto\mathbf{p}$, defined $\langle\mathcal{L}\mathbf{p},\mathbf{q}\rangle = \langle\mathbf{p},\mathcal{L}^*\mathbf{q}\rangle$ under the standard L^2 inner product, and thus given element-wise by

$$\mathcal{L}_j^*\big[\mathbf{q}(x)\big] = -q_j(x) + f'(U_j(x))\sum_{k=1}^{N}\int_{-\pi}^{\pi} w_{kj}(x-y) q_k(y)\mathrm{d}y, \qquad j=1,...,N,$$

note the exchange in the order of the indices in $w_{kj}(x)$. Note also that Eq. (4.27) suggests that Δ and $\mathrm{d}\Delta$ should be $\mathcal{O}(\varepsilon)$. To ensure boundedness of solutions $\mathbf{\Phi}(x,t)$, we require the inhomogeneous portion of Eq. (4.27) to be orthogonal to the nullspace of the adjoint operator $\mathcal{L}^*$. The nullspace of $\mathcal{L}^*$ is defined as the solution to the equation $\mathcal{L}^*\big[\boldsymbol{\varphi}(x)\big]=0$, $\boldsymbol{\varphi}=(\varphi_1,\varphi_2,...,\varphi_N)^T$, such that

$$\varphi_j(x) = f'(U_j(x))\sum_{k=1}^{N}\int_{-\pi}^{\pi} w_{kj}(x-y)\varphi_k(y)\mathrm{d}y. \tag{4.28}$$

To derive explicit solutions to Eq. (4.28), we must make further assumptions on either the firing rate function $f(u)$ or the weight functions $w_{jk}(x)$. For instance, if

we assume symmetric interlaminar connectivity, such that $w_{jk}(x) \equiv w_{kj}(x)$ for all $j,k = 1,...,N$, then we can show that $\varphi_j(x) = f'(U_j(x))U_j'(x)$ (for all $j = 1,...,N$) is a solution to Eq. (4.28). This can be verified by applying integration by parts after plugging the expression into the integrand:

$$\begin{aligned}\varphi_j(x) &= f'(U_j)\sum_{k=1}^{N} w_{kj}(x) * \left[f'(U_k(x))U_k'(x)\right] \\ &= f'(U_j)\sum_{k=1}^{N} w_{jk}(x) * \left[f'(U_k(x))U_k'(x)\right] \\ &= f'(U_j)\frac{\mathrm{d}}{\mathrm{d}x}\sum_{k=1}^{N} w_{jk}(x) * f(U_k(x)) = f'(U_j(x))U_j'(x),\end{aligned}$$

where we have applied Eq. (4.8) in the last equality. Solutions can also be found for more general weight functions ($w_{jk}(x) \not\equiv w_{kj}(x)$), assuming $f(u) = H(u-\theta)$, the Heaviside nonlinearity, Eq. (1.3), as we demonstrate in Section 4.2.4.

Assuming we can solve Eq. (4.28), we enforce boundedness by taking the inner product of $\boldsymbol{\varphi}(x)$ with Eq. (4.27). For the time being, we assume the null space of $\mathcal{L}^*$ is one-dimensional, and address other cases in Section 4.4. Thus, we take the null vector $\boldsymbol{\varphi}(x)$ and compute its inner product with the inhomogeneous portion of Eq. (4.27) to yield:

$$\begin{aligned}0 = \sum_{j=1}^{N}\Bigg\langle \varphi_j(x), \Bigg[\mathcal{L}_j\left[\boldsymbol{\Phi}(x,t)\right] + \int_{-\pi}^{\pi} h_j(y+\Delta)w_{jj}(x-y)f(U_j(y))\mathrm{d}y \\ + v(t)\sum_{k=1}^{N} w_{vjk} * f(U_k)\mathrm{d}y\Bigg]\mathrm{d}t + \varepsilon^{-1}\mathrm{d}\Delta U_j'(x) + \mathrm{d}Z_j(x,t)\Bigg\rangle.\end{aligned}$$

Rearranging terms leads to the following one-dimensional stochastic differential equation:

$$\mathrm{d}\Delta(t) = \left[q(\Delta(t)) + \varepsilon v(t)\right]\mathrm{d}t + \mathrm{d}\mathcal{Z}(t), \tag{4.29}$$

where the terms on the right hand side include a weighted average of each layer's: (a) spatial heterogeneity $q(\Delta)$, (b) velocity $\varepsilon v(t)$, and (c) noise $\mathcal{Z}(t)$. The impact of local spatial heterogeneity in each layer on the effective position $\Delta(t)$ is given by

$$q(\Delta) = \varepsilon\Upsilon\left[\sum_{j=1}^{N}\int_{-\pi}^{\pi}\varphi_j(x)\left(\int_{-\pi}^{\pi}h_j(y+\Delta)w_{jj}(x-y)f(U_j(y))\mathrm{d}y\right)\mathrm{d}x\right], \quad (4.30)$$

where

$$\Upsilon = -\left(\sum_{j=1}^{N}\mu_j\right)^{-1}, \quad \mu_j = \int_{-\pi}^{\pi}\varphi_j(x)U_j'(x)\mathrm{d}x, \quad j=1,...,N, \quad (4.31)$$

so in the absence of any velocity or noise, local attractors of the network are given by $\bar{\Delta}$ where $q(\bar{\Delta}) = 0$. Furthermore, the potential function, which determines statistical quantities such as mean first-passage times, is given by $Q(\Delta) = -\int_{-\pi}^{\Delta} q(s)\mathrm{d}s$. Next, note that the effective velocity input to the multilayer bump solution is precisely $\varepsilon v(t)$, which can be shown by applying our assumption on the weight functions $w_{vjk}(x)$, Eq. (4.5), to compute

$$\Upsilon\left[v(t)\sum_{j=1}^{N}\int_{-\pi}^{\pi}\varphi_j(x)\sum_{k=1}^{N}\int_{-\pi}^{\pi}w_{vjk}(x-y)f(U_k(y))\mathrm{d}y\mathrm{d}x\right] = v(t),$$

where we have reduced the numerator by applying Eq. (4.8). Finally, the effective noise to the stochastic position variable $\Delta(t)$ is given by the spatially averaged and weighted process

$$\mathrm{d}\mathcal{Z}(t) = \varepsilon\Upsilon\left[\sum_{j=1}^{N}\int_{-\pi}^{\pi}\varphi_j(x)\mathrm{d}Z_j(x,t)\mathrm{d}x\right],$$

which has zero mean $\langle\mathcal{Z}(t)\rangle = 0$ and variance $\langle\mathcal{Z}(t)^2\rangle = \bar{D}t$, where we can apply

Eq. (4.6) for noise correlations to compute

$$\bar{D} = \sum_{j=1}^{N}\sum_{j=1}^{N} D_{jk},$$

$$D_{jk} = \varepsilon^2\Upsilon^2 \int_{-\pi}^{\pi}\int_{-\pi}^{\pi} \varphi_j(x)\varphi_k(y)C_{jk}(x-y)\mathrm{d}y\mathrm{d}x, \quad j,k = 1,...,N, \tag{4.32}$$

demonstrating the contribution of the effective noise acting on $\Delta(t)$ will be determined by a weighted average of the noises from each layer $j = 1,...,N$. To determine specific features of the dynamics of Eq. (4.29), we further define constituent functions of the model Eq. (4.1). To begin, we reduce the formulae considerably by focusing on the Heaviside nonlinearity, $f(u) = H(u-\theta)$, Eq. (1.3), allowing for analytic calculations of the above quantities.

4.2.4 Results for a Heaviside firing rate

As demonstrated in Section 4.2.2, assuming the firing rate function is a Heaviside nonlinearity, $f(u) = H(u-\theta)$, Eq. (1.3), can allow for direct calculation of eigensolutions to the linear stability problem for bumps ($\lambda\boldsymbol{\psi} = \mathcal{L}\boldsymbol{\psi}$). Identifying the nullspace of the adjoint linear operator is a related problem ($\mathcal{L}^*\boldsymbol{\varphi} \equiv 0$), and assuming $f(u) = H(u-\theta)$ projects the infinite-dimensional problem to a $2N$-dimensional linear system. We then need only solve for a vector whose entries correspond to the coefficients of delta functions, as discussed in [88]. To demonstrate, we first apply our formula for the derivative $f'(U_j(x)) = \gamma_j\left[\delta(x-a_j) + \delta(x+a_j)\right]$, Eq. (4.22), and our formula for γ_j, Eq. (4.23). The delta functions contained in $f'(U_j(x))$ concentrate Eq. (4.28) for $\varphi_j(x)$ at the set of $2N$ points of the bump radii, $x = \{\pm a_1, \pm a_2, ..., \pm a_N\}$. This suggest the ansatz $\varphi_j(x) = \alpha_j\delta(x-a_j) + \beta_j\delta(x+$

a_j). Plugging these assumptions into Eq. (4.28) reduces it to the form:

$$\begin{aligned}\varphi_j(x) &= \gamma_j \left[\delta(x-a_j)+\delta(x+a_j)\right] \sum_{k=1}^{N} \int_{-\pi}^{\pi} w_{kj}(x-y)\left(\alpha_k\delta(y-a_j)+\beta_k\delta(y+a_j)\right) \mathrm{d}y \\ &= \gamma_j \sum_{k=1}^{N} \left[\alpha_k w_{kj}(a_j-a_k)+\beta_k w_{kj}(a_j+a_k)\right] \delta(x-a_j) \\ &\quad + \gamma_j \sum_{k=1}^{N} \left[\alpha_k w_{kj}(a_j+a_k)+\beta_k w_{kj}(a_j-a_k)\right] \delta(x+a_j), \quad j=1,...,N.\end{aligned}$$

Recalling that we have defined $\varphi_j(x) = \alpha_j\delta(x-a_j)+\beta_j\delta(x+a_j)$, we generate equations for the constants α_j and β_j ($j=1,...,N$) by requiring self-consistency at $x=\{\pm a_1, \pm a_2, ..., \pm a_N\}$:

$$\alpha_j = \gamma_j \sum_{k=1}^{N} \alpha_k w_{kj}(a_j-a_k)+\beta_k w_{kj}(a_j+a_k), \;\; \beta_j = \gamma_j \sum_{k=1}^{N} \alpha_k w_{kj}(a_j-a_k)+\beta_k w_{kj}(a_j+a_k),$$

for $j=1,...,N$, which can be expressed concisely as the $2N$-dimensional linear system:

$$\mathbf{z} = \mathbf{W}^*\mathbf{z}, \quad \mathbf{z} = \begin{pmatrix} \boldsymbol{\alpha} \\ \boldsymbol{\beta} \end{pmatrix} = (\alpha_1,...,\alpha_N,\beta_1,...,\beta_N)^T, \quad \mathbf{W}^* = \begin{bmatrix} \mathcal{A}_-^* & \mathcal{A}_+^* \\ \mathcal{A}_+^* & \mathcal{A}_-^* \end{bmatrix}, \tag{4.33}$$

where $\mathbf{W}^*$ is the adjoint of the matrix defined in Eq. (4.24), the linear stability problem for stationary bumps. The system, Eq. (4.33), can be written out in terms of its block matrix structure as

$$\boldsymbol{\alpha} = \mathcal{A}_-^*\boldsymbol{\alpha} + \mathcal{A}_+^*\boldsymbol{\beta}, \quad \boldsymbol{\beta} = \mathcal{A}_-^*\boldsymbol{\beta} + \mathcal{A}_+^*\boldsymbol{\alpha}, \tag{4.34}$$

which can be rearranged into the corresponding block matrix equations for $\boldsymbol{\alpha}_\pm = \boldsymbol{\alpha} \pm \boldsymbol{\beta}$:

$$\boldsymbol{\alpha}_+ = \left(\mathcal{A}_-^* + \mathcal{A}_+^*\right)\boldsymbol{\alpha}_+, \quad \boldsymbol{\alpha}_- = \left(\mathcal{A}_-^* - \mathcal{A}_+^*\right)\boldsymbol{\alpha}_-. \tag{4.35}$$

For a nontrivial solution to Eq. (4.34) to exist, there must be a nontrivial solution to either system in Eq. (4.35). As demonstrated in Section 4.2.2, there is always a nontrivial solution to $\mathbf{x} = (\mathcal{A}_- - \mathcal{A}_+)\,\mathbf{x}$, corresponding to the translation symmetric perturbation of the linear stability operator defined in Eq. (4.20). As this implies an eigenvalue of unity associated with $(\mathcal{A}_- - \mathcal{A}_+)$, there must also be an eigenvalue of unity associated with $(\mathcal{A}_-^* - \mathcal{A}_+^*)$. In general, we do not expect nontrivial solutions to $\mathbf{x} = (\mathcal{A}_- + \mathcal{A}_+)\,\mathbf{x}$, and thus expect none for $\boldsymbol{\alpha}_+ = (\mathcal{A}_-^* + \mathcal{A}_+^*)\,\boldsymbol{\alpha}_+$. This means, we expect $\boldsymbol{\alpha}_+ \equiv \mathbf{0}$, so $\boldsymbol{\beta} \equiv -\boldsymbol{\alpha}$. Thus, we need only solve the N-dimensional system $\boldsymbol{\alpha} = (\mathcal{A}_-^* - \mathcal{A}_+^*)\,\boldsymbol{\alpha}$. Applying these results to Eq. (4.29), we find a more tractable form for the integral terms defining each of the components:

$$q(\Delta) = \varepsilon\Upsilon \sum_{j=1}^{N} \alpha_j \int_{-a_j}^{a_j} h_j(y+\Delta)\left[w_{jj}(a_j - y) - w_{jj}(a_j + y)\right] \mathrm{d}y,$$

where now $\Upsilon = \left(2\sum_{j=1}^{N} \alpha_j |U_j'(a_j)|\right)^{-1}$ for $j = 1, ..., N$, using the fact that $U'(-a_j) = -U_j'(a_j) > 0$. Lastly, note the summed components of effective diffusion coefficient $\bar{D}$ are given by direct evaluations of the correlation functions

$$D_{jk} = 2\varepsilon^2\Upsilon^2\alpha_j\alpha_k\left[C_{jk}(a_j - a_k) - C_{jk}(a_j + a_k)\right], \qquad j,k = 1, ..., N,$$

reflecting the fact that noise primarily impacts the threshold-crossing points of the bumps, initially at $x = \pm a_j$, $j = 1, ..., N$.

Mirroring our discussion in the linear stability Section 4.2.2, we now discuss those cases with respect to the adjoint problem and note how they reflect the results derived there.

Two-layer feedforward network. Assuming $w_{12} \equiv 0$, layer 1 receives no feedback

from layer 2. In this case, the coefficients α_1 and α_2 are given by

$$\alpha_1 = \frac{w_{11}^- \alpha_1 + w_{21}^- \alpha_2}{w_{11}^-}, \qquad \alpha_2 = \frac{w_{22}^- \alpha_2}{w_{21}^- + w_{22}^-}, \tag{4.36}$$

which has solutions $\alpha_2 = 0$ and α_1 arbitrary, so the dynamics of the reduced system is entirely determined by those of layer 1. Layer 2 tracks the motion of the bump in layer 1, since $\alpha_2 = 0$: $\bar{D} = D_{11}$ and $q(\Delta) = -\varepsilon\mu_1^{-1} \int_{-\pi}^{\pi} \varphi_1(x) \int_{-\pi}^{\pi} h_1(y + \Delta) w_{11}(x - y) f(U_1(y)) \mathrm{d}y \mathrm{d}x$.

Exploding star network. For an arbitrary number of layers N, and $w_{jk} \equiv 0$ for $j = 2, ..., N$ and $k \neq j$, layer 1 receives no feedback from other layers and layers $2, ..., N$ only receive input from layer 1. In this case, the coefficients α_j are given

$$\alpha_1 = \frac{\sum_{k=1}^{N} w_{k1}^- \alpha_k}{w_{11}^-}, \qquad \alpha_j = \frac{w_{jj}^- \alpha_j}{w_{jj}^- + w_{j1}^-}, \tag{4.37}$$

which has solutions $\alpha_j = 0$ for $j \neq 1$ and α_1 arbitrary. All other layers track layer 1, thus the dynamics of the independent layer 1: $\bar{D} = D_{11}$ and $q(\Delta) = -\varepsilon\mu_1^{-1} \int_{-\pi}^{\pi} \varphi_1(x) \int_{-\pi}^{\pi} h_1(y + \Delta) w_{11}(x - y) f(U_1(y)) \mathrm{d}y \mathrm{d}x$. We shall treat the case of an imploding star in Section 4.4.

Two-layer recurrent network. In the case of a fully recurrent network, $\bar{w}_{jk} > 0$ for all $j \neq k$, we find the $N = 2$ case yields the following set of equations for α_1 and α_2:

$$\alpha_1 = \frac{w_{11}^- \alpha_1}{w_{11}^- + w_{12}^-} + \frac{w_{21}^- \alpha_2}{w_{11}^- + w_{12}^-}, \qquad \alpha_2 = \frac{w_{12}^- \alpha_1}{w_{22}^- + w_{21}^-} + \frac{w_{22}^- \alpha_2}{w_{22}^- + w_{21}^-},$$

which can be reduced to the much simpler single equation, $w_{12}^- \alpha_1 = w_{21}^- \alpha_2$, so clearly $(\alpha_1, \alpha_2) = (w_{21}^-, w_{12}^-)$ is a solution as shown in [88]. Thus, if $w_{21}(x)$ is the stronger connectivity function, then α_1 will tend to be larger and layer 1 will

have a larger influence on the overall dynamics. We see this clearly in the limiting feedforward case, in which $w_{12}(x) \equiv 0$.

Directed loop of N layers. Lastly, we consider a directed loop of N layers, wherein $w_{jk} \equiv 0$ unless $k = j$ or $k = j - 1$ ($k = N$ for $j = 1$). In this case, the equations for α_j are written

$$\alpha_j = \frac{w_{jj}^- \alpha_j}{w_{jj}^- + w_{j,j-1}^-} + \frac{w_{j+1,j}^- \alpha_{j+1}}{w_{jj}^- + w_{j,j-1}^-}, \quad j = 1, ..., N,$$

where $j - 1 = N$ for $j = 1$ and $j + 1 = 1$ for $j = N$. Rearranging terms demonstrates that $w_{j,j-1}^- \alpha_j = w_{j+1,j}^- \alpha_{j+1}$, so $\alpha_j = 1/w_{j,j-1}^-$ ($j = 1, ..., N$) satisfies the system.

4.3 Numerical simulations

In this section, we perform further analysis on Eq. (4.29) and compare with numerical simulations of Eq. (4.1). We are mainly interested in the interaction between noise and the spatial heterogeneity described by the nonlinear function $q(\Delta)$ in Eq. (4.29). In the absence of any velocity input, $v(t) \equiv 0$, we compute an effective diffusion coefficient D_{eff}, approximating the variance of $\Delta(t)$ given any periodic heterogeneity $q(\Delta)$ (Fig. 4.6**A**). In essence, we must compute the mean first-passage time for trips between local attractors of Eq. (4.29). Velocity inputs subsequently tilt the potential determined by $Q(\Delta) = -\int_{-\pi}^{\Delta} [q(s) + \varepsilon v(t)]\, \mathrm{d}s$, so there is a bias in the direction of escapes from local attractors (Fig. 4.6**B**). Importantly, noise allows for propagation of bumps in instances where bumps would

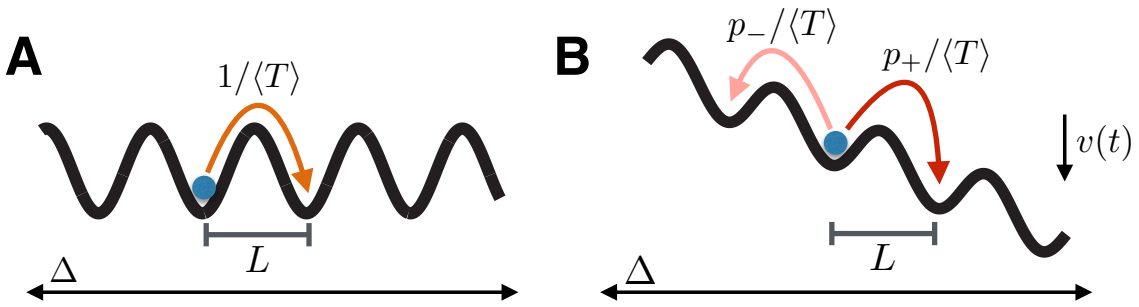

Figure 4.6: Effective diffusion and velocity calculations for the low-dimensional system, Eq. (4.29). For a gradient function $q(\Delta)$ with period L, we can determine the average (**A**) diffusion of $\Delta(t)$ when $v(t) \equiv 0$ and (**B**) velocity when $v(t) \neq 0$. (**A**) The effective diffusion coefficient $D_{eff} = L^2/(2\langle T\rangle)$ approximates the motion of the bump by tracking hops between neighboring potential wells that are distance L apart, where average time between hops is $\langle T\rangle$ [90, 105, 124]. (**B**) Velocity inputs tilt the potential $Q(\Delta)$, so, for example, the probability of a rightward transition is greater than a leftward one ($p_+ > p_-$). In this case, the bump has a nonzero effective velocity, approximated $v_{eff} = L(p_+ - p_-)/\langle T\rangle$ [105].

otherwise be stationary. We demonstrate the details of this analysis, and compare with simulations below.

4.3.1 Specific multilayer architectures

We now focus on specific examples of Eq. (4.29), where statistics of the resulting dynamics can be determined semi-analytically.

Two-layer networks. We begin by assuming $N = 2$ with internal coupling is $w_{jj}(x) = \cos(x)$ with local heterogeneity $h_j(x) = \sigma_j \cos(n_j x)$ and interlaminar connectivity $w_{jk}(x) = \bar{w}_{jk}(1 + \cos x)/2$ ($j = 1, 2$, $k \neq j$). Note, this distinguishes this study from previous work in [86, 88], which assumed homogeneous connectivity. We determined in Section 4.2.4 that $\alpha_1 = w_{21}^-$ and $\alpha_2 = w_{12}^-$, allowing us to

calculate the integrals in Eq. (4.30) directly

$$q(\Delta) = -2\varepsilon\Upsilon\Big(w_{21}^{-}\mathcal{C}_1\sin(a_1)\sin(n_1\Delta) + w_{12}^{-}\mathcal{C}_2\sin(a_2)\sin(n_2\Delta)\Big)$$

where Υ is given by Eq. (4.31) as

$$\Upsilon = \frac{1}{2\big(w_{21}^{-}\sin(a_1)(2\sin(a_1) + \bar{w}_{12}\sin(a_2)) + w_{12}^{-}\sin(a_2)(2\sin(a_2) + \bar{w}_{21}\sin(a_1)\big)}$$

and the impact of the heterogeneities scales like

$$\mathcal{C}_j = \sigma_j\frac{2n_j\sin(a_j)\cos(n_ja_j) - 2\cos(a_j)\sin(n_ja_j)}{n_j^2 - 1}, \qquad j = 1, 2, \tag{4.38}$$

for $n_j \neq 1$. When $n_j = 1$, we may take the limit as $n_j \to 1$ of Eq. (4.38) so that $\mathcal{C}_j = \sigma_j\big(\sin(a_j)\cos(a_j) - a_j\big)/2$. Finally, we specify the spatial noise correlations as $C_{jj}(x) = \pi\cos(x)$ for $j = 1, 2$ and $C_{jk}(x) \equiv 0$ for $k \neq j$, so $D_{jk} \equiv 0$ for $k \neq j$ and the noise $\mathcal{Z}_t$ has diffusion coefficient

$$\bar{D} = D_{11} + D_{22} = 4\varepsilon^2\Upsilon^2\pi\left[\big(w_{21}^{-}\big)^2\sin^2(a_1) + \big(w_{12}^{-}\big)^2\sin^2(a_2)\right].$$

We now examine two specific cases of two-layer networks, simplifying these formulae further.

Two-layer feedforward network. In the case $\bar{w}_{12} = 0$, formulae for α_1 and α_2 are given in Eq. (4.36), and without loss of generality we can set $\alpha_1 = 1$ and $\alpha_2 = 0$. Stochastic dynamics of the multilayer bump are thus approximated by the dynamics of the bump in layer 1, so bump in layer 2 tracks bump 1's position. The nonlinearity $q(\Delta) = -\varepsilon\mathcal{C}_1\sin(n_1\Delta)/(2\sin(a_1))$ and the diffusion coefficient $\bar{D} = D_{11} = \pi\varepsilon^2/(4\sin^2(a_1))$. Thus, the effective potential determining the bump's position $\Delta(t)$ is:

$$Q(\Delta) := -\int_{-\pi}^{\Delta}\left[q(s) + \varepsilon v(t)\right]\mathrm{d}s = -\frac{\varepsilon\mathcal{C}_1\cos(n_1\Delta(t))}{2n_1\sin(a_1)} - \varepsilon v(t)\Delta(t).$$

We use this in determining the theoretical curves plotted in Figs. 4.7 and 4.8, which we calculate in Section 4.3.2. Essentially, we project the dynamics of Eq. (4.29) to a continuous-time Markov process whose transition rates are determined by the escape times from the local attractors, as illustrated in Fig. 4.6.

Two-layer symmetric network. In the case $\bar{w}_{jk} = \bar{w}_c$, we have $a_j = a$ and $\alpha_j = 1$ ($j = 1, 2, k \neq j$), yielding the simplified equations for the heterogeneity, $q(\Delta) = -\varepsilon \left[\mathcal{C}_1 \sin(n_1\Delta) + \mathcal{C}_2 \sin(n_2\Delta)\right] / \left[(4 + 2\bar{w}_c)\sin(a)\right]$, and for the diffusion coefficient, $\bar{D} = \pi\varepsilon^2 / \left[2(2 + \bar{w}_c)^2 \sin^2(a)\right]$. Note, the effective noise has diffusion coefficient that is substantially decreased as opposed to the single-layer or feedforward case [88]. Fluctuations are dampened by introducing loops in the connectivity of the multilayer network. Again, these functional forms are utilized in Figs. 4.7 and 4.8.

Exploding star network. These results can also be generalized to N-layer networks that possess a valid one-dimensional projection described by Eq. (4.29). Another example is that of an exploding star, discussed in Section 4.2.4. Assuming $w_{jk} \equiv 0$ for $j = 2, ..., N$ and $k \neq j$, the coefficients, as computed in Eq. (4.37), are $\alpha_j = 0$ for $j > 1$ and $\alpha_1 = 1$. Thus, the dynamics of the stochastically-driven bump solution are determined by the dynamics of the independent layer 1, and other layers track these dynamics. Also, the constituent functions of the low-dimensional approximation will be exactly that of the two-layer feedforward example.

Directed loop of N layers. Finally, we demonstrate the calculations for a directed loop of N layers, wherein $w_{jk} \equiv 0$ unless $k = j$ or $k = j - 1$ ($k = N$ for $j = 1$).

The coefficients $\alpha_j = 1/w^-_{j,j-1}$, as computed in Section 4.2.4. Assuming $h_j(x) = \sigma_j \cos(n_j x)$, $w_{j,j-1}(x) = \bar{w}_{j,j-1}\big(1+\cos(x)\big)/2$, and $w_{jj}(x) = \cos(x)$, our low-dimensional approximation has form

$$q(\Delta) = -2\varepsilon\Upsilon \sum_{j=1}^{N} \frac{\mathcal{C}_j \sin(a_j)}{w^-_{j,j-1}} \sin(n_j\Delta), \qquad \bar{D} = 4\varepsilon^2\pi\Upsilon^2 \sum_{j=1}^{N} \left(\frac{\sin(a_j)}{w^-_{j,j-1}}\right)^2,$$

with Υ defined by Eq. (4.31). The coefficients $\mathcal{C}_j$ are a function of a_j which have the form $\mathcal{C}_j = 2\sigma_j \left[n_j \sin(a_j)\cos(n_j a_j) - \cos(a_1)\sin(n_j a_j)\right]/(n_j^2 - 1)$ for $n_j \neq 1$ and $\mathcal{C}_j = \sigma_j\big(\sin(a_j)\cos(a_j) - a_j\big)/2$ for $n_j = 1$. Consider symmetry in the strength of synaptic connectivity, so that $\bar{w}_{j,j-1} = \bar{w}_c$ and $a_j = a$ for $j = 1, ..., N$, and

$$q(\Delta) = -\varepsilon \frac{\sum_{j=1}^{N} \mathcal{C}_j \sin(n_j\Delta)}{N(2+\bar{w}_c)\sin(a)}, \quad \bar{D} = \frac{\varepsilon^2\pi}{N(2+M_1)^2\sin^2(a)}.$$

We use these results in Fig. 4.7**C**.

With the constituent functions known, we analyze the stochastic differential equation to approximate the mean position $\langle\Delta(t)\rangle$ and variance $\langle\Delta^2(t)\rangle$ of the bump's position.

4.3.2 Effective diffusion and velocity of the low-dimensional model

Velocity integration must often be performed by spatial working memory networks involved in navigation or the head direction system [68, 94, 107]. We consider the two main sources of error that could be incurred by a heterogeneous network subject to fluctuations. First, noise-driven diffusion of the remembered position will cause a degradation of spatial memory over time [40, 91]. Second, heterogeneities will lead to erroneous integration of the velocity inputs, since the

network will not integrate them perfectly [26, 134]. Thus, errors made in encoding the true position will arise from the noise term $\mathrm{d}\mathcal{Z}_t$ in Eq. (4.29) as well as the heterogeneity $q(\Delta)$, so $\mathrm{d}\mathcal{Z}_t \equiv 0$ and $q(\Delta) \equiv 0$ would yield perfect integration. We can asymptotically quantify these contributions to error by approximating (a) the effective diffusion: $\langle \Delta^2(t) \rangle - \langle \Delta(t) \rangle^2 \approx D_{eff} t$, and (b) the effective velocity: $\langle \Delta(t) \rangle \approx v_{eff} t$.

Effective diffusion. To compare with our results from full numerical simulations, we begin by deriving the effective diffusion coefficient of a bump evolving in a spatially heterogeneous network. This leverages previous results on transport in periodic potentials [105, 124]. In the absence of velocity inputs, $v(t) \equiv 0$, we can approximate the stochastic motion of a bump by tracking the nearest positional attractor to its vicinity [90, 91]. Given a gradient function $q(\Delta)$ in Eq. (4.29), attractors $\bar{\Delta}$ obey $q(\bar{\Delta}) = 0$. For instance, gradient functions of the form $q(\Delta) = -|K| \sin(n\Delta)$ have stable (unstable) attractors at $\bar{\Delta}_s = \frac{2j\pi}{n}$ ($\bar{\Delta}_u = \frac{(2j+1)\pi}{n}$). In our network, the distance x_s between two stable attractors may not be equal to the period L of the gradient function ($q(\Delta) = q(\Delta + L)$). In this case, we can either: (a) construct the corresponding continuous-time Markov chain model and compute the stochastic motion as such or (b) use a first passage time calculation to determine the mean time $\langle T \rangle$ until the bump evolves one period L and use this in the standard effective diffusion calculation. We opt for the latter, so to begin, we note the general form of the effective diffusion coefficient (Details of the

derivation can be found in [90, 91, 105]):

$$D_{eff} = \frac{\bar{D} \cdot L^2}{\langle T \rangle} = \frac{\bar{D} \cdot L^2}{\int_0^L \int_0^L \mathrm{e}^{Q(x)-Q(y)} \mathrm{d}y \mathrm{d}x}, \tag{4.39}$$

where $Q(\Delta) = -\int_{-\pi}^{\Delta} q(s)\mathrm{d}s$ is the potential given by integrating the gradient function as such. In the case of gradient functions $q(\Delta) = \sum_{j=1}^{N} K_j \sin(n_j \Delta)$, the period of the potential will be $L = (2\pi)/n_{min}$ where $n_{min} = \min\{n_1, ..., n_N\}$. Integrals in Eq. (4.39) arising from simple trigonometric-potential functions like $Q(\Delta) = \kappa \cos(n\Delta)$ can be expressed in terms of modified Bessel functions [90, 91]. However, the mixed mode potentials of interest do not yield integrals that can be evaluated analytically. Thus, for our comparisons with numerical simulations in Figs. 4.7 and 4.9, we simply evaluate these integrals using numerical quadrature.

We find that the asymptotic approximation $\langle \Delta^2(t) \rangle \approx D_{eff} t$ captures the trends in numerical simulations reasonably well. In Fig. 4.7**A**, we analyze the diffusion of bumps in a multilayer network with the same spatial heterogeneity function in each layer ($h_1(x) \equiv h_2(x)$). As in previous work [86], increasing the strength of interlaminar connectivity decreases the rate at which the variance scales in time. Furthermore, the purely feedforward network has far-higher variance than a network with weakly recurrent coupling, since the network bump position is controlled by a single layer. As a result, the noise cancelation that arises from recurrent coupling is not apparent. In Fig. 4.7**B**, we study the effects of having two layers with different spatial heterogeneity ($h_1(x) = \sigma_1 \cos(4x)$, $h_2(x) = \sigma_2 \cos(8x)$). Note the multimodal shape of the effective potential $Q(\Delta)$. As a result, different feedforward architectures ($1 \mapsto 2$ vs. $2 \mapsto 1$) can lead to substantially different

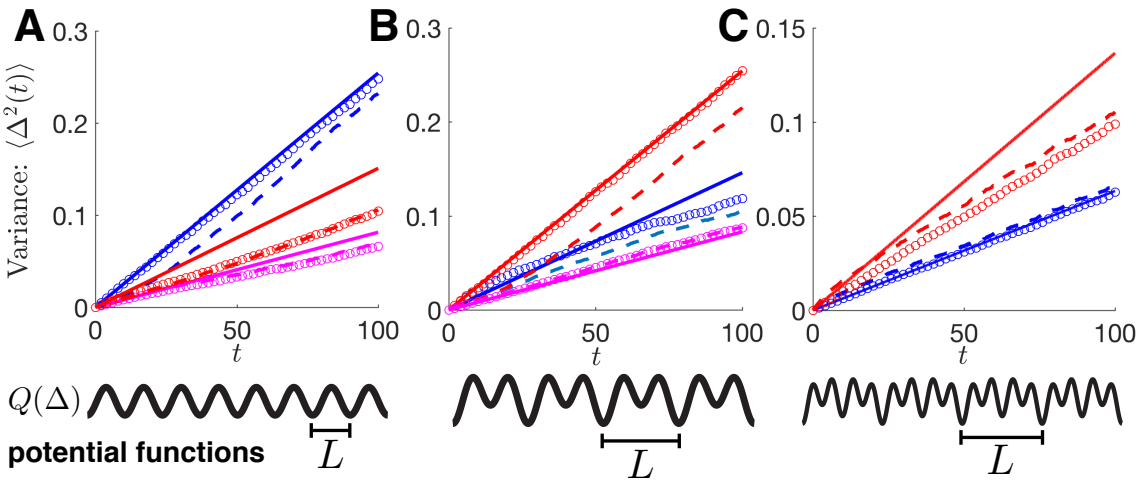

Figure 4.7: Variance $\langle \Delta^2(t) \rangle$ of the bump solutions in the absence of a velocity input ($v(t) \equiv 0$) for fixed heterogeneities $h_j(x) = \sigma_j \cos(n_j x)$ ($j = 1, 2$) and varied interlaminar connectivity strengths $\bar{w}_{12}$ and $\bar{w}_{21}$. Qualitative descriptions of the associated potential functions $Q(\Delta)$ of each network are plotted below each panel. (**A**) Plots in the case of symmetric heterogeneity ($n_1 = n_2 = 8$; $\sigma_1 = \sigma_2 = 0.25$) with feedforward connectivity (blue curves: $\bar{w}_{12} = 0.3, \bar{w}_{21} = 0$), asymmetric connectivity (red curves: $\bar{w}_{12} = 0.3, \bar{w}_{21} = 0.1$), and symmetric connectivity (magenta curves: $\bar{w}_{12} = \bar{w}_{21} = 0.3$). We find that statistics calculated from numerical simulations of the low-dimensional system (circles), Eq. (4.29) are well matched to statistics of simulations of the full model (dashed line), Eq. (4.1). Variances approximated by our effective diffusion calculation $\langle \Delta^2(t) \rangle = D_{eff} t$, Eq. (4.39), are given by solid lines. Note, as interlaminar connectivity increases in strength, the variance scales more slowly with time. (**B**) Plots in the case of asymmetric heterogeneity ($n_1 = 4$, $n_2 = 8$; $\sigma_1 = 0.05$, $\sigma_2 = 0.25$) where the the low-frequency ($n_1 = 4$), more stable layer determines dynamics (blue curves: $\bar{w}_{12} = 0.3, \bar{w}_{21} = 0$); high-frequency ($n_2 = 8$), less stable layer determines dynamics (red curves: $\bar{w}_{12} = 0, \bar{w}_{21} = 0.3$); and symmetric coupling (magenta curves: $\bar{w}_{12} = \bar{w}_{21} = 0.3$). (**C**) Plots for a system with $N = 3$ layers where the heterogeneity: $h_1(x) = 0.01 \cos(4x)$, $h_2(x) = 0.025 \cos(8x)$, $h_3(x) = 0.25 \cos(16x)$. Connectivity is taken to be feedforward (red curves: $\bar{w}_{21} = \bar{w}_{32} = 0.3$, $\bar{w}_{jk} = 0$ for all other $k \neq j$) and a symmetric loop (blue curves: $\bar{w}_{13} = \bar{w}_{21} = \bar{w}_{32} = 0.3$, $\bar{w}_{jk} = 0$ for all other $k \neq j$). In all panels, $\varepsilon = 0.1$. Numerical simulations of the full model, Eq. (4.1), were performed using Euler-Maruyama with timestep $dt = 0.01$ with direct integration of convolution using $dx = 0.01$ and 10^6 realizations to compute ensemble statistics.

variances, depending on whether the more stable layer 1 or less stable layer 2 determines the dynamics. Lower-frequency spatial heterogeneities tend to stabilize bumps more to stochastic perturbations, generally leading to a lower effective diffusion [90, 91]. Here, we show that this feature influences which interlaminar coupling architectures are best for reducing variance in spatial working memory. Lastly, we study a three-layer network in Fig. 4.7**C**. A fully recurrent architecture reduces the diffusion of the bump more than a feedforward architecture, even when the feedforward architecture is dominated by the layers that are more robust to noise perturbations ($h_1(x) = \sigma_1 \cos(4x)$, $h_2(x) = \sigma_2 \cos(8x)$). When interlaminar coupling from the less stable layer is incorporated ($h_3(x) = \sigma_3 \cos(16x)$), variance drops. Having validated our theory of effective diffusion for networks without velocity inputs, we now study the interaction of velocity inputs, noise, and spatial heterogeneity in multilayer networks.

Effective velocity. We now explore the impact of noise and spatial heterogeneity on the integration of velocity. While an analogous formula for the effective diffusion could also be derived, the results are quite similar to the case of no velocity inputs discussed above. Thus, we primarily consider how noise and heterogeneity contribute to the integration of velocity, as this will also be the main source of error when the network is integrating velocity.

Consider a velocity function $v(t)$ that is piecewise constant in time ($v(t) \equiv v_j$ on $t_j < t < t_{j+1}$), corresponding to the saltatory motion common to foraging animals [110]. In this case, we can approximate the effective velocity v_{eff} of bumps in the spatial working memory network, Eq. (4.1), by again computing the mean

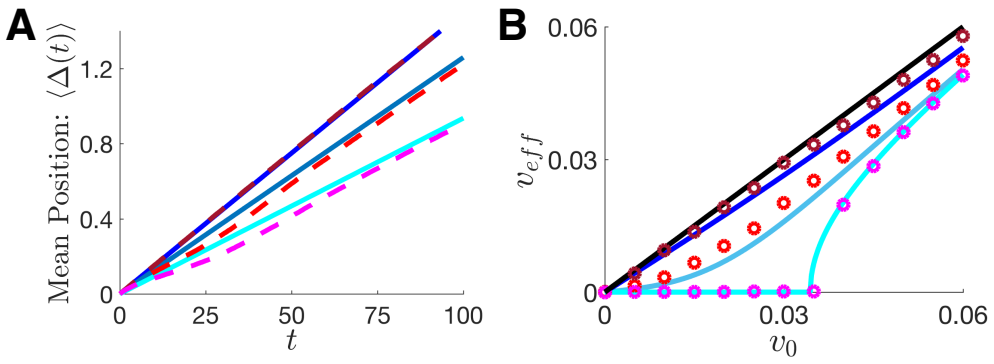

Figure 4.8: Bumps driven by velocity inputs ($\varepsilon v(t) \equiv v_0 > 0$) impacted by spatial heterogeneities ($h_1(x) = \sigma_1 \cos(n_1 x)$, $h_2(x) = \sigma_2 \cos(n_2 x)$) and noise. (**A**) Plots of the mean bump position $\langle \Delta(t) \rangle$ for homogeneous networks (top lines: $\sigma_1 = \sigma_2 = 0$), identical heterogeneity (middle lines: $n_1 = n_2 = 16$; $\sigma_1 = \sigma_2 = 1$), and differing heterogeneity (bottom lines: $n_1 = 8, n_2 = 16$; $\sigma_1 = \sigma_2 = 1$) in the layers. Note the top lines represent perfect integration of the $v_0 = 0.015$ velocity input in the ensemble average $\langle \Delta(t) \rangle$, whereas incorporating heterogeneity slows the propagation of bumps, so the velocity is integrated imperfectly. The theoretical lines (solid) computed from Eq. (4.40) match the results of numerical simulations (dashed lines) quite well. (**B**) Plot of the effective velocity v_{eff} of the ensemble versus the input velocity v_0 as the noise strength is varied (bottom to top: $\varepsilon = 0, 0.1, 0.2$. We fix the heterogeneity so that $n_1 = n_2 = 8$ in all curves, and $\varepsilon \sigma_j = 0.4$, so that even in the limit of no noise ($\varepsilon \to 0$), there is spatial heterogeneity. In the absence of noise, heterogeneity causes the bump to become pinned for sufficiently small velocity input v_0. Introducing noise causes the average effective velocity $v_{eff} = \langle \Delta(t) \rangle / t$ to approach the input velocity v_0. Blue solid lines are from theory Eq. (4.40), and circles are from numerical simulations. Black line is $v_{eff} = v_0$. For both panels, the coupling strength is symmetric: $\bar{w}_{12} = \bar{w}_{21} = 0.3$. Numerical simulations of the full model (dashed lines) are as described in Fig. 4.7.

time of a transit of the variable $\Delta(t)$ across one period L of the potential $Q(\Delta)$. We slightly abuse the notion of a period, since the velocity input v_j will skew the potential as $Q(\Delta) = -\int_{-\pi}^{\Delta} q(s) \mathrm{d}s - \varepsilon v_j \Delta$, so really L represents the period of the $q(\Delta)$ portion of the potential. Our approximation proceeds by tracking the expected number of hops the bump makes. Hops occur when the bump leaves the vicinity of its local attractor and arrives in the vicinity of a neighboring attractor,

presumably a distance L away. Note, for multimodal potentials, we must account for the multiple attractors in a single period L, but we forgo those details here. Hops can be rightward $\chi_+(t)$ or leftward $\chi_-(t)$, so we track the difference $\chi(t) := \chi_+(t) - \chi_-(t)$ to determine the rightward displacement. Shifting coordinates to assume the bump begins at $\Delta(0) = 0$, we can approximate the position of the bump $\Delta(t) = L \cdot \chi(t)$. Since the counting process $\chi(t)$ is Markovian, we need only know the hop rates $p_\pm/\langle T\rangle$ to compute $\langle \chi(t)\rangle = [p_+ - p_-]\, t/\langle T\rangle$, where p_+ (p_-) is the probability of a rightward (leftward) hop. The escape probabilities $p_\pm$, mean escape time $\langle T\rangle$, and effective velocity of the bump $v_{eff} = L \cdot \chi(t)\rangle/t$ can be calculated directly from Eq. (4.29) with the potential $Q(\Delta)$:

$$\begin{aligned} v_{eff} =& \frac{L(p_+ - p_-)}{\langle T\rangle}, \quad p_+ = 1 - p_- = \frac{1}{1 + \mathrm{e}^{-v_0 L/\bar{D}}}, \\ \langle T\rangle =& \frac{p_+}{\bar{D}} \int_0^L \int_{x-L}^x \mathrm{e}^{\frac{Q(x)-Q(y)}{\bar{D}}} \mathrm{d}y \mathrm{d}x. \end{aligned} \tag{4.40}$$

We compare our formula for the effective velocity, Eq. (4.40), to results from numerical simulations in Fig. 4.8**A**. As the amplitude of heterogeneity increases, the effective speed of traveling bumps decreases, given identical velocity input. This is in line with previous studies on the impact of heterogeneities on wave propagation [17, 118]. However, we also show that as the amplitude of noise is increased, the effective velocity v_{eff} gets closer to v_0 (Fig. 4.8**B**). This is due to the fact that noise-induced transitions between local attractors become more frequent, and the motion of the bump reflects the asymmetry in the potential $Q(\Delta)$. In the case of large-amplitude noise, $\bar{D} \gg 1$, we can approximate the transition probabilities and mean first-exit time in Eq. (4.40) using linearization in the small parameter

$1/\bar{D}$: $p_+ \approx \frac{1}{2} + \frac{v_0 L}{4D}$ and $\langle T \rangle \approx \frac{L^2}{2\bar{D}}$, yielding $v_{eff} \approx v_0$. Thus, while the effective diffusion will also tend to increase with $\bar{D}$, the effective velocity will grow to more closely match the true input velocity, similar to results discussed in the optimal-transport framework of [105].

In the absence of noise ($\bar{D} \to 0$), we can no longer assume the bump stochastically transitions between local attractors. In fact, for persistent propagation in the network to occur, the gradient function $q(\Delta)$ must have no zeroes, so that $\dot{\Delta}(t) = q(\Delta) > 0$ for all Δ, assuming $v_0 > 0$. In this case, we can compute the time $T_L = \int_0^L \frac{d\Delta}{q(\Delta)}$ it takes to traverse a single period L, and compute the effective velocity: $v_{eff} = L/T_L$ (For more details, see[118]). For example, when $\dot{\Delta}(t) = -K\sin(n\Delta) + v_0$, the time it takes to traverse the length $L = 2\pi/n$ is $T_L = 2\pi/\left[m\sqrt{v_0^2 - K^2}\right]$ so $v_{eff} = 2\pi/(mT) = \sqrt{v_0^2 - K^2}$. Clearly, if $v_0 \leq K$, this theory predicts the bump becomes pinned to a local attractor of the network, due to the spatial heterogeneity. The lower curve in Fig. 4.8**B** compares this theory with simulations of the noise-free version of the model Eq. (4.1), and indeed we find that heterogeneities then pin bumps so that $v_{eff} = 0$, in the absence of noise. On the other hand, the bump propagates in the presence of noise, so the velocity signal is detectable whereas it would not be in a noise-free paradigm, providing an example of stochastic resonance [106].

We conclude that, not only does our low-dimensional approximation describe bump dynamics in a multilayer network, it provides further insight into how heterogeneity, noise, and interlaminar coupling impact the encoding of input signals.

Noise degrades positional information, but strong spatial heterogeneity and interlaminar coupling can stabilize bump positions over long-delay periods. While heterogeneity disrupts integration of velocity inputs, sufficiently strong noise can restore mean-bump propagation speeds to be close to the input velocity. Thus, there is a tradeoff between the stabilizing effects of heterogeneity and the resulting disruption of velocity integration, which we shall explore more in future work.

4.4 Networks with multiple independent modules

Our reduction to the low-dimensional system carried out in Section 4.2.3 relied on the assumption that the multilayer bump solution possessed one marginally stable mode of perturbation. Thus, noise and velocity perturbations were always effectively integrated by the bumps in each layer by the same amount, so the multilayer bump moved coherently. However, if the interlaminar weight functions w_{jk} of the network Eq. (4.1) are defined such that multiple layers receive no feedback from other layers, those independent layers only integrate perturbations of their own activity. Consider the three-layer imploding star network presented in Fig. 4.5: Shifting the bump in layer 1 does not impact the dynamics of the layer 2 bump. Thus, only noise perturbations local to those layers impact their activity (Fig. 4.9). This suggests we need to modify our derivation of a low-dimensional system to account for this independence.

This idea can be applied to a class of cases wherein $w_{jk} \equiv 0$ for $j = 1, ..., M$, where $M \leq N$, and $k \neq j$. With this assumption, we must now assume each

bump in each layer $j = 1, ..., M$ has an independent phase Δ_j. Subsequently, the remaining phases Δ_k for $k = M+1, ..., N$ depend on the first M phases. Since layers $1, ..., M$ dominate the dynamics, we ignore the impacts of heterogeneity in layers $M+1, ..., N$, so $h_j(x) \equiv 0$ for $j = M+1, ..., N$. To begin, we consider the ansatz $u_j(x,t) = U_j(x - \Delta_j(t)) + \epsilon \Phi_j(x - \Delta_j(t), t)$ for all $j = 1, ..., N$. Plugging this into Eq. (4.1) and truncating to $\mathcal{O}(\epsilon)$, we have:

$$\begin{aligned} \mathrm{d}\Phi_j = &\left[\mathcal{L}_j\big[\mathbf{\Phi}\big] + w_{jj}(x) * \big[f(U_j(x))h_j(x+\Delta_j)\big] + v(t)\sum_{k=1}^{N} w_{vjk} * f(U_k) \right] \mathrm{d}t \\ &+ \varepsilon^{-1}\mathrm{d}\Delta_j U_j' + \mathrm{d}Z_j, \quad j = 1, ..., M, \end{aligned} \tag{4.41a}$$

$$\begin{aligned} \mathrm{d}\Phi_j = &\left[\mathcal{L}_j\left[\mathbf{\Phi}\right] + v(t)\sum_{k=1}^{N} w_{vjk} * f(U_k) + \sum_{k\neq j} w_{jk} * \left[f'(U_k)U_k'\right](\Delta_j - \Delta_k) \right] \mathrm{d}t \\ &+ \varepsilon^{-1}\mathrm{d}\Delta_j U_j' + \mathrm{d}Z_j, \quad j = M+1, ..., N, \end{aligned} \tag{4.41b}$$

where we have linearized the terms

$$f(U_j(x + \Delta_j - \Delta_k)) = f(U_j(x)) + f'(U_j(x))U_j'(x)(\Delta_j - \Delta_k)$$

and recall $F(x) * G(x) = \int_{-\pi}^{\pi} F(x-y)G(y)\mathrm{d}y$. While the linearization in $(\Delta_j - \Delta_k)$ assumes the quantity remains small, our approximation performs reasonably well, even when bumps are substantially separated in numerical simulations (Fig. 4.9). Note, $\mathcal{L}_j$ is the j^{th} element of the linear functional $\mathcal{L} : \mathbf{p} \mapsto \mathbf{q}$ for $\mathbf{p} = (p_1, p_2, ..., p_N)^T$ and $\mathbf{q} = (q_1, q_2, ..., q_N)^T$, defined as

$$\begin{aligned} \mathcal{L}_j\big[\mathbf{p}(x)\big] &= -p_j(x) + w_{jj}(x) * \left[f'(U_j(x))p_k(x)\right], && j = 1, ..., M, \\ \mathcal{L}_j\big[\mathbf{p}(x)\big] &= -p_j(x) + \sum_{k=1}^{N} w_{jk}(x) * \left[f'(U_k(x))p_k(x)\right], && j = M+1, ..., N, \end{aligned}$$

with adjoint operator $\mathcal{L}^* : \mathbf{q} \mapsto \mathbf{p}$, defined $\langle \mathcal{L}\mathbf{p}, \mathbf{q} \rangle = \langle \mathbf{p}, \mathcal{L}^*\mathbf{q} \rangle$ under the standard L^2 inner product, and thus given element-wise by given for $j = 1, ..., N$,

$$\mathcal{L}_j^* \left[\mathbf{q}(x) \right] = -q_j(x) + f'(U_j(x)) \left[w_{jj}(x) * q_j(x) + \sum_{k \neq j;\ k=M+1}^{N} w_{kj}(x) * q_k(x) \right].$$

To ensure boundedness of solutions $\mathbf{\Phi}(x,t)$, we require the inhomogeneous portion of Eq. (4.41) to be orthogonal to the nullspace of the adjoint operator $\mathcal{L}^*$. Vectors $\boldsymbol{\varphi} = (\varphi_1, \varphi_2, ..., \varphi_N)^T$ that reside in the nullspace of $\mathcal{L}^*$ are solutions to the equation $\mathcal{L}^* \left[\boldsymbol{\varphi}(x) \right] = 0$, such that

$$\varphi_j(x) = f'(U_j(x)) \left[w_{jj}(x) * \varphi_j(x) + \sum_{k \neq j;\ k=M+1}^{N} w_{kj}(x) * \varphi_k(x) \right], \quad j = 1, ..., N. \tag{4.42}$$

Solutions of Eq. (4.42) can be identified by recalling the formula for the spatial derivative of $U_j(x)$, given by Eq. (4.8), and noting that for $j = 1, ..., N$, we have

$$U_j'(x) = \int_{-\pi}^{\pi} \frac{\mathrm{d}}{\mathrm{d}x} w_{jj}(x-y) f(U_j(y)) \mathrm{d}y = \int_{-\pi}^{\pi} w_{jj}(x-y) f'(U_j(y)) U_j'(y) \mathrm{d}y.$$

Therefore, if we set $\varphi_j(x) = f'(U_j(x))U_j'(x)$ for a *single index* $j = 1, ..., M$ and $\varphi_l(x) \equiv 0$ otherwise, then for that index j, Eq. (4.42) becomes

$$\begin{aligned} f'(U_j(x))U_j'(x) &= f'(U_j(x)) \left[w_{jj}(x) * \left[f'(U_j(x))U_j'(x) \right] + \sum_{k=M+1}^{N} w_{kj}(x) * (0) \right] \\ &= f'(U_j(x))U_j'(x), \end{aligned}$$

and for $l \neq j$, we have

$$0 = f'(U_l(x)) \left[w_{ll}(x) * [0] + \sum_{k \neq l;\ k=M+1}^{N} w_{kl}(x) * (0) \right] = 0.$$

Thus, taking the inner product of Eq. (4.41) with each function in this M-dimensional set of nullspace vectors, we have a closed system of independent-evolution equations for the set of phases $(\Delta_1, ..., \Delta_M)$:

$$\mathrm{d}\Delta_j = \left[q_j(\Delta_j) + \varepsilon v(t)\right] \mathrm{d}t + \mathrm{d}\mathcal{Z}_t^j, \quad j = 1, ..., M, \tag{4.43}$$

where now $\langle \left(\mathcal{Z}_t^j\right)^2 \rangle = D_{jj}t$ with

$$q_j(\Delta_j) = \varepsilon \frac{\int_{-\pi}^{\pi} f'(U_j(x))U_j'(x) \int_{-\pi}^{\pi} h_j(y+\Delta_j) w_{jj}(x-y) f(U_j(y)) \mathrm{d}y \mathrm{d}x}{\int_{-\pi}^{\pi} f'(U_j(x))U_j'(x)^2 \mathrm{d}x},$$

$$D_{jj} = \varepsilon^2 \frac{\int_{-\pi}^{\pi} \int_{-\pi}^{\pi} f'(U_j(x))U_j'(x) f'(U_j(y))U_j'(y) C_{jj}(x-y) \mathrm{d}y \mathrm{d}x}{\left[\int_{-\pi}^{\pi} f'(U_j(x))U_j'(x)^2 \mathrm{d}x\right]^2}.$$

Lastly, to express the phases $(\Delta_{M+1}, ..., \Delta_N)$ in terms of $(\Delta_1, ..., \Delta_M)$, we apply the eigenvalue equation, Eq. (4.20), we derived in Section 4.2.2. The possible equilibrium positions $(\Delta_1, ..., \Delta_N)$ of bumps can be approximated by assuming a zero eigenvalue $\lambda = 0$ in Eq. (4.20) and taking inner products with $f'(U_j(x))U_j'(x)$ for $j = 1, ..., N$:

$$\begin{aligned} \Delta_j \langle f'(U_j)U_j', U_j' \rangle &= \left\langle f'(U_j)U_j', \sum_{k=1}^{N} w_{jk} * \left[f'(U_k)U_k'\right] \Delta_k \right\rangle, \\ 0 &= \left\langle f'(U_j)U_j', \sum_{k=1}^{N} w_{jk} * \left[f'(U_k)U_k'\right] \cdot \left[\Delta_k - \Delta_j\right] \right\rangle. \end{aligned} \tag{4.44}$$

It can be shown Eq. (4.44) is immediately satisfied for $j = 1, ..., M$, since $w_{jk}(x) \equiv 0$ for $k \neq j$. The remaining $(N - M)$-dimensional system for $(\Delta_{M+1}, ..., \Delta_N)$ can then be solved algebraically. As the independent phases $(\Delta_1, ..., \Delta_M)$ determine the dynamics, we ignore the local impact of noise in the non-independent layers $(\Delta_{M+1}, ..., \Delta_N)$. We now demonstrate this calculation for a 3-layer model with two independent layers ($j = 1, 2$).

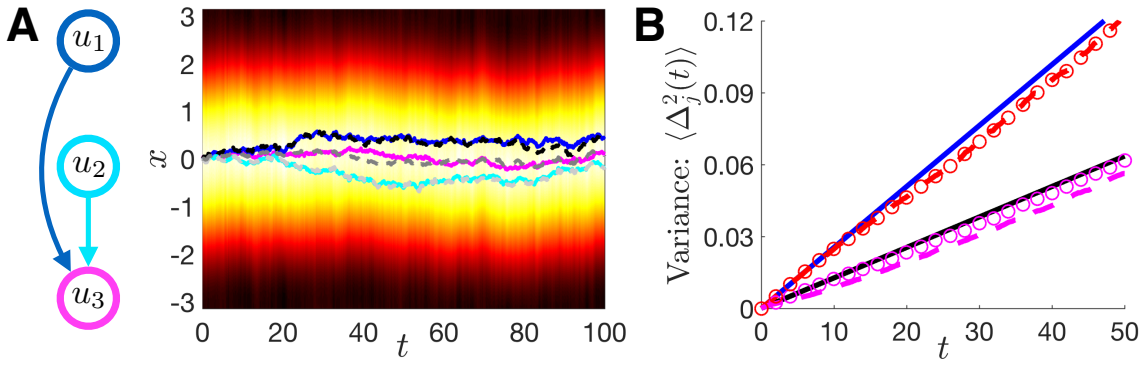

Figure 4.9: Evolution of bump positions in a $N = 3$-layer network with only feedforward connectivity from $1 \mapsto 3$ and $2 \mapsto 3$, so layers 1 and 2 evolve independently. (**A**) Numerical simulation of bump evolution in layer 3 overlaid with bump position from full simulation (magenta line), as well as positions of the bumps in layer 1 (dark blue) and layer 2 (cyan). Dashed lines are approximations from low-dimensional system, Eq. (4.43). (**B**) Variance $\langle \Delta_j^2(t) \rangle$ as a function of time as computed from full numerical simulations (dashed lines), the low-dimensional approximation (circles), and the effective diffusion calculation (solid lines), Eq. (4.39). The top curves are for layer 1 ($\langle \Delta_1^2(t) \rangle$) and the bottom curves are for layer 3 ($\langle \Delta_3^2(t) \rangle$), the output layer. While this is a fully feedforward network, the output layer averages the position estimates in layers 1 and 2, reducing the effective diffusion of the layer 3 bump. Here $h_1(x) = h_2(x) = 0.25\cos(8x)$ and $h_3(x) \equiv 0$ with interlaminar connectivity $\bar{w}_{31} = \bar{w}_{32} = 0.3$, and $\varepsilon = 0.1$. Numerical simulations are performed as described in Fig. 4.7.

Three-layer imploding star. We begin by assuming the constituent functions take the form $w_{jj}(x) = \cos(x)$ $(j = 1, .., 3)$; $h_j(x) = \sigma\cos(n_j x)$ $(j = 1, 2)$; $w_{3j}(x) = \bar{w}_c(1 + \cos(x))/2$ $(j = 1, 2)$; and $C_{jj}(x) = \pi\cos(x)$. In this case, the function $q_j(\Delta_j) = -\mathcal{C}_j \sin(n_j\Delta_j)/(2\sin(a))$ and $D_{jj} = \pi\varepsilon^2/(4\sin^2(a))$ $(j = 1, 2)$ in Eq. (4.43), with $\mathcal{C}_j$ defined as in Eq. (4.38). Note that $a_1 = a_2 = a$, but $a_3 \neq a$, due to synaptic input from layers 1 and 2. Thus, using Eq. (4.44), we can solve to find that $\Delta_3(t) = (\Delta_1(t) + \Delta_2(t))/2$, so $\langle \Delta_3^2(t) \rangle = \left[\langle \Delta_1^2(t) \rangle + \langle \Delta_2^2(t) \rangle\right]/4$. Both the low-dimensional approximation, Eq. (4.43), and the resulting variances compare well with our results from numerical simulation (Fig. 4.9). Also, even though there

is no recurrence in this network, the fact that the output layer 3 receives two independent feedforward inputs means its estimate will be a weighted average of layers 1 and 2. Ultimately, this leads to more robust storage of the initial condition of the network in the output layer.

4.5 Conclusion

We have carried out a detailed analysis of the stochastic dynamics of bumps in multilayer neural fields. Importantly, the model incorporated both spatial heterogeneities and velocity inputs, to understand how these network features interacted with noise. In the absence of velocity input, we have shown that a bump's response to perturbations is shaped by the graph of the interlaminar architecture. Bumps in layers of the network that receive no feedback from other layers will not be affected by perturbations to the rest of the network. This lack of feedback to independent layers means that such feedforward networks are less robust to noise perturbations, since noise cancelation relies upon the presence of recurrent architecture [86]. Recurrently coupled networks are more robust to noise perturbations, especially when layers possess heterogeneity. The most severe heterogeneities will tend to determine the stability of the entire network's bump solution in the presence of noise. However, the stabilizing effect of heterogeneities is disruptive to velocity integration, since it slows the propagation of velocity-driven bumps. Interestingly, noise can restore the propagation of bumps, so they move at a speed close to the input. We also extended this analysis to the case of networks with

multiple independent layers, showing multiple phase variables are needed to describe each independent layer's bump. The non-independent layers are entrained by the phases of the independent layers. Our work extends previous results on the impact of noise [19], heterogeneity [17], and velocity input [168] on the dynamics of continuum neural fields, to address how multilayer architectures shape networks' processing of spatially-relevant inputs.

Chapter 5

Discussion

Our primary motivation for exploring these models comes from extensive experimental literature on persistent activity representing spatial working memory [65, 107]. Particularly pertinent to this work are place cell and grid cell networks, which track a mammal's idiothetic position in two-dimensional space as it navigates through its environment [109]. Networks in cortex and hippocampus are capable of encoding analog spatial variables for time periods lasting seconds up to tens of minutes on length scales of hundreds of meters [73]. The specific single neuron and network architectural features that engender this impressive accuracy are the subject of ongoing research [30].

We have introduced and studied a neural field model that incorporates external inputs and additive noise as a model of short term memory in mammals. In networks with no spatial heterogeneity, noise causes bumps to wander according to Brownian motion. In the presence of spatially heterogeneous external inputs,

the stochastic bumps no longer obey dynamics well described by pure diffusion. Rather, bumps are attracted to the local maxima of the input functions, so their motion can be approximated by multivariate Ornstein-Uhlenbeck processes. In Chapter 3, we include a velocity input that results in the propagation of the bump attractor, whose position encodes an animal's estimate of its position. Noise can cause degradation in the memory, which can cause inaccurate memory recollection. We proposed a novel addition to the model that incorporates the effects of sensory feedback assuming the distance between an animal's perceived and actual position is relatively small.

Finally, in Chapter 4, we showed our analysis need not be limited to a single network layer. Importantly, the model incorporated both spatial heterogeneities and velocity inputs, to understand how these network features interacted with noise. In the absence of velocity input, we have shown that a bump's response to perturbations is shaped by the graph of the interlaminar architecture. Recurrently coupled networks are more robust to noise perturbations, especially when layers possess heterogeneity. The most severe heterogeneities will tend to determine the stability of the entire network's bump solution in the presence of noise. However, the stabilizing effect of heterogeneities is disruptive to velocity integration, since it slows the propagation of velocity-driven bumps. Interestingly, noise can restore the propagation of bumps, so they move at a speed close to the input. We also extended this analysis to the case of networks with multiple independent layers, showing multiple phase variables are needed to describe each independent layer's bump.

We note there is also evidence that place cell networks can respond to abrupt and large changes in an animal's spatial context [157]. In a study by [83], when an animal's spatial reference frame was suddenly switched, network activity could rapidly adjust to reflect the new context. In some trials, activity flickered between the two possible environment representations before settling on the new contextual representation. We could extend our model to account for these observations, by exploring the effects of large and strong sensory feedback cues, which could lead to such winner-take-all dynamics [87, 135]. There is also recent experimental evidence for discrete, rather than continuous, representations of spatial position by navigational networks. Studying the dynamics of sharp-wave ripple events in hippocampus, [115] showed that reactivation sequences had activity reflecting discrete attractors of the underlying network. Rather than evolving smoothly, neural activity would temporarily sharpen in the vicinity of each position-representing attractor before transitioning to a spatially discontiguous location. In this paradigm, theta-frequency or gamma-frequency oscillations of inhibitory input could temporarily destabilize attractors, allowing neural activity to traverse the network to subsequent attractors [78, 155]. It would be interesting to consider such modifications to our model and explore how they impact the robustness of the spatial-position code.

It is important to note that synaptic connections projecting from long-range axons can be subject to axonal transmission delays, as in the planar neural field study of Hutt and Rougier [81] and in multi-layer ring models [88]. For simplicity in our analysis, we only considered instantaneous synaptic connections. In future

work, we could explore the impact of delays within and between layers of neural fields when velocity is non-zero. As shown on stationary one-dimensional bump attractor systems [88], delay tends to stabilize the position of bumps to noise. We suspect a similar result, wherein diffusion is reduced. However, delay may also impact the network's ability to accurately integrate velocity. It would be interesting to derive the underlying dynamics when delay is included.

Finally, we believe our network analysis could be extended to derive the effective dynamics of more general neural activity. In particular, we expect that similar analyses could be performed on neural fields that support traveling waves [116] or Turing patterns [43]. It would be interesting to examine layers that individually support Turing patterns with different dominant frequencies, to see how interlaminar coupling impacts the onset of pattern-formation and the frequency of the emerging pattern. We are also interested in extending this framework to multilayer networks whose individual layers support different classes of solution. For example, we could consider a network comprised of two layers wherein one layer supports bump attractors and the other supports stationary front solutions. In the case of excitatory feedforward input from the bump to the front layer, the front would expand only in response to the motion of the bump. Such a network could provide robust storage of visited locations during memory-guided visual search [36] or spatial navigation [68].

Appendix A

Two Ring Reduction Analysis

In Eq. (4.1) and in previous work [118], we present a model with a spatially asymmetric-weight function whose amplitude represents velocity input. Varying this input leads to a proportional rise in the velocity of moving bumps generated in the corresponding network. This single-layer network is a linear reduction of a "double-ring" network, analyzed in detail in [164]. Originally developed as a model of the head-direction system, the rings of the double-ring network each prefer either rightward or leftward velocity inputs. However, similar network architectures have been used to model the dynamics of activity in the brain's spatial navigation system [30], as we consider here. We now demonstrate a reduction of the double-ring network to a single-ring network where inputs are given as a pre-factor to an integral term with asymmetric coupling, as in [118]. In Section B, we show how this reduction extends to a two-layer network, where each layer is a reduction of a "double-ring."

We consider a slight variation on the model used in [164], so the nonlinearity filtering synaptic input is within, rather than outside, the convolution integrals. Note, it is typically possible to perform a mapping between such models [19]. In a double-ring model, there are two synaptic input variables $u_L(x,t)$ and $u_R(x,t)$, for leftward and rightward preferring velocity populations respectively, subject to the evolution equations

$$\frac{\partial u_L}{\partial t} = -u_L + w_{+\phi} * f(u_L(x,t)) + w_{-\phi} * f(u_R(x,t)) + I(t), \tag{A.1a}$$

$$\frac{\partial u_R}{\partial t} = -u_R + w_{+\phi} * f(u_L(x,t)) + w_{-\phi} * f(u_R(x,t)) - I(t), \tag{A.1b}$$

where the nonzero shift $\phi > 0$ in either weight function $w_{\pm\phi} := w(x \pm \phi)$ is crucial for generating traveling bumps in the input driven system ($I(t) \neq 0$). Note that the function $w(x) = w(-x)$ is a typical even-symmetric, lateral-inhibitory weight kernel, as described in Section 4.1. Symmetric, stationary bump solutions $u_{L,R}(x,t) = U(x)$ to Eq. (A.1) are given by the equation:

$$U(x) = \bar{w}(x) * f(U(x)), \quad \bar{w}(x) = w(x+\phi) + w(x-\phi), \tag{A.2}$$

where $\bar{w}(x)$ is an even symmetric function, since $\bar{w}(-x) = w(-x+\phi) + w(-x-\phi) = w(x-\phi) + w(x+\phi) = \bar{w}(x)$. Input $I \neq 0$ is converted to bump velocity, which can be demonstrated by assuming $|I(t)| \ll 1$ and linearizing Eq. (A.1) using the ansatz, $u_j(x,t) = U(x - X(t) - \psi_j) + \varepsilon\Phi_j(x,t) + \mathcal{O}(\varepsilon^2)$ ($j = L, R$):

$$\frac{\partial}{\partial t}\begin{pmatrix} \Phi_L(x,t) \\ \Phi_R(x,t) \end{pmatrix} = \mathcal{L}\begin{pmatrix} \Phi_L(x,t) \\ \Phi_R(x,t) \end{pmatrix} + \begin{pmatrix} \varepsilon v(t) U'(x) + I(t) \\ \varepsilon v(t) U'(x) - I(t) \end{pmatrix}, \tag{A.3}$$

where $\varepsilon v(t) = \dot{X}(t)$ is the bump's velocity, and the linear operator

$$\mathcal{L}\begin{pmatrix}\Phi_L\\ \Phi_R\end{pmatrix} = \begin{pmatrix}-\Phi_L + w_{+\phi} * [f'(U)\Phi_L] + w_{-\phi} * [f'(U)\Phi_R]\\ -\Phi_R + w_{+\phi} * [f'(U)\Phi_L] + w_{-\phi} * [f'(U)\Phi_R]\end{pmatrix}.$$

For solutions to Eq. (A.3) to be bounded, we require the inhomogeneous portion to be orthogonal to the nullspace of the adjoint linear operator, defined as

$$\mathcal{L}^*\begin{pmatrix}\Psi_L\\ \Psi_R\end{pmatrix} = \begin{pmatrix}-\Psi_L + f'(U)\cdot w_{+\phi} * [\Psi_L + \Psi_R]\\ -\Psi_R + f'(U)\cdot w_{-\phi} * [\Psi_L + \Psi_R]\end{pmatrix} \equiv \begin{pmatrix}0\\ 0\end{pmatrix}.$$

This leads to the following equation for the dependence of the bumps' velocity $\varepsilon v(t)$ on the input $I(t)$:

$$\varepsilon v(t) = \frac{\langle I(t), \Psi_L(x) - \Psi_R(x)\rangle}{\langle U'(x), \Psi_L(x) + \Psi_R(x)\rangle}.$$

Thus, there is a proportional increase in the velocity $\varepsilon v(t)$ corresponding to an increase in the input $I(t)$, to linear order. By differentiating Eq. (A.2), we see a solution to Eq. (A.3) is $\Phi_{L,R}(x,t) = U'(x)$. Thus, up to $\mathcal{O}(\varepsilon^2)$, we can approximate $u_{L,R}(x,t) \approx U(x - X(t) - \psi_{L,R})$. Dropping subscripts on the u_j ($j = L, R$) formulae and differentiating with respect to t, we find

$$\frac{\partial u(x,t)}{\partial t} = -\varepsilon v(t) U'(x - X(t) + \psi), \tag{A.4}$$

and we can further incorporate the formula for the stationary bump by replacing $U(x - X(t) - \psi)$ with $u(x,t)$ in Eq. (A.2), and adding the equation to Eq. (A.4). Subsequently, a differentiation of that formula, with $U(x - X(t) - \psi)$ replaced with $u(x,t)$ means the $U'(x - X(t) - \psi)$ in Eq. (A.4) can also be replaced to yield

$$\frac{\partial u(x,t)}{\partial t} = -u + \bar{w} * f(u) - \varepsilon v(t)\left[\bar{w}'\right] * f(u), \tag{A.5}$$

so Eq. (A.5) describes the dynamics of Eq. (A.1) to linear order in $I(t)$.

Appendix B

Reduction in Multiple Dimensions

The double-ring model, Eq. (A.1), can be extended to the case of two layers (of double-rings), each receiving independent velocity-producing inputs. Now, there are four synaptic input variables ($u_{L1}, u_{R1}, u_{L2}, u_{R2}$), where u_{jk} corresponds to the variable in the kth layer preferring j (L : left or R : right)-ward velocity. These are subject to the evolution equations

$$\dot{u}_{L1} = -u_{L1} + w_{+\phi} * [f(u_{L1}) + \alpha_c f(u_{L2})] + w_{-\phi} * [f(u_{R1}) + \alpha_c f(u_{R2})] + I, \quad \text{(B.1)}$$

$$\dot{u}_{R1} = -u_{R1} + w_{+\phi} * [f(u_{L1}) + \alpha_c f(u_{L2})] + w_{-\phi} * [f(u_{R1}) + \alpha_c f(u_{R2})] - I,$$

$$\dot{u}_{L2} = -u_{L2} + w_{+\phi} * [f(u_{L2}) + \alpha_c f(u_{L1})] + w_{-\phi} * [f(u_{R2}) + \alpha_c f(u_{R1})] + I,$$

$$\dot{u}_{R2} = -u_{R2} + w_{+\phi} * [f(u_{L2}) + \alpha_c f(u_{L1})] + w_{-\phi} * [f(u_{R2}) + \alpha_c f(u_{R1})] - I,$$

where again the nonzero shift $\phi > 0$ causes bumps to travel when $I \neq 0$, and α_c represents the coupling between layers 1 and 2. Since $w(x) = w(-x)$ is even, there are symmetric, stationary bump solutions $u_{jk}(x,t) = U(x)$ ($j = L, R$, $k = 1, 2$) to

Eq. (B.1), given by:

$$U(x) = (1 + \alpha_c)\bar{w}(x) * f(U(x)), \quad \bar{w}(x) = w(x + \phi) + w(x - \phi), \tag{B.2}$$

and note $\bar{w}(x)$ is even. When $|I(t)| \ll 1$, we linearize Eq. (B.1) assuming $u_{jk}(x,t) = U(x - X(t) - \psi_{jk}) + \varepsilon\Phi_{jk}(x,t) + \mathcal{O}(\varepsilon^2)$ for $j = L, R$ and $k = 1, 2$:

$$\left(\frac{\partial}{\partial t} - \mathcal{L}\right)\begin{pmatrix} \Phi_{L1}(x,t) \\ \Phi_{R1}(x,t) \\ \Phi_{L2}(x,t) \\ \Phi_{R2}(x,t) \end{pmatrix} = \begin{pmatrix} \varepsilon v(t)U'(x) + I(t) \\ \varepsilon v(t)U'(x) - I(t) \\ \varepsilon v(t)U'(x) + I(t) \\ \varepsilon v(t)U'(x) - I(t) \end{pmatrix}, \tag{B.3}$$

where $\varepsilon v(t) = \dot{X}(t)$ is the bumps' velocity, and the linear operator

$$\mathcal{L}(\mathbf{\Phi}) = -\mathbf{\Phi} + \begin{pmatrix} w_{+\phi} * [f'(U)(\Phi_{L1} + \alpha_c\Phi_{L2})] + w_{-\phi} * [f'(U)(\Phi_{R1} + \alpha_c\Phi_{R2})] \\ w_{+\phi} * [f'(U)(\Phi_{L1} + \alpha_c\Phi_{L2})] + w_{-\phi} * [f'(U)(\Phi_{R1} + \alpha_c\Phi_{R2})] \\ w_{+\phi} * [f'(U)(\Phi_{L2} + \alpha_c\Phi_{L1})] + w_{-\phi} * [f'(U)(\Phi_{R2} + \alpha_c\Phi_{R1})] \\ w_{+\phi} * [f'(U)(\Phi_{L2} + \alpha_c\Phi_{L1})] + w_{-\phi} * [f'(U)(\Phi_{R2} + \alpha_c\Phi_{R1})] \end{pmatrix}$$

where $\mathbf{\Phi} = (\Phi_{L1}, \Phi_{R1}, \Phi_{L2}, \Phi_{R2})$. For solutions to Eq. (B.3) to be bounded, we require the right hand side to be orthogonal to the nullspace of $\mathcal{L}^*$, defined:

$$\mathcal{L}^*(\mathbf{\Psi}) = -\mathbf{\Psi} + \begin{pmatrix} f'(U) \cdot w_{+\phi} * [\Psi_{L1} + \Psi_{R1} + \alpha_c(\Psi_{L2} + \Psi_{R2})] \\ f'(U) \cdot w_{-\phi} * [\Psi_{L1} + \Psi_{R1} + \alpha_c(\Psi_{L2} + \Psi_{R2})] \\ f'(U) \cdot w_{+\phi} * [\Psi_{L2} + \Psi_{R2} + \alpha_c(\Psi_{L1} + \Psi_{R1})] \\ f'(U) \cdot w_{-\phi} * [\Psi_{L2} + \Psi_{R2} + \alpha_c(\Psi_{L1} + \Psi_{R1})] \end{pmatrix} \equiv 0.$$

with $\mathbf{\Psi} = (\Psi_{L1}, \Psi_{R1}, \Psi_{L2}, \Psi_{R2})$. This leads to the following linear equation, relating $\varepsilon v(t)$ to $I(t)$:

$$\varepsilon v(t) = \frac{\langle I(t), \Psi_{L1}(x) + \Psi_{L2}(x) - \Psi_{R1}(x) - \Psi_{R2}(x)\rangle}{\langle U'(x), \Psi_{L1}(x) + \Psi_{L2}(x) + \Psi_{R1}(x) + \Psi_{R2}(x)\rangle}.$$

Lastly, noting $\Phi_{jk}(x,t) = U'(x)$ solves Eq. (B.3), we can approximate $u_{jk} \approx U(x - X(t) - \psi_{jk})$ ($j = L, R$ and $k = 1, 2$) up to $\mathcal{O}(\varepsilon^2)$. Dropping the subscripts and differentiating with respect to t, we again find Eq. (A.4). Next, replacing $U(x - X(t) - \psi)$ with $u(x,t)$ in Eq. (B.2) and adding to Eq. (A.4) as well as plugging this equation in for $U'(x - X(t) - \psi)$ yields

$$\frac{\partial u(x,t)}{\partial t} = -u + (1 + \alpha_c)\bar{w} * f(u) - \varepsilon v(t)(1 + \alpha_c)\left[\bar{w}'\right] * f(u). \tag{B.4}$$

Note, in the case of asymmetric coupling between either double ring, we would expect two distinct forms of Eq. (B.4), where $\bar{w}'$ was different for either. This full asymmetry for an arbitrary number of layers is captured by the asymmetric-weight functions given by Eqs. (4.1) and (4.5).

Bibliography

[1] A. Abbott. Brains of norway. *Nature*, 514(7521):154–157, 2014.

[2] D. Aikath, A.P. Weible, D.C. Rowland, and C.G. Kentros. Role of self-generated odor cues in contextual representation. *Hippocampus*, 24(8):1039–51, 2014.

[3] E. Aksay, G. Gamkrelidze, S.H. Seung, R. Baker, and D.W. Tank. In vivo intracellular recording and perturbation of persistent activity in a neural integrator. *Nature Neuroscience*, 4(2):184–193, 2001.

[4] S. Amari. Dynamics of pattern formation in lateral-inhibition type neural fields. *Biological Cybernetics*, 27(2):77–87, 1977.

[5] S. Amari. *Mathematical theory of nerve nets*. Sangyotosho, 1978.

[6] S. Amari. Heaviside world: Excitation and self-organization of neural fields. In Stephen Coombes, Peter beim Graben, Roland Potthast, and James Wright, editors, *Neural Fields: Theory and Applications*. Springer, 2014.

[7] M.I. Anderson and K.J. Jeffery. Heterogeneous modulation of place cell firing by changes in context. *The Journal of Neuroscience*, 23(26):8827–8835, 2003.

[8] G. Anello and G. Cordaro. Existence of solutions and bifurcation points to hammerstein equations with essentially bounded kernel. *Journal of Mathematical Analysis and Applications*, 298(1):292–297, 2004.

[9] J. Armero, J. Casademunt, L. Ramirez-Piscina, and J.M. Sancho. Ballistic and diffusive corrections to front propagation in the presence of multiplicative noise. *Physical Review E*, 58(5):5494, 1998.

[10] K. Atkinson. *A survey of numerical methods for the solution of Fredholm Integral Equations of the Second Kind*. SIAM, 1976.

[11] A. Baddeley. Working memory: looking back and looking forward. *Nature Reviews Neuroscience*, 4(10):829–839, 2003.

[12] F.P. Battaglia, G.R. Sutherland, and B.L. McNaughton. Local sensory cues and place cell directionality: additional evidence of prospective coding in the hippocampus. *The Journal of Neuroscience*, 24(19):4541–4550, 2004.

[13] P.M. Bays. Spikes not slots: noise in neural populations limits working memory. *Trends in Cognitive Sciences*, 19(8):431–438, 2015.

[14] R. Ben-Yishai, R.L. Bar-Or, and H. Sompolinsky. Theory of orientation tuning in visual cortex. *Proceedings of the National Academy of Sciences*, 92(9):3844–8, 1995.

[15] M. Benayoun, J.D. Cowan, W. van Drongelen, and E. Wallace. Avalanches in a stochastic model of spiking neurons. *PLoS Computational Biology*, 6(7):e1000846, 2010.

[16] C.A. Brackley and M.S. Turner. Random fluctuations of the firing rate function in a continuum neural field model. *Physical Review E*, 75(4 Pt 1):041913, 2007.

[17] P.C. Bressloff. Traveling fronts and wave propagation failure in an inhomogeneous neural network. *Physica D: Nonlinear Phenomena*, 155(1):83–100, 2001.

[18] P.C. Bressloff. Stochastic neural field theory and the system-size expansion. *SIAM Journal on Applied Mathematics*, 70(5):1488–1521, 2009.

[19] P.C. Bressloff. Spatiotemporal dynamics of continuum neural fields. *Journal of Physics A: Mathematical and Theoretical*, 45(3):033001, 2011.

[20] P.C. Bressloff. Neural field model of binocular rivalry waves. In *Waves in Neural Media*, pages 319–345. Springer, 2014.

[21] P.C. Bressloff and S. Coombes. Neural 'bubble' dynamics revisited. *Cognitive Computation*, 5(3):281–294, 2013.

[22] P.C. Bressloff and J.D. Cowan. A spherical model for orientation and spatial–frequency tuning in a cortical hypercolumn. *Philosophical Transactions of the Royal Society of London. Series B: Biological Sciences*, 358(1438):1643–1667, 2003.

[23] P.C. Bressloff and Z.P. Kilpatrick. Two-dimensional bumps in piecewise smooth neural fields with synaptic depression. *SIAM Journal on Applied Mathematics*, 71(2):379–408, 2011.

[24] P.C Bressloff and Z.P. Kilpatrick. Nonlinear langevin equations for wandering patterns in stochastic neural fields. *SIAM Journal on Applied Dynamical Systems*, 14(1):305–334, 2015.

[25] P.C. Bressloff and M.A. Webber. Front propagation in stochastic neural fields. *SIAM Journal on Applied Dynamical Systems*, 11(2):708–740, 2012.

[26] C.D. Brody, R. Romo, and A. Kepecs. Basic mechanisms for graded persistent activity: discrete attractors, continuous attractors, and dynamic representations. *Current Opinion in Neurobiology*, 13(2):204–211, 2003.

[27] V.H. Brun, T. Solstad, K.B. Kjelstrup, M. Fyhn, M.P. Witter, E.I. Moser, and M. Moser. Progressive increase in grid scale from dorsal to ventral medial entorhinal cortex. *Hippocampus*, 18(12):1200–1212, 2008.

[28] N. Brunel and V. Hakim. Fast global oscillations in networks of integrate-and-fire neurons with low firing rates. *Neural Computation*, 11(7):1621–1671, 1999.

[29] Y. Burak and I.R. Fiete. Grid cells: the position code, neural network models of activity, and the problem of learning. *Hippocampus*, 18:1283–1300, 2008.

[30] Y. Burak and I.R. Fiete. Accurate path integration in continuous attractor

network models of grid cells. *PLoS Computational Biology*, 5(2):e1000291, 2009.

[31] Y. Burak and I.R. Fiete. Fundamental limits on persistent activity in networks of noisy neurons. *Proceedings of the National Academy of Sciences*, 109(43):17645–50, 2012.

[32] N. Burgess, E.A. Maguire, and J. O'Keefe. The human hippocampus and spatial and episodic memory. *Neuron*, 35(4):625–641, 2002.

[33] G. Buzsáki and E.I. Moser. Memory, navigation and theta rhythm in the hippocampal-entorhinal system. *Nature Neuroscience*, 16(2):130–138, 2013.

[34] M. Camperi and X. Wang. A model of visuospatial working memory in prefrontal cortex: recurrent network and cellular bistability. *Journal of Computational Neuroscience*, 5(4):383–405, 1998.

[35] S. Carroll, K. Josić, and Z.P. Kilpatrick. Encoding certainty in bump attractors. *Journal of Computational Neuroscience*, 37(1):29–48, 2014.

[36] L. Chelazzi, J. Duncan, E.K. Miller, and R. Desimone. Responses of neurons in inferior temporal cortex during memory-guided visual search. *Journal of Neurophysiology*, 80(6):2918–2940, 1998.

[37] C.C. Chow and J.A. White. Spontaneous action potentials due to channel fluctuations. *Biophysical Journal*, 71(6):3013, 1996.

[38] W.W. Cochran, H. Mouritsen, and M. Wikelski. Migrating songbirds

recalibrate their magnetic compass daily from twilight cues. *Science*, 304(5669):405–408, 2004.

[39] T.S. Collett and P. Graham. Animal navigation: path integration, visual landmarks and cognitive maps. *Current Biology*, 14(12):R475–R477, 2004.

[40] A. Compte, N. Brunel, P.S. Goldman-Rakic, and X. Wang. Synaptic mechanisms and network dynamics underlying spatial working memory in a cortical network model. *Cerebral Cortex*, 10(9):910–923, 2000.

[41] C. Constantinidis and T. Klingberg. The neuroscience of working memory capacity and training. *Nature Reviews Neuroscience*, 17:438–449, 2016.

[42] C. Constantinidis and X. Wang. A neural circuit basis for spatial working memory. *The Neuroscientist*, 10(6):553–565, 2004.

[43] S. Coombes. Waves, bumps, and patterns in neural field theories. *Biological Cybernetics*, 93(2):91–108, 2005.

[44] S. Coombes and C.R. Laing. Pulsating fronts in periodically modulated neural field models. *Physical Review E*, 83(1):011912, 2011.

[45] S. Coombes and M. Owen. Evans functions for integral neural field equations with heaviside firing rate function. *SIAM Journal on Applied Dynamical Systems*, 3(4):574–600, 2004.

[46] S. Coombes and M. Owen. Bumps, breathers, and waves in a neural network with spike frequency adaptation. *Physical Review Letters*, 94(14):148102, 2005.

[47] S. Coombes and M. Owen. Exotic dynamics in a firing rate model of neural tissue with threshold accommodation. In F Botelho, T Hagen, and J E Jamison, editors, *Fluids and Waves: Recent Trends in Applied Analysis*, volume 440, pages 123–144. American Mathematical Society: Contemporary Mathematics, 2007.

[48] S. Coombes, H. Schmidt, and I. Bojak. Interface dynamics in planar neural field models. *Journal of Mathematical Neuroscience*, 2(1):9, 2012.

[49] T.M. Cover and J.A. Thomas. *Elements of information theory*. Wiley-interscience, 2006.

[50] C.E. Curtis. Prefrontal and parietal contributions to spatial working memory. *Neuroscience*, 139(1):173–180, 2006.

[51] S. Deneve, P.E. Latham, and A. Pouget. Reading population codes: a neural implementation of ideal observers. *Nature Neuroscience*, 2(8):740–745, 1999.

[52] S.S. Deshmukh and J.J. Knierim. Representation of non-spatial and spatial information in the lateral entorhinal cortex. *Frontiers in Behavioral Neuroscience*, 5:69, 2011.

[53] A. Destexhe and D. Contreras. Neuronal computations with stochastic network states. *Science*, 314(5796):85–90, 2006.

[54] D. Durstewitz, J.K. Seamans, and T.J. Sejnowski. Neurocomputational models of working memory. *Nature Neuroscience*, 3:1184–1191, 2000.

[55] B. Ermentrout. Neural networks as spatio-temporal pattern-forming systems. *Reports on Progress in Physics*, 61(4):353, 1998.

[56] A.S. Etienne, R. Maurer, and V. Séguinot. Path integration in mammals and its interaction with visual landmarks. *The Journal of Experimental Biology*, 199(1):201–209, 1996.

[57] A.A. Faisal, L.P.J. Selen, and D.M. Wolpert. Noise in the nervous system. *Nature Reviews Neuroscience*, 9(4):292–303, 2008.

[58] O. Faugeras and J. Inglis. Stochastic neural field equations: A rigorous footing. *Journal of Mathematical Biology*, 71(2):1–42, 2013.

[59] O. Faugeras, R. Veltz, and F. Grimbert. Persistent neural states: stationary localized activity patterns in nonlinear continuous n-population, q-dimensional neural networks. *Neural Computation*, 21(1):147–187, 2009.

[60] S.E. Folias and P.C. Bressloff. Breathing pulses in an excitatory neural network. *SIAM Journal on Applied Dynamical Systems*, 3(3):378–407, 2004.

[61] S.E. Folias and P.C. Bressloff. Breathers in two-dimensional neural media. *Physical Review Letters*, 95(20):208107, 2005.

[62] S.E. Folias and B. Ermentrout. New patterns of activity in a pair of interacting excitatory-inhibitory neural fields. *Physical Review Letters*, 107(22):228103, 2011.

[63] S.E. Folias and B. Ermentrout. Bifurcations of stationary solutions in an interacting pair of ei neural fields. *SIAM Journal on Applied Dynamical Systems*, 11(3):895–938, 2012.

[64] M.D. Fox and M.E. Raichle. Spontaneous fluctuations in brain activity observed with functional magnetic resonance imaging. *Nature Reviews Neuroscience*, 8(9):700–711, 2007.

[65] S. Funahashi, C.J. Bruce, and P.S. Goldman-Rakic. Mnemonic coding of visual space in the monkey's dorsolateral prefrontal cortex. *Journal of Neurophysiology*, 61(2):331–349, 1989.

[66] C.C.A. Fung, K.Y.M. Wong, and S. Wu. A moving bump in a continuous manifold: A comprehensive study of the tracking dynamics of continuous attractor neural networks. *Neural Computation*, 22(3):752–792, 2010.

[67] C.W. Gardiner. *Handbook of Stochastic Methods for Physics, Chemistry, and the Natural Sciences*. Springer-Verlag, Berlin, 3rd ed edition, 2004.

[68] M. Geva-Sagiv, L. Las, Y. Yovel, and N. Ulanovsky. Spatial cognition in bats and rats: from sensory acquisition to multiscale maps and navigation. *Nature Reviews Neuroscience*, 16(2):94–108, 2015.

[69] M.S. Goldman, J.H. Levine, G. Major, D.W. Tank, and H.S. Seung. Robust persistent neural activity in a model integrator with multiple hysteretic dendrites per neuron. *Cerebral Cortex*, 13(11):1185–1195, 2003.

[70] P.S. Goldman-Rakic. Cellular basis of working memory. *Neuron*, 14(3):477–485, 1995.

[71] Y. Guo. Existence and stability of traveling fronts in a lateral inhibition neural network. *SIAM Journal on Applied Dynamical Systems*, 11(4):1543–1582, 2012.

[72] Y. Guo and C.C. Chow. Existence and stability of standing pulses in neural networks: I. existence. *SIAM Journal on Applied Dynamical Systems*, 4(2):217–248, 2005.

[73] T. Hafting, M. Fyhn, S. Molden, M. Moser, and E.I. Moser. Microstructure of a spatial map in the entorhinal cortex. *Nature*, 436(7052):801–806, 2005.

[74] A. Hammerstein. Nichtlineare integralgleichungen nebst anwendungen. *Acta Mathematica*, 54(1):117–176, 1930.

[75] D. Hansel and G. Mato. Short-term plasticity explains irregular persistent activity in working memory tasks. *The Journal of Neuroscience*, 33(1):133–149, 2013.

[76] D. Hansel and H. Sompolinsky. Modeling feature selectivity in local cortical circuits. In C Koch and I Segev, editors, *Methods in Neuronal Modeling: From Ions to Networks*, chapter 13, pages 499–567. Cambridge: MIT, 1998.

[77] K. Hardcastle, S. Ganguli, and L.M. Giocomo. Environmental boundaries as an error correction mechanism for grid cells. *Neuron*, 86(3):827–39, 2015.

[78] M.E. Hasselmo and M.P. Brandon. A model combining oscillations and attractor dynamics for generation of grid cell firing. *Frontiers in Neural Circuits*, 6(30):1–12, 2012.

[79] J.V. Haxby, L. Petit, L.G. Ungerleider, and S.M. Courtney. Distinguishing the functional roles of multiple regions in distributed neural systems for visual working memory. *Neuroimage*, 11(2):145–156, 2000.

[80] A. Hutt, A. Longtin, and L. Schimansky-Geier. Additive noise-induced turing transitions in spatial systems with application to neural fields and the swift–hohenberg equation. *Physica D*, 237(6):755–773, 2008.

[81] A. Hutt and N.P. Rougier. Activity spread and breathers induced by finite transmission speeds in two-dimensional neural fields. *Physical Review E: Statistical, Nonlinear, and Soft Matter Physics*, 82:R055701, 2010.

[82] V. Itskov, D. Hansel, and M. Tsodyks. Short-term facilitation may stabilize parametric working memory trace. *Frontiers in Computational Neuroscience*, 5(40):1–19, 2011.

[83] K. Jezek, E.J. Henriksen, A. Treves, E.I. Moser, and M. Moser. Theta-paced flickering between place-cell maps in the hippocampus. *Nature*, 478(7368):246–249, 2011.

[84] S. Kastner, K. DeSimone, C.S. Konen, S.M. Szczepanski, K.S. Weiner, and K.A. Schneider. Topographic maps in human frontal cortex revealed in memory-guided saccade and spatial working-memory tasks. *Journal of Neurophysiology*, 97(5):3494–3507, 2007.

[85] S. Katzner, I. Nauhaus, A. Benucci, V. Bonin, D.L. Ringach, and M. Carandini. Local origin of field potentials in visual cortex. *Neuron*, 61(1):35–41, 2009.

[86] Z.P. Kilpatrick. Interareal coupling reduces encoding variability in multiarea models of spatial working memory. *Frontiers in Computational Neuroscience*, 7(82):1–14, 2013.

[87] Z.P. Kilpatrick. Short term synaptic depression improves information transfer in perceptual multistability. *Frontiers in Computational Neuroscience*, 7(85):53–68, 2013.

[88] Z.P. Kilpatrick. Delay stabilizes stochastic motion of bumps in layered neural fields. *Physica D: Nonlinear Phenomena*, 295:30–45, 2015.

[89] Z.P. Kilpatrick and P.C. Bressloff. Spatially structured oscillations in a two-dimensional excitatory neuronal network with synaptic depression. *Journal of Computational Neuroscience*, 28(2):193–209, 2010.

[90] Z.P. Kilpatrick and B. Ermentrout. Wandering bumps in stochastic neural fields. *SIAM Journal on Applied Dynamical Systems*, 12(1):61–94, 2013.

[91] Z.P. Kilpatrick, B. Ermentrout, and B. Doiron. Optimizing working memory with heterogeneity of recurrent cortical excitation. *The Journal of Neuroscience*, 33(48):18999–19011, 2013.

[92] Z.P. Kilpatrick, S.E. Folias, and P.C. Bressloff. Traveling pulses and wave

propagation failure in inhomogeneous neural media. *SIAM Journal on Applied Dynamical Systems*, 7(1):161–185, 2008.

[93] J.J. Knierim, H.S. Kudrimoti, and B.L. McNaughton. Place cells, head direction cells, and the learning of landmark stability. *The Journal of Neuroscience*, 15(3):1648–1659, 1995.

[94] J.J. Knierim and K. Zhang. Attractor dynamics of spatially correlated neural activity in the limbic system. *Annual Review of Neuroscience*, 35:267–285, 2012.

[95] H. Ko, S.B. Hofer, B. Pichler, K.A. Buchanan, P.J. Sjöström, and T.D. Mrsic-Flogel. Functional specificity of local synaptic connections in neocortical networks. *Nature*, 473(7345):87–91, 2011.

[96] A.A. Koulakov, S. Raghavachari, A. Kepecs, and J.E. Lisman. Model for a robust neural integrator. *Nature Neuroscience*, 5(8):775–782, 2002.

[97] J. Kruger and W. Stannat. Front propagation in stochastic neural fields: A rigorous mathematical framework. *SIAM Journal on Applied Dynamical Systems*, 13(3):1293–1310, 2014.

[98] C. Kuehn and M.G. Riedler. Large deviations for nonlocal stochastic neural fields. *Journal of Mathematical Neuroscience*, 4(1):1–33, 2014.

[99] C.R. Laing and C.C. Chow. Stationary bumps in networks of spiking neurons. *Neural Computation*, 13(7):1473–1494, 2001.

[100] C.R. Laing and A. Longtin. Noise-induced stabilization of bumps in systems with long-range spatial coupling. *Physica D*, 160(3-4):149 – 172, 2001.

[101] C.R. Laing and W.C. Troy. Pde methods for nonlocal models. *SIAM Journal on Applied Dynamical Systems*, 2(3):487–516, 2003.

[102] C.R. Laing, W.C. Troy, B. Gutkin, and B. Ermentrout. Multiple bumps in a neuronal model of working memory. *SIAM Journal on Applied Mathematics*, 63(1):62–97, 2002.

[103] I. Lee, D. Yoganarasimha, G. Rao, and J.J. Knierim. Comparison of population coherence of place cells in hippocampal subfields ca1 and ca3. *Nature*, 430(6998):456–459, 2004.

[104] S. Lim and M.S. Goldman. Balanced cortical microcircuitry for maintaining information in working memory. *Nature Neuroscience*, 16(9):1306–1314, 2013.

[105] B. Lindner, M. Kostur, and L. Schimansky-Geier. Optimal diffusive transport in a tilted periodic potential. *Fluctuation and Noise Letters*, 1(01):R25–R39, 2001.

[106] A. Longtin. Stochastic resonance in neuron models. *Journal of Statistical Physics*, 70(1-2):309–327, 1993.

[107] B.L. McNaughton, F.P. Battaglia, O. Jensen, E.I. Moser, and M. Moser. Path integration and the neural basis of the 'cognitive map'. *Nature Reviews Neuroscience*, 7(8):663–678, 2006.

[108] B.L. McNaughton, L. Chen, and E.J. Markus. "Dead reckoning," landmark learning, and the sense of direction: a neurophysiological and computational hypothesis. *Journal of Cognitive Neuroscience*, 3(2):190–202, 1991.

[109] E.I. Moser, E. Kropff, and M. Moser. Place cells, grid cells, and the brain's spatial representation system. *Annual Review of Neuroscience*, 31:69–89, 2008.

[110] W.J. O'brien, H.I. Browman, and B.I. Evans. Search strategies of foraging animals. *American Scientist*, 78(2):152–160, 1990.

[111] J. O'Keefe and N. Burgess. Geometric determinants of the place fields of hippocampal neurons. *Nature*, 381(6581):425–8, 1996.

[112] M.R. Owen, C.R. Laing, and S. Coombes. Bumps and rings in a two-dimensional neural field: splitting and rotational instabilities. *New Journal of Physics*, 9(10):378, 2007.

[113] D. Panja. Effects of fluctuations on propagating fronts. *Physics Reports*, 393(2):87–174, 2004.

[114] B. Pesaran, J.S. Pezaris, M. Sahani, P.P. Mitra, and R.A. Andersen. Temporal structure in neuronal activity during working memory in macaque parietal cortex. *Nature Neuroscience*, 5(8):805–811, 2002.

[115] B.E. Pfeiffer and D.J. Foster. Autoassociative dynamics in the generation of sequences of hippocampal place cells. *Science*, 349(6244):180–183, 2015.

[116] D.J. Pinto and B. Ermentrout. Spatially structured activity in synaptically

coupled neuronal networks: I. traveling fronts and pulses. *SIAM Journal on Applied Mathematics*, 62(1):206–225, 2001.

[117] D.B. Poll and Z.P. Kilpatrick. Stochastic motion of bumps in planar neural fields. *SIAM Journal on Applied Mathematics*, 75(4):1553–1577, 2015.

[118] D.B. Poll, K. Nguyen, and Z.P. Kilpatrick. Sensory feedback in a bump attractor model of path integration. *Journal of Computational Neuroscience*, 40(2):137–155, 2016.

[119] X. Qi, T. Meyer, T.R. Stanford, and C. Constantinidis. Changes in prefrontal neuronal activity after learning to perform a spatial working memory task. *Cerebral Cortex*, 21(12):2722–2732, 2011.

[120] S.G. Rao, G.V. Williams, and P.S. Goldman-Rakic. Isodirectional tuning of adjacent interneurons and pyramidal cells during working memory: evidence for microcolumnar organization in pfc. *Journal of Neurophysiology*, 81(4):1903–1916, 1999.

[121] A. Renart, N. Brunel, and X. Wang. Mean-field theory of irregularly spiking neuronal populations and working memory in recurrent cortical networks. In *Computational Neuroscience: A Comprehensive Approach*, pages 431–490. Boca Raton, CRC Press, 2004.

[122] A. Renart, P. Song, and X. Wang. Robust spatial working memory through homeostatic synaptic scaling in heterogeneous cortical networks. *Neuron*, 38(3):473–485, 2003.

[123] C. Ribrault, K. Sekimoto, and A. Triller. From the stochasticity of molecular processes to the variability of synaptic transmission. *Nature Reviews Neuroscience*, 12(7):375–387, 2011.

[124] H. Risken. Fokker-planck equation. In *The Fokker-Planck Equation*, pages 63–95. Springer, 1984.

[125] J.B. Rowe, I. Toni, O. Josephs, R.S.J. Frackowiak, and R.E. Passingham. The prefrontal cortex: response selection or maintenance within working memory? *Science*, 288(5471):1656–1660, 2000.

[126] F. Sagués, J.M. Sancho, and J. García-Ojalvo. Spatiotemporal order out of noise. *Reviews of Modern Physics*, 79(3):829, 2007.

[127] A. Samsonovich and B.L. McNaughton. Path integration and cognitive mapping in a continuous attractor neural network model. *The Journal of Neuroscience*, 17(15):5900–5920, 1997.

[128] B. Sandstede. Stability of travelling waves. *Handbook of Dynamical Systems*, 2:983–1055, 2002.

[129] F. Sargolini, M. Fyhn, T. Hafting, B.L. McNaughton, M.P. Witter, M. Moser, and E.I. Moser. Conjunctive representation of position, direction, and velocity in entorhinal cortex. *Science*, 312(5774):758–762, 2006.

[130] E. Save, L. Nerad, and B. Poucet. Contribution of multiple sensory information to place field stability in hippocampal place cells. *Hippocampus*, 10:64–76, 2000.

[131] D. Schluppeck, C.E. Curtis, P.W. Glimcher, and D.J. Heeger. Sustained activity in topographic areas of human posterior parietal cortex during memory-guided saccades. *The Journal of Neuroscience*, 26(19):5098–5108, 2006.

[132] E. Schneidman, W. Bialek, and M.J. Berry. Synergy, redundancy, and independence in population codes. *The Journal of Neuroscience*, 23(37):11539–11553, 2003.

[133] I. Sendiña-Nadal, S. Alonso, V. Pérez-Muñuzuri, M. Gómez-Gesteira, V. Pérez-Villar, L. Ramírez-Piscina, J. Casademunt, J.M. Sancho, and F. Sagués. Brownian motion of spiral waves driven by spatiotemporal structured noise. *Physical Review Letters*, 84(12):2734, 2000.

[134] H.S. Seung. How the brain keeps the eyes still. *Proceedings of the National Academy of Sciences*, 93(23):13339–13344, 1996.

[135] A. Shpiro, R. Curtu, J. Rinzel, and N. Rubin. Dynamical characteristics common to neuronal competition models. *Journal of Neurophysiology*, 97(1):462–73, 2007.

[136] J.R. Silvester. Determinants of block matrices. *The Mathematical Gazette*, 84(501):460–467, 2000.

[137] J.J.E. Slotine and W. Li. *Applied Nonlinear Control*. Prentice Hall, 1991.

[138] T. Solstad, C.N. Boccara, E. Kropff, M. Moser, and E.I. Moser. Representation of geometric borders in the entorhinal cortex. *Science*, 322(5909):1865–8, 2008.

[139] P. Song and X. Wang. Angular path integration by moving "hill of activity": a spiking neuron model without recurrent excitation of the head-direction system. *The Journal of Neuroscience*, 25(4):1002–14, 2005.

[140] S. Sreenivasan and I. Fiete. Grid cells generate an analog error-correcting code for singularly precise neural computation. *Nature Neuroscience*, 14(10):1330–1337, 2011.

[141] J.S. Taube. The head direction signal: origins and sensory-motor integration. *Annual Review of Neuroscience*, 30:181–207, 2007.

[142] J.G. Taylor. Neural 'bubble' dynamics in two dimensions: foundations. *Biological Cybernetics*, 80(6):393–409, 1999.

[143] R. Thul, S. Coombes, and C.R. Laing. Neural field models with threshold noise. *The Journal of Mathematical Neuroscience*, 6(3):1–26, 2016.

[144] A. Tsao, M. Moser, and E.I. Moser. Traces of experience in the lateral entorhinal cortex. *Current Biology*, 23(5):399–405, Mar 2013.

[145] N. Ulanovsky and C.F. Moss. Dynamics of hippocampal spatial representation in echolocating bats. *Hippocampus*, 21(2):150–61, 2011.

[146] S. Valerio and J.S. Taube. Path integration: how the head direction signal maintains and corrects spatial orientation. *Nature Neuroscience*, 15(10):1445–1453, 2012.

[147] C. van Vreeswijk and H. Sompolinsky. Chaos in neuronal networks with

balanced excitatory and inhibitory activity. *Science*, 274(5293):1724–1726, 1996.

[148] R. Veltz and O. Faugeras. Local/global analysis of the stationary solutions of some neural field equations. *SIAM Journal on Applied Dynamical Systems*, 9(3):954–998, 2010.

[149] X. Wang. Synaptic basis of cortical persistent activity: the importance of nmda receptors to working memory. *The Journal of Neuroscience*, 19(21):9587–9603, 1999.

[150] X. Wang. Synaptic reverberation underlying mnemonic persistent activity. *Trends in Neurosciences*, 24(8):455–463, 2001.

[151] X. Wang. Neurophysiological and computational principles of cortical rhythms in cognition. *Physiological Reviews*, 90(3):1195–268, 2010.

[152] X. Wang and J. Rinzel. Alternating and synchronous rhythms in reciprocally inhibitory model neurons. *Neural Computation*, 4(1):84–97, 1992.

[153] Y. Wang, H. Markram, P.H. Goodman, T.K. Berger, J. Ma, and P.S. Goldman-Rakic. Heterogeneity in the pyramidal network of the medial prefrontal cortex. *Nature Neuroscience*, 9(4):534–542, 2006.

[154] B. Weber, C. Burger, M.T. Wyss, G.K. Von Schulthess, F. Scheffold, and A. Buck. Optical imaging of the spatiotemporal dynamics of cerebral blood flow and oxidative metabolism in the rat barrel cortex. *European Journal of Neuroscience*, 20(10):2664–2670, 2004.

[155] A.W. Welday, I.G. Shlifer, M.L. Bloom, K. Zhang, and Blair H.T. Cosine directional tuning of theta cell burst frequencies: Evidence for spatial coding by oscillatory interference. *The Journal of Neuroscience*, 16:16157–16176, 2011.

[156] H. Werner and T. Richter. Circular stationary solutions in two-dimensional neural fields. *Biological Cybernetics*, 85(3):211–217, 2001.

[157] T.J. Wills, C. Lever, F. Cacucci, N. Burgess, and J. O'Keefe. Attractor dynamics in the hippocampal representation of the local environment. *Science*, 308(5723):873–876, 2005.

[158] H.R. Wilson and J.D. Cowan. Excitatory and inhibitory interactions in localized populations of model neurons. *Biophysical Journal*, 12(1):1–24, 1972.

[159] H.R. Wilson and J.D. Cowan. A mathematical theory of the functional dynamics of cortical and thalamic nervous tissue. *Biological Cybernetics*, 13(2):55–80, 1973.

[160] K. Wimmer, D.Q. Nykamp, C. Constantinidis, and A. Compte. Bump attractor dynamics in prefrontal cortex explains behavioral precision in spatial working memory. *Nature Neuroscience*, 17(3):431–439, 2014.

[161] L. Wu and J.D. Dickman. Neural correlates of a magnetic sense. *Science*, 336(6084):1054–1057, 2012.

[162] S. Wu and S. Amari. Computing with continuous attractors: stability and online aspects. *Neural Computation*, 17(10):2215–2239, 2005.

[163] S. Wu, K. Hamaguchi, and S. Amari. Dynamics and computation of continuous attractors. *Neural Computation*, 20(4):994–1025, 2008.

[164] X. Xie, R. Hahnloser, and H.S. Seung. Double-ring network model of the head-direction system. *Physical Review E*, 66(4):041902, 2002.

[165] M.M. Yartsev and N. Ulanovsky. Representation of three-dimensional space in the hippocampus of flying bats. *Science*, 340(6130):367–372, 2013.

[166] K. Yoon, M.A. Buice, C. Barry, R. Hayman, N. Burgess, and I.R. Fiete. Specific evidence of low-dimensional continuous attractor dynamics in grid cells. *Nature Neuroscience*, 16(8):1077–1084, 2013.

[167] K. Yoon, S. Lewallen, A.A. Kinkhabwala, D.W. Tank, and I.R. Fiete. Grid cell responses in 1d environments assessed as slices through a 2d lattice. *Neuron*, 89(5):1086–1099, 2016.

[168] K. Zhang. Representation of spatial orientation by the intrinsic dynamics of the head-direction cell ensemble: a theory. *The Journal of Neuroscience*, 16(6):2112–2126, 1996.

[169] S. Zhang, F. Schönfeld, L. Wiskott, and D. Manahan-Vaughan. Spatial representations of place cells in darkness are supported by path integration and border information. *Frontiers in Behavioral Neuroscience*, 8(222):1–12, 2014.